Exploitation of the MERIS oxygen *A* band channel for the retrieval of cloud-top pressure and the correction of instrumental stray light

DISSERTATION

zur Erlangung des akademischen Grades eines
Doktors der Naturwissenschaften
am Fachbereich für Geowissenschaften
der Freien Universität Berlin

vorgelegt von

RASMUS LINDSTROT

Berlin, August 2009

1. Gutachter: Prof. Dr. Jürgen Fischer

2. Gutachter: Prof. Dr. Ralf Bennartz

Disputationstermin: 27.10.2009

Selbstständigkeitserklärung

Hiermit erkläre ich an Eides Statt, dass ich die vorliegende Arbeit selbstständig und ohne fremde Hilfe angefertigt, keine anderen als die angegebenen Quellen und Hilfsmittel benutzt und die den benutzten Quellen wörtlich oder inhaltlich entnommenen Stellen als solche kenntlich gemacht habe. Diese Arbeit hat in gleicher oder ähnlicher Form noch keiner Prüfungsbehörde vorgelegen.

Berlin, 21.08.2009

Contents

1 Introduction

Clouds play an extraordinarily important role within the weather and climate system of the earth. Due to the complex interactions with e.g. radiation, air humidity and aerosols, they control the radiation budget and govern the water cycle on earth. In our every day life we experience numerous of such direct or indirect impacts of clouds, be it through the shading of sunlight, the formation of precipitation or the mild- or coldness of winter nights in case of overcast or clear sky.

A strong modulation of the energy budget is one of the central influences of clouds on the state of the earth-ocean-atmosphere-system: Clouds cool the earth by reflecting a significant fraction of the incident solar radiation, adding up to ~30 % in case of optically moderately thick clouds like stratocumulus. In addition, they emit radiation to space according to the temperature of the cloud droplets. This loss of energy is compensated in parts by an absorption of the thermal, terrestrial emission, reducing the radiative cooling of the earth. Although this contribution to the Greenhouse effect is much stronger than that of e.g. atmospheric carbon dioxide, the global net effect of clouds is a cooling of the atmosphere. Based on data of the **E**arth **R**adiation **B**udget **E**xperiment (ERBE, Kyle et al. (1993)), Ramanathan et al. (1989) found a total net flux change due to clouds of -16.6 W/m^2 at the top of the atmosphere. Even higher values were found by Ardanuy et al. (1991) (-26.8 W/m^2) and Rossow and Zhang (1995), who specified the global cloud flux change as -32.4 W/m^2.

However, the actual radiative effect of individual clouds depends on their macro- and microphysical properties like cloud height, optical thickness, the effective droplet radius, etc., and can be both positive or negative. The algebraic sign of the effect is mainly determined by the cloud height (e.g. Mace et al. (2006)): High, cold clouds tend to warm the atmosphere, as they are often optically thin and reflect little solar radiation whereas they almost completely absorb the terrestrial emission. Due to their low temperatures, the emission of energy to space is weak. In contrast, low clouds contribute to the cooling of the atmosphere, as they are usually optically thick and reflect large parts of the incident solar radiation. Due to their low heights and high temperatures the emission of energy to space and therefore the loss of energy inherent to the atmosphere is strong.

Given the strong influence of clouds on the overall earth radiation budget and, more explicitely, the vertical and latitudinal distribution of radiative heating and cooling in the atmosphere, an accurate description of clouds in climate models is of high importance.

However, due to their diversity and complexity, clouds are still a major source of uncertainty in the simulation of climate development (Le Treut et al. (2007); Randall et al. (2007), and citations therein). The feedback of clouds to the changing environment is highly uncertain, the cooling effect of clouds might be enhanced or weakened: The response of the cloud radiative forcing is expected to be between -2 W/m^2 and +1.5 W/m^2 (Meehl et al. (2004); Tsushima et al. (2006)). Precise measurements of cloud properties are therefore crucial in order to feed and validate climate models and understand the shortcomings of state-of-the-art modelling approaches.

Satellite observations provide an indispensable contribution to the monitoring of atmosphere, earth and ocean. Since it is impossible to operationally perform in-situ measurements of cloud properties, the spaceborne remote sensing of clouds is of special importance. The methodologies for the retrieval of cloud properties from satellite data have been constantly advanced during the past decades. In case of the retrieval of cloud altitude, representing one of the most decisive parameters for the cloud radiative effect, several techniques have been developed. The most popular methodologies make use of either the thermal emission of the clouds, allowing for the determination of the cloud's temperature and height (e.g. Menzel et al. (1982, 2006)) or stereoscopic views, exploiting the height-dependent parallax of clouds when looked at from different angles (e.g. Seiz et al. (2006)). Another possibility for the detection of cloud height is the exploitation of measurements within the oxygen *A* absorption band at 0.76 µm (Yamamoto and Wark (1961); Wu (1985); Fischer and Grassl (1991)): The mass of oxygen along the path of reflected sunlight is derived from measurements inside the absorption band. Since oxygen is well mixed in the atmosphere, the traversed mass of air can directly be determined, allowing for the retrieval of surface pressure in clear sky cases and cloud-top pressure in case of measurements above clouds. Since the launch of ENVISAT (**Envi**ronmental **Sat**ellite) on March 1st, 2002, measurements inside the O_2 *A* band are available from MERIS (**Me**dium **R**esolution **I**maging **S**pectrometer, see section 2.2 or Morel et al. (1993)). MERIS, primarily designed for the remote sensing of coastal waters, is operationally used for the retrieval of cloud properties like optical thickness and height.

In the frame of this work, the O_2 *A* band technique is used for the retrieval of cloud-top pressure from MERIS measurements. In chapter 2, extensive simulation studies regarding the sensitivity of MERIS-like measurements to cloud-top pressure and other influ-

encing parameters are presented. An analysis of the information content and the degrees of freedom of O_2 *A* band measurements above clouds are included. The MERIS cloud-top pressure retrieval algorithm, as implemented in the MERIS ground segment (Fischer et al. (1997)), was validated using airborne LIDAR measurements of cloud-top height. The results of the validation campaign are shown and discussed in chapter 3. One of the shortcomings of currently used cloud retrieval algorithms is the assumption of single-layered clouds. However, since in several studies low level clouds were found in ~50 % of cases where cirrus clouds were present (Fye (1978); Hahn et al. (1984); Mace et al. (1997)), this assumption is not fulfilled in general and results in either a biased retrieval or the missing of one of the cloud layers. An attempt to identify two-layered cloud systems and derive the height of both layers is shown in chapter 4. The retrieval algorithm is based on synergistic measurements of MERIS and AATSR (**A**dvanced **A**long **T**rack **S**canning **R**adiometer, Huot et al. (2001)), both mounted on ENVISAT. Using an optimal estimation technique, the heights of optically thin cirrus above optically thick water clouds are derived.

One of the main sources of errors of MERIS measurements inside the oxygen *A* band is instrumental stray light, caused by multiple scattering at optical elements inside the instrument like lenses or gratings. The technique for the correction of stray light implemented within the MERIS ground segment fails to completely remove the stray light contribution from the measured signal, causing significant artefacts in the derived products. In the frame of this work, an empirical correction of stray light was developed, based on the optimization of a brightness-dependent stray light model by adjusting the retrieved surface and cloud-top pressure to reference data. As a mandatory prerequisite, an algorithm for the retrieval of surface pressure from MERIS measurements had to be developed, presented in chapter 5. The stray light correction strategy and results are shown and discussed in chapter 6. In chapter 7 a summary and an outlook on future work are given.

2 Remote sensing of cloud-top pressure using moderately resolved measurements within the oxygen *A* band - a sensitivity study

---

Preusker, R., and R. Lindstrot, (2009), J. Appl. Meteor. Climatol., 48, 1562–1574.

Abstract

Reflected solar radiation measured by MERIS (**Me**dium **R**esolution **I**maging **S**pectrometer) on ENVISAT (**Envi**ronmental **Sat**ellite) is currently used within ESA's ground segment for the retrieval of cloud-top pressure. The algorithm is based on the analysis of the gaseous absorption of solar radiation in the oxygen *A* band around 762 nm. The strength of absorption is directly related to the average photon path length, which is mainly determined by the cloud-top pressure. However, it additionally depends on surface and cloud properties, like cloud thickness and microphysics. The interpretation of the measurements is further complicated by the temperature-dependence of the absorption line shapes and the sensitivity to the spectral properties of the spectrometer like spectral position and width.

This paper is focused on results of sensitivity studies using the radiative transfer model MOMO, regarding the most important parameters affecting the measurements of MERIS or similar instruments. The cloud-top pressure retrieval scheme is briefly presented. An analysis of the information content and the degrees of freedom of measurements within the oxygen *A* band is included in this study.

2.1 Introduction

The monitoring of atmospheric parameters relevant for weather and climate has been improved considerably in the last decades by the increasing use of satellite observations. Due to their global coverage and high spatial resolutions, satellite measurements serve as input and validation data sets for weather and climate models and provide a basis for a better understanding of the physical processes and interactions in the atmosphere. However, the development of reliable and accurate algorithms for the retrieval of atmospheric parameters from satellite observations is challenging. In addition to the limiting influence of instrumental constraints, it is difficult to quantify the influence of the parameter of interest, since remote sensing measurements are usually sensitive to a variety of parameters. The ambiguity of the interpretation of the observed signals cause large retrieval uncertainties, especially in case of cloud properties like cloud-top pressure, representing one of the most desired parameters to be monitored from space. The most common techniques for the retrieval of cloud-top pressure are based on measuring the thermal emission of clouds in atmospheric window channels or, more advanced, in the carbon dioxide absorption band around 14 µm (CO_2-Slicing, Menzel et al. (1982, 2006)). These methods perform well in the upper atmosphere but show large deviations for low clouds, since here the sensitivity is reduced. Beside radar and lidar techniques, yielding the highest accuracies but no spatial coverage, and stereoscopic methods, the most promising approach in the visible and near infrared spectral region is an exploitation of the oxygen absorption band around 762 nm. This technique is based on the assumption, that the mean photon path length of the reflected solar radiation is related to the amount of absorption measured in the O_2 *A* band. In a cloudy atmosphere the mean photon path length is primarily determined by the air mass above the cloud, the cloud-top pressure (herein after referred to as CTP). Hence CTP can be estimated from the transmission within the O_2 *A* band, approximated by the ratio of the measured radiance in an absorption channel and a window channel. Theoretical investigations as well as aircraft measurements have shown the potential usefulness of the O_2 *A* band (Wu (1985); Fischer and Grassl (1991); Fischer et al. (1991); Kuze and Chance (1994); O'Brien and Mitchell (1992)). The method was first proposed by Yamamoto and Wark (1961) and operationally applied to measurements of GOME (**G**lobal **O**zone **M**easuring **E**xperiment, Burrows et al. (1999)) and POLDER (**Pol**arisation and **D**irectionality of

the **E**arth´s **R**eflectance Buriez et al. (1997)). The POLDER algorithm did not consider multiple scattering inside the cloud and in consequence had a bias of 170 hPa and bias corrected standard deviation of 70 hPa as compared to cloud-top temperatures retrieved from Meteosat measurements (Vanbauce et al. (1998)).

Since the launch of ENVISAT in 2002, the oxygen *A* band method is used for the retrieval of CTP from observations of the **Me**dium **R**esolution **I**maging **S**pectrometer (MERIS). MERIS, primarily designed for ocean color remote sensing, provides measurements in 15 channels between 0.4 µm and 1.0 µm (see table 2.1), one of them located in the O_2 *A* band (channel 11). Measurements within this absorption band allow the determination of the mean effective photon path length of reflected solar light at 0.76 µm in the atmosphere. Additional information from the shortwave infrared and thermal spectral regions about the cloud liquid and ice water absorption is not available from MERIS, which hampers the estimation of that part of the photon path that lies within the cloud. A rough estimate of this magnitude can be made using the window channel reflectance of MERIS channel 10 at 753 nm as a proxy for the cloud optical thickness. Apart from this complication the relation between the path length and the cloud-top pressure primarily depends on the solar and viewing geometry, which is an easily solveable task.

In summary, MERIS measurements provide two pieces of information about the cloud: the transmission of the reflected solar radiation in the O_2 *A* band, providing the effective photon path length, and the single directional reflectance in the visible channels, allowing an estimate for the pixel mean cloud optical thickness, provided that the reflectivity of the surface is known. The goal is to derive the cloud-top pressure from these two measurements. The diversity of cloud appearances, e.g. their variable geometrical thickness and cloud droplet phase and size complicate the CTP estimation. In particular broken and multi-layered cloud fields lead to ambiguous results, as the mean photon path length is modified significantly in these cases as compared to the single-layered, closed cloud assumed in the retrieval algorithm. This will be discussed in detail in the following sections.

Since all investigations shown here are geared to the spectral properties of MERIS, the instrument is briefly described in section 2.2. However, the results of the later sections are valid for any similar spectrometer performing moderately resolved measurements in the oxygen *A* band. The algorithm for the retrieval of CTP is described in more detail

in section 2.3. The main part of this work, the sensitivity analysis of the O_2 *A* measurements, is presented in section 2.4. It contains a solid description of the simulations and methodologies used and presents and discusses the sensitivities of the O_2 *A* transmittance to CTP, cloud optical thickness, cloud geometrical thickness, cloud fraction, surface albedo, surface pressure, cloud microphysics, channel width and position and the atmospheric temperature profile. Section 2.5 gives in an insight into the information content of measurements in the O_2 *A* band and thereby tries to answer the question whether the use of additional channels or a modification of channel position or width have the potential to improve the retrieval of CTP.

2.2 MERIS

MERIS is a programmable, medium-spectral resolution, imaging spectrometer (Rast et al. (1999)). It is one of ten core instruments on the polar orbiter ENVISAT (**Envi**ronmental **Sat**ellite, launched on March 1st, 2002) flying at 800 km in a sun-synchronous orbit with an equator crossing time of 10:30AM, descending node, and 98.5° inclination. MERIS consists of 5 identical pushbroom imaging spectrometers operating in the solar spectral range (390 to 1040 nm), arranged in a fan shape configuration which covers a total field of view of 68.5° and spans a swath width of around 1150 km. The spectral dispersion is achieved by mapping the entrance slit of a grating spectrometer onto a CCD array. The integration time, instrument optics and CCD array resolution are adjusted such that MERIS has a spatial resolution of 260 m * 300 m and a spectral sampling of 1.25 nm. The instrument electronic data rate provides 15 channels which are programmable by ground command in width and in position. In the regular operation mode the spatial resolution is reduced by a factor of 4 along and across track (reduced resolution mode). In the full resolution mode, the full spatial resolution is transmitted. The central wavelengths of the spectral channels as listed in table 2.1 vary slightly across the field of view of MERIS. This “spectral smile” is caused by curvature of the image of the slit formed in the focal plane array, resulting in viewing angle-dependent central wavelengths of the spectral MERIS channels. In order to accurately determine the spectral smile of MERIS, spectral calibration campaigns are conducted repeatedly, using the full possible spectral resolution in the oxygen *A* band and solar Fraunhofer lines (Delwart et al. (2007)).

Table 2.1: Central wavelength and bandwidth (fwhm) of MERIS spectral channels

Band	Center (nm)	Width (nm)	Usage
1	412.5	10	Yellow substance, turbidity
2	442.5	10	Chlorophyll
3	490	10	Chlorophyll, pigment
4	510	10	Suspended matter, turbidity
5	560	10	Chlorophyll, suspended matter
6	620	10	Suspended matter
7	665	10	Chlorophyll
8	681.25	7.5	Chlorophyll
9	708.25	10	Atmospheric correction, 'red edge'
10	753.75	7.5	Cloud optical thickness, cloud-top pressure reference
11	761.875	3.75	Cloud-top pressure
12	778	10	Aerosol, vegetation
13	865	20	Aerosol, atmospheric correction
14	885	10	Water vapour reference
15	900	10	Water vapour

2.3 Algorithm description

The algorithm for the remote sensing of CTP described herein makes use of the absorption of solar radiation by oxygen at 0.76 µm by relating the strength of absorption to the transmitted airmass: the transmission decreases as the transmitted absorber mass increases. A wide field of remote sensing applications uses this differential absorption technique for the estimation of masses, e.g. the estimation of atmospheric water vapour or trace gases. The presence of clouds significantly alters the path lengths of reflected and back-scattered photons, with high clouds leading to shorter path lengths and high transmission, and low clouds leading to longer path lengths and low transmission. The transmission can not be measured directly, it is estimated by the ratio r of the measured radiance in the absorption channel and one absorption free window channel, namely MERIS channels 11 at 761.875 nm and 10 at 753.75 nm (see figure 2.1):

$$r = L_{11}/L_{10} \tag{2.1}$$

The enhancement of photon path lengths due to in-cloud multiple scattering is a function of cloud optical thickness. Therefore, the window radiance L_{10} serves as an additional

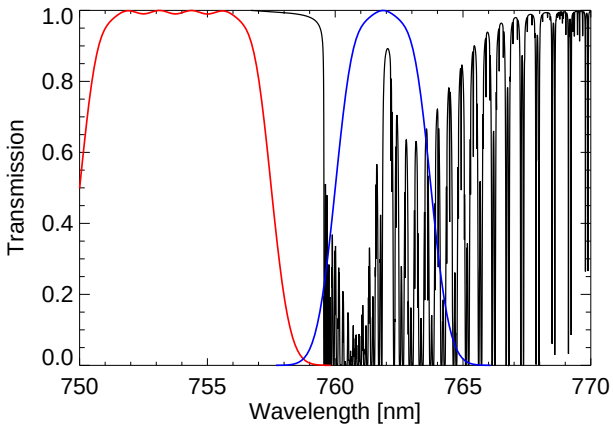

Figure 2.1: Response functions of MERIS channels 10 (red) and 11 (blue) and transmission of molecular oxygen at 760 nm.

input parameter to the algorithm, as it allows an estimation of the cloud optical thickness. Although the vertical profile of extinction and the cloud geometrical thickness are not known, the inclusion of the window channel radiance therefore allows for the correction of multiple scattering effects within the cloud layer.

The retrieval algorithm is based on radiative transfer simulations using the **M**atrix **O**perator **Mo**del (MOMO, Fischer and Grassl (1984); Fell and Fischer (2001)). The simulations were used to derive coefficients of a multi-dimensional non-linear regression that relates the measured radiance to CTP. The regression approach was chosen in order to obtain an algorithm which is able to work in near real time within ESA's ground segment, without needing a high amount of calculation power and main memory (Fischer et al. (1997)).

2.4 Sensitivity study

In order to determine the sensitivity of MERIS measurements to the individual influencing quantities, radiative transfer calculations were performed. The simulations were analyzed with respect to the influence of CTP and other geophysical parameters like cloud optical and geometrical thickness, surface albedo and temperature profile etc. Additionally, the influences of instrumental parameters like spectral channel position

and width were determined.

2.4.1 Radiative transfer simulations

The radiative transfer code MOMO was used to simulate the radiance in the MERIS channels. A modified k-distribution technique was applied to incorporate gaseous absorption (Goody and Young (1989); Bennartz and Fischer (2000)). The calculations were based on the HITRAN 2004 dataset (Rothman et al. (2005)), providing shape and strength parameters for the single absorption lines of the main atmospheric gases. In order to take into account the temperature dependence of the absorption lines, six standard temperature profiles, as provided by McClatchey et al. (1972), were used for the simulations. The clouds were assumed to be vertically homogeneous. The scattering at cloud particles was represented by appropriate scattering and extinction coefficients and the corresponding scattering phase function. These parameters were obtained by Mie theory (Wiscombe (1980)).

2.4.2 Results

2.4.2.1 Single cloud layer

It is common to describe the sensitivity of a measurement by the following partial differential:

$$\xi_j^i = \frac{\delta \ln s_i}{\delta \ln P_j}$$

which quantifies the relative change of a signal s_i due to the relative change of the parameter P_j. Here the signal carrying information is the transmitance of the reflected solar radiation, quantified by the ratio r (eq. 2.1). The sensitivity becomes:

$$\xi_j = \frac{\delta \ln r}{\delta \ln P_j} \, .$$

However, this description has the disadvantage that it depends on the absolute scales of the parameter P_j, hampering a quantitative comparison of the different sensitivities. Thus we decide to relate the relative change of the signal to a reasonable change of each

physical parameter. Thus ξ is calculated as

$$\xi_j = \frac{\delta \ln r}{\delta \ln P_j} \cdot \Delta P_j$$

if ΔP_j is a relative change or

$$\xi_j = \frac{\delta \ln r}{\delta P_j} \cdot \Delta P_j$$

if ΔP_j is an absolute value. We derived the sensitivities for six parameters: cloud optical thickness τ, surface albedo α, cloud fraction cf, cloud geometrical thickness ct (in hPa), surface pressure sp and cloud-top pressure ctp as the final quantity of interest. Additionally, we calculated the sensitivity to changes of the spectral channel response (in fact to the uncertainty of the spectral characterisation of MERIS) quantified by the center wavelength cw and by the effective bandwidth bw. The sensitivities to α,τ, and cf are given with respect to a 10 % change, the sensitivities to ctp, sp and ct are calculated with respect to a change of 10 hPa and the sensitivities to the channel characterisation are given with respect to changes of 0.1 Å. These values were chosen because they all cause a change of signal in the same order of magnitude.
Another important parameter, the sensitivity to the viewing geometry, has not been considered in order to limit the complexity of the presented results. It is usually known with high precision. In case of cloud fraction, a very simple approach has been chosen. The used radiative transfer code MOMO does not consider three-dimensional effects. Using the "independent pixel approximation", a cloud fraction was simply modelled by mixing the results of cloudy and clear case simulations, neglecting the effects of horizontal transport of photons. A more realistic calculation including three-dimensional effects is beyond the scope of this study.
All sensitivities are calculated with respect to an increasing quantity of the corresponding parameter. Thus the sensitivity to CTP has a negative sign since the transmittance decreases if CTP increases (if the cloud is shifted to a lower level). The sensitivities are calculated straight forwardly by simulating radiation fields with small changes of the corresponding physical parameter. Four general cases will be discussed here:

- *a)* a thin cloud above a dark surface,
- *b)* a thick cloud above a dark surface,

- *c)* a thin cloud above a bright surface,
- *d)* a thick cloud above a bright surface.

The simulated cloud is vertically homogeneous with an optical thickness of 20 ("thick") or 2 ("thin"). The cloud particle sizes follow a modified Gamma-Hansen distribution (Hansen (1971)) with an optical effective radius of 12. The surface was modelled as a Lambertian reflector with an albedo of 0.1 ("dark") or 0.6 ("bright"). At 760 nm, the surface albedo is usually darker (ocean surface) or brighter (land surface) than 0.1. Nevertheless, this value was chosen to represent both the dark land and ocean cases as no fundamental qualitative differences of the results are to be expected for slightly higher or lower values of surface albedo. The results were calculated for nadir view and a solar incident angle of 41.4°. All sensitivities are shown as a function of the center wavelength *cw* of the absorbing channel. This has two advantages: 1.) It covers the full spectral variability of MERIS channel 11. 2.) It shows the variability with respect to the absorption optical thickness (at least in the range a MERIS-like instrument can cover) and is therewith transferable to instruments with similar characteristics.
The results are summarized in figure 2.2 a)- d). Specific conclusions are as follows:

1. In all cases the sensitivity to changes in the channel position ($\delta \ln r/\delta cw \cdot 0.1$ Å: blue stars) and bandwidth ($\delta \ln r/\delta bw \cdot 0.1$ Å: brown triangles) can be significant. The sensitivity varies between $+0.5$ % and -0.3 % for changes of 0.1 Å. It is important to note that both sensitivities are zero for all cases around 762 nm, which is the position of minimum absorption between the P- and the R-branch of the band. The nominal central wavelength of MERIS band 11 was chosen to be 761.875 nm for this reason.

2. In cases *a)*, *b)* and *d)*, the cases with either a thick cloud or a dark surface, most of the detected radiance stems from reflection at the cloud. The sensitivity to changes of CTP ($\delta \ln r/\delta ctp \cdot 10$ hPa: red triangles) varies between 0.4 % and 1.2 % for height changes of 10 hPa. Interestingly, the maximum of the cloud-top sensitivity is approximately at the same position as the minimum of the channel characteristic sensitivities. It is very important to note here that the cloud geometrical thickness has only an approximately 25 % lower sensitivity ($\delta \ln r/\delta ct \cdot 10$ hPa: green plus signs) than the cloud-top pressure, regardless of the case under consideration. In

other words: a cloud height change of 10 hPa causes the same change of signal as a change of the geometrical thickness of 13 hPa of the simulated homogeneous cloud. Similar findings have already been stated by other authors (Fischer and Grassl (1991); O'Brien and Mitchell (1992); Stephens and Heidinger (2000)). With respect to the central wavelength of the channel, the sensitivities are correlated. That is to say the spectral dependence of the sensitivies is similar but not equal. Hence the two parameters can be separeted to a limited degree using two or more channels in the O_2 *A* band at a MERIS-like spectral resolution (see section 2.5.2). It has been shown that multiple channels within the oxygen *A* band with a considerably higher spectral resolution (0.1 nm) allow the simultaneous retrieval of both quantities (O'Brien and Mitchell (1992); Stephens and Heidinger (2000)).

3. In all cases the sensitivity to changes in the cloud optical thickness ($\delta \ln r / \delta \ln \tau \cdot 0.1$: pink squares) almost equals the sensitivity to changes in the cloud fraction ($\delta \ln r / \delta \ln cf \cdot 0.1$: orange crosses). A 10 % change of cloud fraction has a similar effect as a 10 % change of cloud optical thickness. Hence a sub-pixel cloud fraction can not be inferred from MERIS measurements.

4. Above bright surfaces (cases *c)* and *d)*) a 10 % change of cloud optical thickness or cloud fraction causes a change in signal comparable to a cloud-top pressure change of 10 hPa. For darker surfaces, the precise knowlegde of the cloud optical thickness / cloud fraction is only needed for optically very thin clouds (case *a)*).

5. The surface brightness sensitivity ($\delta \ln r / \delta \ln \alpha \cdot 0.1$: black diamonds) is significant in case of optically thin clouds (cases *a)* and c*)*). Even in cases of moderately thick clouds above bright surfaces (case d) the measured transmittance *r* is influenced substantially by a change of surface brightness.

6. In case of thin clouds (cases *a)* and *c)*) the signal is influenced significantly by the surface pressure ($\delta \ln r / \delta sf \cdot 10$ hPa: dotted line). Above bright surfaces it is the most important quantity. *r* is not sensitive to surface pressure in case of optically thick clouds.

7. In the case of thin clouds above bright surfaces (case c) the signal is dominated by the surface brightness and the surface pressure, precluding cloud retrievals.

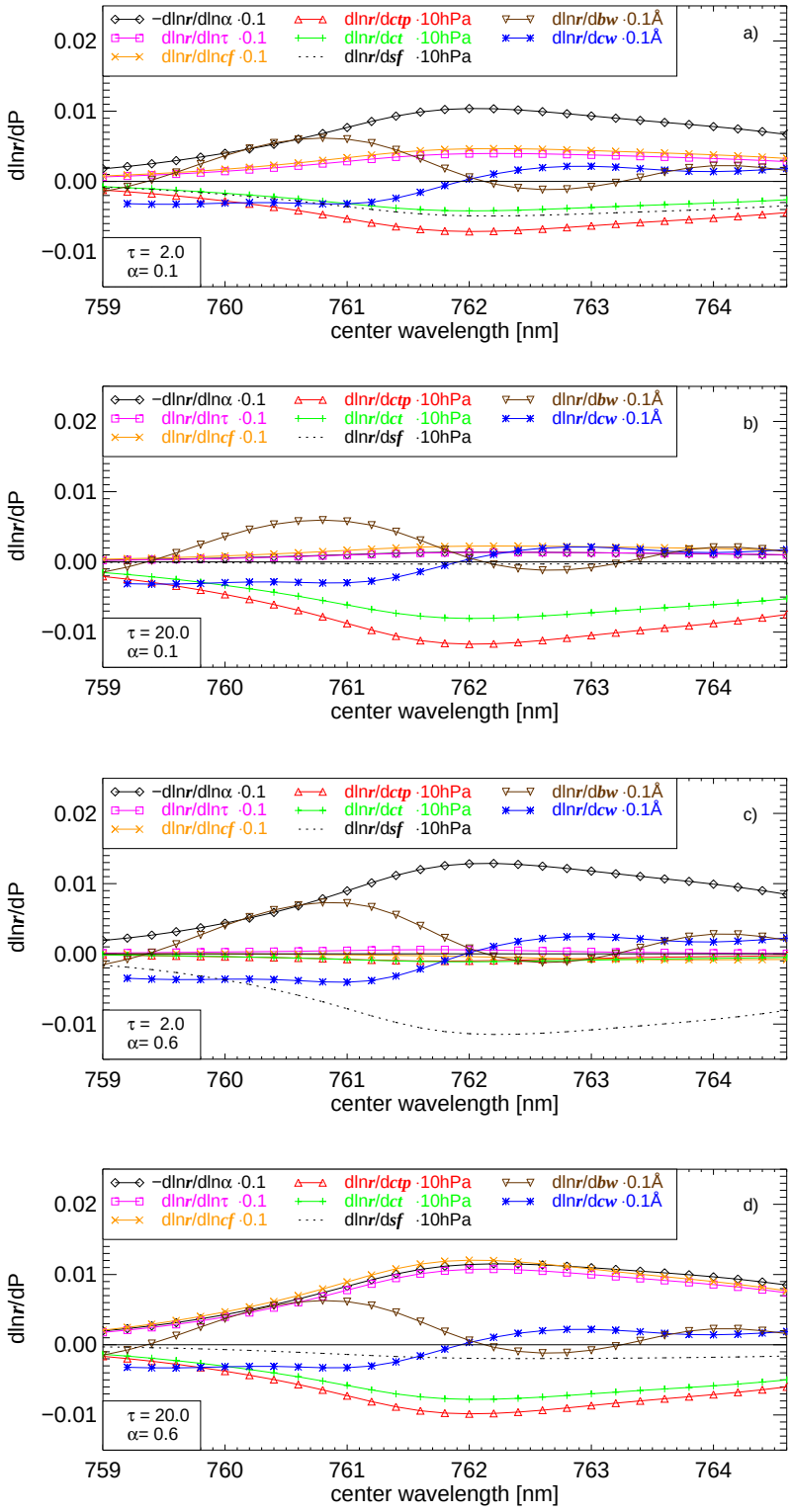

Figure 2.2: Sensitivity of channel ratio r to changes of several parameters, depending on central wavelength of MERIS channel 11 for four different cases. See text for details.

2.4.2.2 Multiple cloud layers

It has been shown above that r is sensitive to the geometrical cloud thickness, or, generally speaking, to the vertical profile of cloud extinction and that the information about the geometrical cloud thickness can not be separated from the information about CTP. The non-realistic assumption of homogeneous single layer clouds is therefore a source of error in the retrieval of CTP. However, the diversity of profiles occurring in real clouds complicates the assessment of the sensitivity to the profile of extinction. In order to completely answer this question, an in-depth study is necessary that is beyond the scope of this work. However, multilayer clouds, frequently appearing in the atmosphere, represent an extreme case of vertically inhomogeneous profiles of extinction. In order to quantify the consequence of multiple cloud layers on the retrieval of CTP, a simple simulation study was carried out: two individual cloud layers were assumed at a height of 750 hPa and 230 hPa, respectively. The total optical thickness of both cloud layers was held constant at a value of 50, whereas the distribution of optical thickness among the two layers was varied. Furthermore, a homogeneous single layer cloud with an optical thickness of 50 was simulated at different altitudes between 750 hPa and 230 hPa. Each distribution of optical thickness in the multilayer case was assigned to a corresponding height of the single layer case by comparing both data sets. The height of the best fitting single layer cloud is what we here call the *effective* cloud-top pressure. Figure 2.3 shows the effective cloud-top pressure as a function of the optical thickness of the upper layer. The investigation has been made for an albedo of 0.1 and of 0.6. Since both curves are identical, the following conclusions do not depend on the surface brightness below the clouds.

1. A moderately thin cloud above the lower cloud only slightly changes the effective cloud height. For instance, an upper cloud optical thickness of 2 increases the effective cloud height by 25 hPa to 725 hPa. This is the same effect as already observed in case *c)* for a thin single layer cloud above a bright surface.

2. A low level cloud changes the effective cloud height significantly, even in case the upper layer is thick. For instance, a lower cloud optical thickness of 10 beneath an upper cloud optical thickness of 40 leads to an increase of the effective CTP by 40 hPa to 270 hPa. The effect is even more pronounced for two equally thick

clouds with an optical thickness of 25. The resulting effective cloud height is at 360 hPa, 130 hPa below the true cloud height of the upper cloud.

A bright surface or a subjacent cloud layer always have a significant impact on the reflected transmission as observed by MERIS, even if the upper cloud layer is optically thick. Only a fraction of the photons incident on a cloud is reflected back to space immediately, while those photons that are transmitted through the cloud might be reflected at lower levels, if the surface beneath is bright enough. Consequently, the average accuracy of the retrieved CTP is worse for high clouds, since the probability of multilayer systems is obviously higher than in case of low clouds. The deduction of supplementary information on the vertical profile of extinction from additional MERIS-like channels in the oxygen *A* band is possible to some degree. The additional information is limited, however, since at this spectral resolution the channels are highly correlated, as evidenced in figure 2.2 and will be further discussed in section 2.5.2.

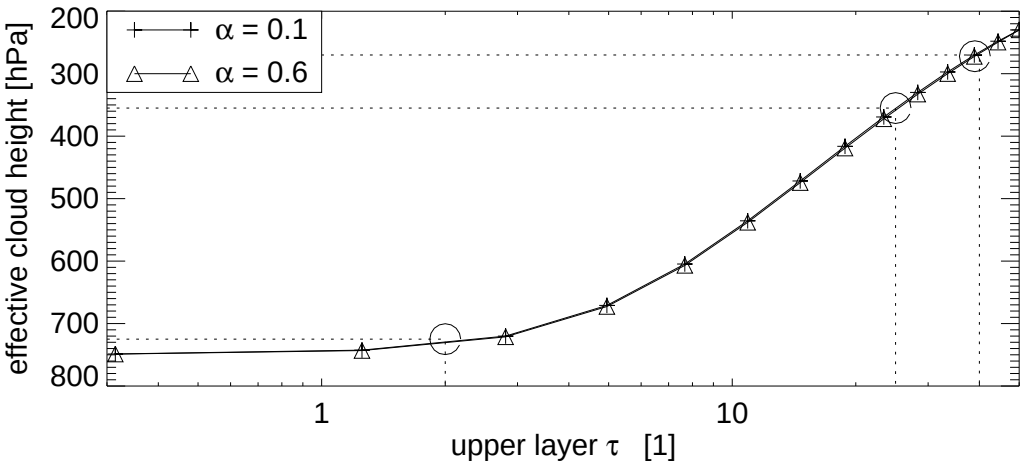

Figure 2.3: Effective single layer cloud-top pressure, depending on distribution of optical thickness for two-layered cloud with a combined optical thickness of $\tau = 50$.

2.4.2.3 Sensitivity to the temperature profile

Due to temperature-dependent broadening of the individual oxygen absorption lines, the transmission in the oxygen *A* band depends on the temperature profile in the observed column. The dominant effect is the so-called pressure broadening in the lower atmosphere that affects the width of the individual absorption lines, with the line width inversely depending on the temperature. In order to determine the sensitivity of the measurements to the temperature profile, we have adopted six standard atmospheric profiles, intended to model the typical climatic conditions in tropical, midlatitude summer, midlatitude winter, subarctic summer, subarctic winter and US standard atmospheres. These model atmospheres (McClatchey et al. (1972)) have been widely used in the atmospheric research community and provide standard vertical profiles of pressure, temperature, water vapor and ozone density. The effects of the different temperature profiles on the measured channel ratio *r*, relative to a US Standard atmosphere, have been analyzed for clouds at different heights. The results are summarized in figure 2.4. First of all it has to be noted that a shift towards lower temperatures causes a decrease of *r*, due to stronger absorption in the line wings. Provided that the real temperature is colder at all height levels, the effect is more pronounced in case of low clouds due to the increase of traversed mass of air (see blue curve, showing the subarctic winter profile). In cases where the differences of temperature changes its sign at some altitude level, the effect is weakened and can even cancel completely (green curve, showing the tropical profile). Disregarding the subarctic winter profile because of the lack of sunlight, the maximum difference found is on the order of 20 hPa for low clouds and much lower for high clouds. In summary, an underestimation of the temperature profile causes an underestimation of CTP and vice versa. However, the errors are small as compared to other error sources.

2.4.2.4 Sensitivity to cloud microphysics

The scattering properties of cloud particles at 0.76 µm depend on the droplet phase, size and shape. In order to determine the sensitivity of the measured channel ratio *r* to cloud microphysics, the radiance field above clouds was simulated for six different scattering phase functions, namely for liquid cloud droplets ($r_{eff} = [7, 15, 20]$ µm) and ice crystals ($r_{eff} = [35, 78, 218]$ µm) of various sizes. The different phase functions, calculated

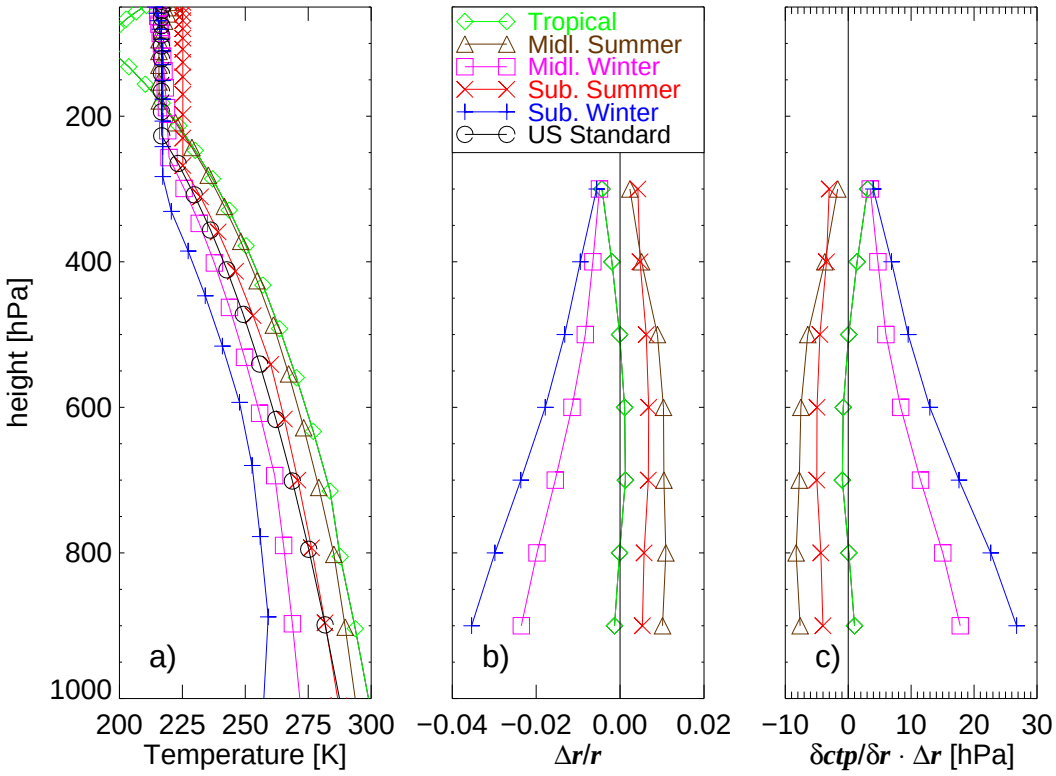

Figure 2.4: Temperature profiles (McClatchey et al. (1972), left panel), relative change of r depending on cloud height and temperature profile as compared to US Standard profile (middle panel), equivalent change in hPa (right panel).

from Mie theroy (liquid cases) and provided by Macke et al. (1996) (ice cases), are displayed in figure 2.5, left panel. All phase functions show the characteristic forward scatter peak but reveal some differences as well. E.g., the liquid phase functions have a distinct minimum in the sideward scatter regions, whereas the ice phase functions show a weak dependence on the scattering angle here.

The right panel shows the effect of a change of cloud microphysics on the O_2 A transmission in the principal plane, for a solar zenith angle of 30°. The sensitivity was calculated for homogeneous clouds at a height of 500 hPa ($\tau = 20$), relative to a cloud with $r_{eff} = 15\,\mu m$, and is expressed as the equivalent change of cloud height. A sole change of droplet size does not change r significantly, whereas a switch of cloud phase (and shape) modifies r, corresponding to a change of cloud height of up to 10 hPa for cer-

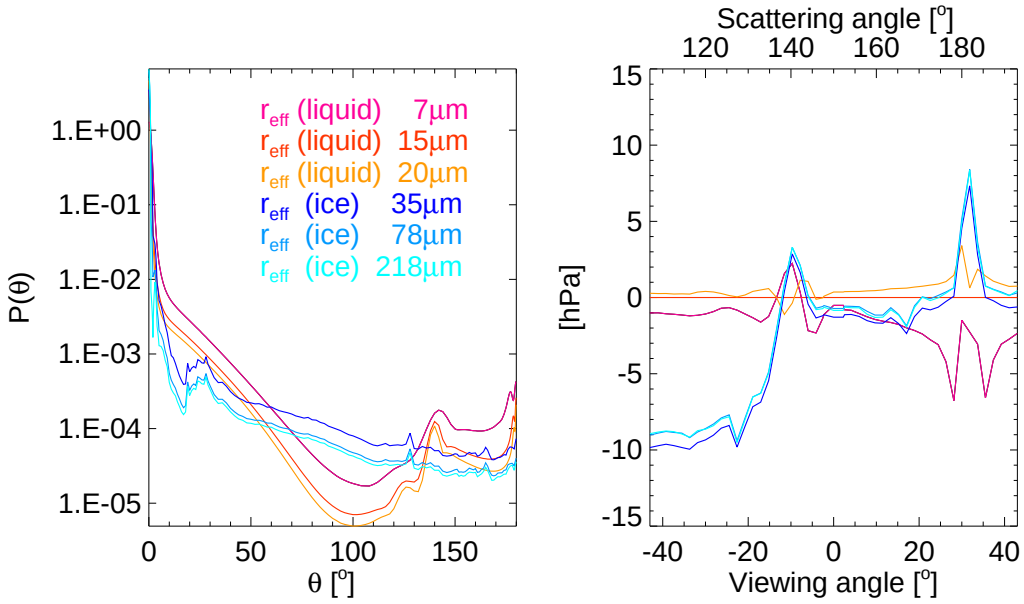

Figure 2.5: Normalized scattering phase functions of six different cloud droplets (left panel), equivalent change of CTP, relative to liquid cloud with r_{eff}=15 µm, in principle plane for solar zenith angle of 30° (right panel).

tain viewing geometries. The negative bias of the ice cases between $-40°$ and $-20°$ of viewing zenith corresponds to the differences of the scattering phase functions between a scattering angle around $\theta = 120°$ (see upper x-axis annotation of right panel), whereas the deviations around 30° of viewing zenith are caused by the differences around the backscatter peak ($\theta = 180°$). The maximum errors found are in the range of 10 hPa and are therefore small as compared to other error sources.

2.4.3 Conclusions

The biggest source of error for the retrieval of CTP is the presence of multilayer clouds. In these cases, the retrieved CTP represents an effective single-layer height, depending on the distribution of optical thickness among the cloud layers. Further important sources of error are the unknown cloud geometrical thickness and cloud fraction, whereas the cloud optical thickness can be estimated using a window reflectance close to the O_2 *A* band. The cloud microphysics and the temperature profile account for maximum errors of less than 10 hPa and 20 hPa, respectively, and are therefore of minor

importance. In case of optically thin clouds and bright surfaces, the surface reflectance and the surface pressure have to be known with high precision. Summarizing, the retrieval of CTP from measurements in the O_2 *A* band is possible with high accuracy in case of optically thick, single-layered clouds. These conditions are usually met by low clouds, whereas the probability of multilayer cloud structures increases with cloud height.
Regardless of the atmospheric condition and the individual cloud properties, the spectral characterization of the instrument is of great importance, as a change of central wavelength or spectral channel width significantly alters the gaseous optical depth observed by the channel. Depending on the channel position, an uncertainty of merely 0.1 Å of one of these properties causes an uncertainty of up to 10 hPa in CTP.

2.5 Analysis of the information content and the degrees of freedom of measurements within the oxygen *A* band

2.5.1 Theoretical basis

The information content and the degrees of freedom of a specific retrieval can be determined on the basis of the inverse theory, using an appropriate forward model and realistic assumptions about error correlations. The obtained parameters can be used to investigate the feasibility of the retrieval and optimize its performance by finding the optimal channel configuration, for instance. In the frame of this work, only a brief overview about this theory is given. An in-depth description can be found in Rodgers (2000).
In retrieval theory concepts the state vector x usually denotes the atmospheric parameters to be retrieved. Assuming a linear behaviour within the error bounds of the retrieved state, the state vector can be related to the measurement vector y, containing all available, individual measurements, via the weighting function $\mathbf{K}$ and a random error vector ε. This can be written as

$$y - y_0 = \mathbf{K}(x - x_0) + \varepsilon$$

for an arbitrary linearisation point, defined by x_0 and y_0. Since $\mathbf{K}$ can usually be assumed to behave linearly only in a small range around the actual state, the true state x can not be determined directly. Instead, iterative methods like optimal estimation have to be applied.
Prior to any measurement, a background knowledge about x is given by the average values, variances and correlations of the retrieval parameters. Analogously, assumptions about measurement errors like radiometric noise can be made. By compiling the measurement and background error covariances in the measurement error covariance matrix $\mathbf{S}_\varepsilon$ and the background error covariance matrix $\mathbf{S_a}$, the so-called averaging kernel matrix $\mathbf{A}$ can be calculated by

$$\mathbf{A} = (\mathbf{K^T S_\varepsilon^{-1} K} + \mathbf{S_a^{-1}})^{-1} \mathbf{K^T S_\varepsilon^{-1} K}$$

This allows the determination of the degrees of freedom d of the measurement, representing the number of independent parameters that can be retrieved.

$$d = tr(\mathbf{A})$$

The maximum possible value of d is the number of elements of the state vector x or, if smaller, the number of elements of the measurement vector y. A second quantity that is useful for the evaluation of the measurement quality is the information content Ψ of a measurement:

$$\Psi = -\frac{1}{2} \log_2 |\mathbf{I} - \mathbf{A}|)$$

By using the binary logarithm, the resulting number Ψ can be interpreted as the number of bits, giving the number of states that can be separated. In case of a one elemental state vector, this can be used directly to determine the resolving power of the measurements regarding the retrieval parameter.

2.5.2 Application to observations in the oxygen *A* band

In order to determine the amount of information inherent to measurements within the oxygen *A* band, a simulation study was performed, using again the radiative transfer code MOMO (see section 2.4.1). Based on the four test cases *a) - d)* as defined in section

2.4.2.1, Ψ and d were computed depending on channel position, number of channels and channel width. The state vector x was composed of cloud optical thickness, CTP and cloud volume extinction, assuming again homogeneous, single layer clouds in order to reduce the complexity of the study. All other influencing parameters like surface albedo, temperature profile, aerosol optical thickness and central wavelength of the channels were assumed to be known. The background error covariance matrix $\mathbf{S_a}$ was defined by the climatological variance of the retrieval parameters. The measurement errors were assumed to be uncorrelated with a signal-to-noise ratio of 250. The accuracy of the resulting values of d and Ψ is slightly reduced by these simplifying assumptions, as, e.g., the measurement errors might be correlated due to uniform wavelength shifts of all channels. However, the chosen approach is well suitable for the purpose of a qualitative insight into the information content of measurements in the oxygen A band.

2.5.2.1 Dependence on central wavelength

Figure 2.6 shows Ψ and d of the retrieval for the four test cases, using two channels with nominal resolution (solid lines, full width at half maximum fwhm$\approx$ 3.7 nm) and full spectral resolution (dashed lines, fwhm$\approx$ 1.6 nm). The first channel was fixed in the absorption free area at 753 nm ($\equiv$ MERIS channel 10), the second one was shifted through the O_2 A band. As can be seen from the left panel of figure 2.6, the information content Ψ has a maximum around 762 nm for the two cases with thick clouds (*b*), *d*)). Cases *a)* and *c)* (thin cloud) do not show a strong wavelength dependence of Ψ and have a significantly lower gain of information. This is to be expected, since MERIS is hardly sensitive to optically thin clouds. In all cases, a switch to higher spectral resolution does not change Ψ significantly.

The right panel shows the degrees of freedom d. As only two channels were used for the retrieval, the maximum possible value is 2. For thick clouds (cases *b)* and *d)*), d shows a strong dependence on the central wavelength of the absorption channel, with a maximum close to 2. This can be interpreted as an accurate measurement of two degrees of freedom, one respresenting the cloud optical thickness and the other one the mean photon path length that depends on both CTP and the cloud extinction profile. Cases *a)* and *c)* have significantly lower degrees of freedom with case *c)* (thin cloud, bright surface) showing higher values than case *a)* (thin cloud, dark surface). This can

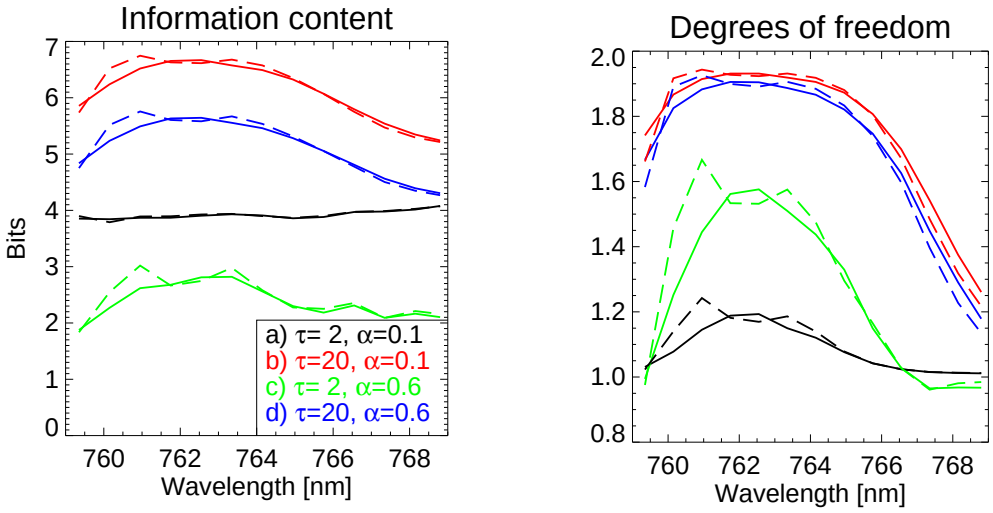

Figure 2.6: Information content (left panel) and degrees of freedom (right panel) for a two-channel retrieval of CTP, cloud optical thickness and cloud volume extinction as a function of spectral channel position. Dashed lines correspond to MERIS subpixel resolution (fwhm $\approx$ 1.6 nm), solid lines correspond to MERIS-like channel width (fwhm $\approx$ 3.7 nm).

be explained with the stronger signal over bright surfaces, suppressing the influence of noise. Since the surface albedo was assumed to be known precisely, the signal could be inverted successfully in this simulation study. In reality, where the surface albedo is only known to limited accuracy, a bright surface underlying optically thin clouds dominates the signal, leaving almost no sensitivity to cloud parameters.

2.5.2.2 Dependence on number of channels

Figure 2.7 shows the dependence of Ψ and d on the number of used channels within the oxygen A band. The first channel was again fixed outside of the absorption band and the absorption channels (fwhm$=$ 1.6 nm, $\Delta\lambda = 1.25$ nm) were added consecutively. At every step the gain of information was analysed for all remaining channels. The channel providing the highest gain of information was added to the measurement vector y.
The panels show a rise of both Ψ and d as the number of channels increases, in parts due to the cancellation of noise. The remaining increase is due to the slightly differing sensitivities of channels in the R- and P-branch to cloud-top pressure and cloud extinction. The good performance of cases *c)* and *d)* (bright surface) can again be explained with

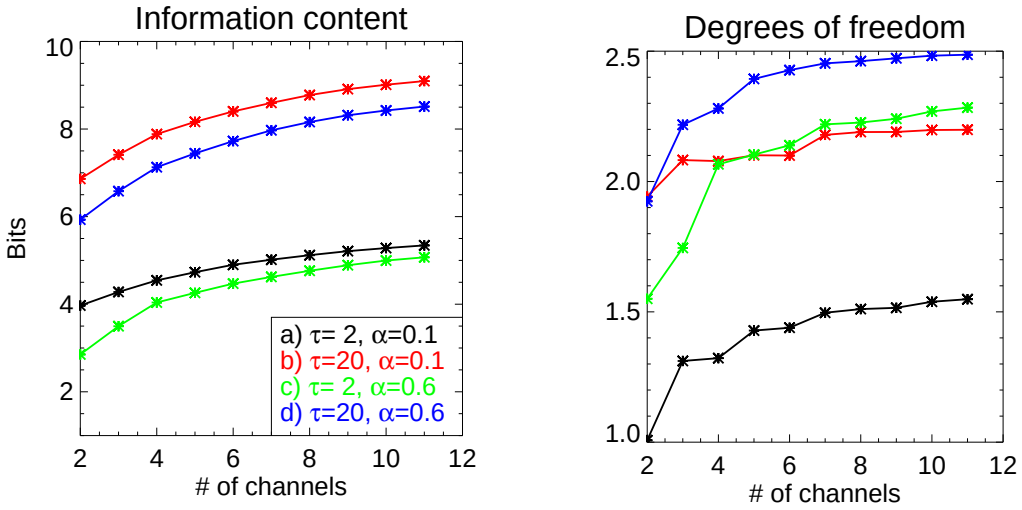

Figure 2.7: Information content (left panel) and degrees of freedom (right panel) for a retrieval of CTP, cloud optical thickness and cloud volume extinction as a function of the number channels within the oxygen *A* band.

the strong signal and the unrealistic assumption of a precisely known surface albedo. However, the maximal value of d is 2.55, indicating that CTP and cloud extinction can be separated to some extent if a sufficient number of channels inside the absorption band is used.

2.5.2.3 Dependence on channel width

Figure 2.8 shows the dependence of Ψ and d on the channel width. Eleven channels were used, one outside and ten inside the absorption band.
For all four cases, both parameters show only weak dependence on the channel width between 0.5 nm and 2 nm. This is to be expected, since the information required to separate the signals of CTP and extinction profile is hidden in the shape of the individual absorption lines (O'Brien and Mitchell (1992)). A spectral resolution higher than 0.1 nm is needed to resolve these effects.

2.5.2.4 Conclusion

The O_2 *A* band channel of MERIS is spectrally well designed, as it is placed in the region providing the highest information content regarding the retrieval of CTP. Additional

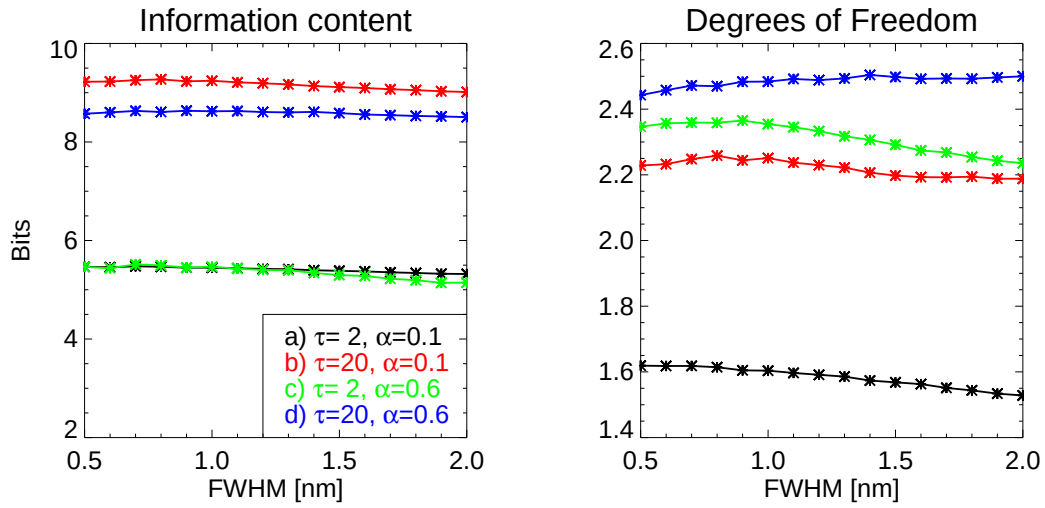

Figure 2.8: Information content (left panel) and degrees of freedom (right panel) for an eleven-channel retrieval of CTP, cloud optical thickness and cloud volume extinction as a function of channel width.

moderately resolving channels within the oxygen *A* band provide a limited increase of information about the vertical structure of clouds as compared to a single-channel retrieval. This is in parts due to the cancellation of noise with the remaining increase caused by the slightly differing sensitivities to CTP and geometrical thickness in the R- and P-branch of the oxygen *A* band. The maximum number of degrees of freedom of a multiple-channel measurement at a MERIS-like spectral resolution is between 2 and 3. The highly correlated signals of cloud height and geometrical thickness can thus be separated to a limited degree. A moderate increase of spectral resolution to a value of 0.5 nm does not significantly improve the retrieval.

2.6 Conclusion

Measurements within the oxygen *A* band, as provided by MERIS, show a high sensitivity to cloud-top pressure, except for optically thin cases above bright surfaces. In addition to CTP, the most important geophysical quantities that influence the measured transmission are the cloud optical and geometrical thickness and the surface albedo. As the surface albedo can be taken from surface reflectance data bases and the optical thickness can be estimated via the window channel brightness, the unknown geometri-

cal thickness of the cloud remains as a main source of error. The retrieval of CTP fails in the presence of dual-layered clouds unless one of the layers is optically very thin, as a single channel in the O_2 *A* band does not allow the separation of different cloud layers. The errors caused by the unknown temperature profile and cloud microphysics are irrelevant for the most part and less than 20 hPa in extreme cases. They are therefore of minor importance as compared to the other error sources. A further source of uncertainty is introduced by instrumental parameters, namely the spectral channel position and width, if not known with high precision. Depending on the channel position, an uncertainty of 0.1 Å in one of these quantities results in errors of up to 10 hPa. At a MERIS-like spectral resolution, these sensitivities vanish around 762 hPa, the region of maximum sensitivity to CTP. Thus, MERIS channel 11 is spectrally well designed, providing the maximum possible information content regarding the retrieval of CTP. The retrieval algorithm is implemented in the MERIS ground segment (Merheim-Kealy et al. (1999)). A validation campaign using airborne lidar measurements revealed an accuracy of 25 hPa in case of low, single layer clouds (Lindstrot et al. (2006)), which can be well explained with the findings stated above.

The use of additional channels within the oxygen *A* band is a way to achieve a gain of information about the height and extent of a cloud. At a MERIS-like spectral resolution, the maximum number of degrees of freedom of measurements in the O_2 *A* band is between 2 and 3, indicating that up to three independent pieces of information can be separated, namely the cloud optical thickness, the cloud-top pressure and the cloud geometrical thickness or mean extinction, respectively. However, since the signals of cloud-top pressure and geometrical thickness are highly correlated and the exact vertical profile of extinction is unknown, a residual uncertainty is unavoidable. An increase of spectral resolution to 0.5 nm does not improve the retrieval, as the information is hidden in the shape of the individual absorption lines with typical width of 0.1 nm.

The **O**cean and **L**and **C**olour **I**nstrument (OLCI) on board Sentinel-3 (Aguirre et al. (2007)), to be launched in 2012, will provide up to three spectral channels in the oxygen *A* band at a MERIS-like spectral resolution. Future measurements of the **O**rbiting **C**arbon **O**bservatory (OCO, Crisp et al. (2004)), providing hyperspectral measurements in the oxygen *A* band at a spectral resolution of 0.04 nm, will potentially allow the retrieval of information about the vertical profile of extinction and the detection of multilayer clouds.

A combination of MERIS measurements in the near infrared with observations in the thermal spectral region, as provided by the **A**dvanced **A**long **T**rack **S**canning **R**adiometer (AATSR, Huot et al. (2001)) on ENVISAT can help to improve the accuracy of the retrieval of cloud-top pressure. The synergistic use of measurements in the near infrared and thermal spectral regions will be further explored in the framework of the Sentinel-3 mission.

Acknowledgments

The authors thank J. Fischer for fruitful discussions and ESA for financial support under contract nr. 20693 / 07 / I-OL.

3 Validation of MERIS cloud-top pressure using airborne lidar measurements

---

Lindstrot, R., R. Preusker, T. Ruhtz, B. Heese, M. Wiegner, C. Lindemann, and J. Fischer, (2006), J. Appl. Meteor. Clim., 45 (12), 1612-1621.

Abstract

The results of a validation of ESAs operational MERIS cloud-top pressure product by airborne lidar measurements are presented. MERIS (**Me**dium **R**esolution **I**maging **S**pectrometer), mounted on the polar orbiting ESA-satellite ENVISAT, provides radiance measurements within the oxygen *A* absorption band around 762 nm. The exploitation of these data allows the retrieval of cloud-top pressure (herein after referred to as CTP).

The validation flights were performed in the north-eastern part of Germany between April and June 2004 and were temporally and spatially synchronized with the ENVISAT overpasses. The Cessna 207 T of the Freie Universität Berlin was equipped with the **Po**rtable **Li**dar **S**ystem POLIS of the Ludwig Maximilians Universität München and a GPS navigation system. The maximum flying altitude was around 3000 m, so the validation measurements were limited to situations with low-level clouds only. The validation was done by a comparison between MERIS and lidar data. The statistical analysis of the observations revealed a high accuracy of the MERIS CTP product for low-level clouds, apart from a slight systematic overestimation of cloud-top heights. The root mean square error resulted in 249 m with a bias of $+232$ m. In the average top height level of ~ 2000 m these values are commensurate to pressure values of 24 hPa (rmse) and -22 hPa (bias). Furthermore, this validation campaign revealed deficiencies of the MERIS cloud mask to detect small-scale broken clouds.

3.1 Introduction

Clouds and their physical properties like top height, droplet size and distribution as well as optical and geometrical thickness play a dominant role for the energy budget of the earth. However, the interactions between clouds and radiation are represented inadequately within current climate models. This is in part due to an insufficient understanding of the cloud-radiation interaction and the insufficient data basis available for the validation of the models (Houghton et al., 2001). It is therefore an important task for the remote sensing community to provide these information with a sufficient spatial and temporal resolution.

During the last decades several methods for the remote sensing of CTP were developed. The most common technique is the so-called 'CO_2-Slicing'-method (Wielicki and Coakley, 1981; Menzel et al., 1982, 2006), which uses the clouds emission within the CO_2 absorption band around $\sim 14\,\mu m$ to derive the cloud-top temperature. On the basis of temperature and humidity profiles the cloud-top height can be retrieved with an accuracy of $\sim 1.5\,km$ (Frey et al., 1999). Other techniques use the altitude-dependent shading of the earths surface by clouds (Gurney, 1982), or the parallax between two pictures of the same cloud taken from different viewing angles (Shenk and Curan, 1973; Hasler, 1981; Diner et al., 1998). A further method, which is applied to MERIS data, is based on measurements of the cloud-reflected solar radiation within the oxygen *A* band around 762 nm (Yamamoto and Wark, 1961; Fischer and Grassl, 1991). The latter technique is specified in section 3.2.1.

Since the launch of ESAs earth observation satellite ENVISAT (**Envi**ronmental **Sat**ellite) in march 2002, the oxygen *A* band method is applied to data of the imaging spectrometer MERIS (Fischer et al., 1997). In order to validate this CTP product, 12 validation flights were conducted in the north-eastern part of Germany between April and June 2004. A Cessna 207 T of the Freie Universität Berlin served as a measurement platform and was equipped with a GPS system and attitude sensors. On board the Cessna the **Po**rtable **Li**dar **S**ystem (POLIS) (Heese et al., 2002) was mounted to measure the cloud-top height. The comparison of POLIS and MERIS values revealed a high accuracy of the MERIS product for the examined days. The results are discussed in detail in chapter 3.3.

3.2 Instruments and techniques

3.2.1 MERIS cloud-top pressure retrieval

MERIS (**Me**dium **R**esolution **I**maging **S**pectrometer, Rast et al., 1999) is an imaging pushbroom spectrometer, that is mounted on the polar orbiting satellite ENVISAT. It is made up of five cameras, which are identical in construction and have a viewing angle of $\sim 14°$ each. The field of view of MERIS is 68.5°, corresponding to a swath of 1150 km over ground. The spatial resolution is 1000 m by 1200 m for the 'Reduced Resolution'-mode and 260 m by 300 m for the 'Full Resolution'-mode, which is available for a subset of scenes only. MERIS provides 15 spectral channels, programmable in width and position in the range of 390 nm to 1040 nm. Measurements of channel 10 at a wavelength of 753 nm and channel 11 at 761 nm are used to derive the cloud-top height (Fischer et al., 1997):

Solar radiation at a wavelength around 761 nm is partly absorbed by atmospheric oxygen. The strength of absorption depends on the mass of traversed air. In case of a reflecting cloud in the optical path, the absorption mainly takes place in the airmass above the cloud, determined by the cloud-top height. The strength of the absorption is therefore a measure for the airmass above the cloud and thus for the pressure at the cloud-top. In contrast to channel 11 the measurements of channel 10 are not subject to atmospheric gas absorption and can thus be taken as a reference. However, multiple scattering events within the cloud and between cloud and surface significantly increase the photon path lengths and therefore have to be considered.

The retrieval algorithm is based on the idea to interrelate the input parameters to the cloud-top pressure by a multi-dimensional nonlinear regression. The regression coefficients were determined by an Artificial Neural Network (ANN), described in detail in Fischer et al., 1997. Radiative transfer simulations with MOMO (**M**atrix **O**perator **Mo**del, Fischer and Grassl, 1984; Fell and Fischer, 2001) served as training data sets for the ANN. These simulations included a broad number of combinations of atmospheric parameters like temperature and humidity profiles, cloud heights and thicknesses, surface albedo values and aerosol loads.

The described technique is expected to provide accurate results in cases of optically thick, low clouds but to reveal weaknesses in cases of thin, high cirrus clouds and high

surface albedo values because of a strong impact of the mentioned multiple scattering between cloud and earth surface. In order to limit this uncertainty, the cloud optical thickness, derived from measurements of MERIS channel 10, and the surface albedo, taken from the GOME ground albedo data base, serve as additional input parameters to the retrieval algorithm. However, the albedo data base has a spatial resolution of merely 60 km by 60 km. Currently, a new surface albedo data base from MERIS data with a spatial resolution of 10 km by 10 km is under construction. An additional inaccuracy is caused by the uncertain length of the photon paths within the cloud. This 'penetration depth' could be determined if the geometrical extent and thus the extinction of the cloud were known. As this parameter can not be assessed by MERIS measurements, a global mean value of extinction is assumed by the algorithm. In cases where the actual cloud extinction is higher than this climatologically assessed mean, the cloud-top height is expected to be overestimated, as the penetration depth is smaller than assumed. In case the extinction is lower, the cloud-top height is underestimated. The expected accuracy of the method is 30 hPa for low clouds and exceeds 70 hPa for thin, high clouds (Fischer et al. (1997)). The presented algorithm to extract the cloud-top pressure is implemented in the MERIS ground segment (Merheim-Kealy et al., 1999).

3.2.2 POLIS cloud-top height retrieval

The portable lidar system POLIS was developed and constructed by the Meteorological Institute of the Ludwig-Maximilians-Universität München for groundbased and airborne operation (Heese et al., 2002). The light source is a Nd:YAG laser emitting pulses at 355 or 532 nm with a repetition rate of up to 20 Hz. The main components of the detection system are a Dall-Kirkham telescope of a diameter of 20 cm and a Licel acquisition system. In its standard configuration POLIS is operated in a two channel mode: two channels of mutually perpendicular polarization states at 355 nm, two channels at wavelengths 355 and 532 nm, or two channels including elastic and Raman backscattering at 355 and 387 nm, respectively. Due to its optical design and the close mounting of the laser on the telescope, POLIS provides backscatter signals already from approximately 70 m onward. This ability makes POLIS especially useful for cloud-top detection also close to the aircraft. The vertical resolution is 7.5 m. The instantaneous field of view of the receiving optics is 2.5 mrad, i.e., the diameter of a 'lidar pixel' at the cloud deck is

in the order of two meters. As backscattering from cloud droplets is significantly larger than backscattering from (background) aerosol particles, clouds can easily be identified by lidar signals on a single shot basis.
POLIS was mounted 'downward looking' into the Cessna 207 T of the Freie Universität Berlin. In the frame of this experiment, only one wavelength (355 nm) and a reduced pulse repetition frequency of 5 Hz were selected, providing sufficient information to accurately determine cloud-top heights. The cloud-top height was defined by that range bin that detected the maximum number of photons. In case of cloud free conditions the surface return in the lidar data was used to check the flight height as determined from the GPS system.

3.3 Experiment

3.3.1 Flights

The maximum flying altitude of the aircraft was around 3000 m, limiting the observations to low level clouds. Altogether 12 flights were conducted in the north-eastern part of Germany between April and June 2004. The overflown regions were mainly composed of vegetated and agriculturally used areas. The validation flights are arranged in four categories, depending on the cloud conditions (see Tab. 3.1).

3.3.2 Case studies

The validation of the ESA CTP product is carried out by a comparison between MERIS and POLIS measurements. However, the comparability of these datasets is limited by three dissimilarities, that have to be considered for the assessment of the results:

1. MERIS measurements are an average of a two-dimensional 1-km^2 area, whereas POLIS measurements form a one-dimensional trace of 'pinpoints' with a diameter of typically a few meters (depending on the distance between the aircraft and the cloud-top) and a separation of 10 m. The POLIS values thus had to be averaged over a distance of 1 km, which corresponds to a time slot of 20 s at an aircraft speed of $\sim 50\,\mathrm{ms}^{-1}$.

Table 3.1: Flight dates and cloud types.

Date	Cloud types
2004/04/20	Cumulus + cirrus
2004/05/03	Stratocumulus
2004/05/06	Cumulus + cirrus
2004/05/12	Stratocumulus
2004/05/18	Stratocumulus
2004/05/24	Stratocumulus
2004/05/25	Stratocumulus + cumulus
2004/05/26	Stratocumulus + cumulus
2004/06/03	Cumulus
2004/06/07	Stratocumulus
2004/06/11	Cumulus + cirrus
2004/06/16	Cumulus

2. Due to the different velocities of the satellite and the aircraft, POLIS measurements of the cloud field took more than one hour whereas MERIS radiances are obtained within a few seconds. The different measurements are thus to be considered as synchronous in terms of space but not in terms of time. To reduce the error which might occur when the clouds change with time, we only used measurements that are not separated more than ± 5 min in time for our intercomparison.

3. MERIS cloud-top pressure values were converted to cloud-top heights. Therefore temperature and pressure profiles from radiosondes of Lindenberg at 12 UTC of each day were used. The spatial and temporal distance to the aircraft measurements, which were spread across north-eastern Germany and took place between 9 and 11 UTC, introduces an additional inaccuracy of up to 2 hPa (~ 20 m in the considered lower atmosphere).
   The vertical resolution of the ESA MERIS CTP is approximately 4 hPa (~ 40 m), while it is 7.5 m for POLIS cloud-top heights. However, the accuracy of POLIS is dominated by the uncertainty of the GPS-determined flying altitude, which is in the range of $20 - 30$ m.

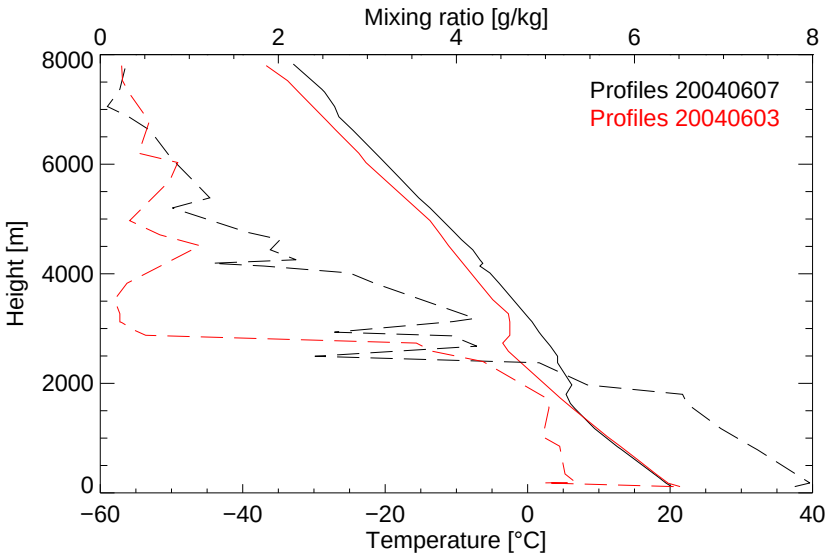

Figure 3.1: Temperature (solid lines) and humidity (dashed lines) profiles of the 7th of June (Stratocumulus, black) and the 3rd of June (Cumulus, red).

Figure 3.1 shows two representative vertical profiles of the atmosphere at Lindenberg. The stratocumulus case shows the typical temperature inversion at a height of ~ 2000 m with a corresponding rapid decrease of humidity in this layer. The cumulus case reveals a higher inversion (~ 3000 m), that allowed the development of convective clouds. However, the humidity in the boundary layer is lower than in the Stratocumulus case, causing the smaller amount of clouds (see Fig. 3.2 and 3.4).

In the following subsections the results depending on the different cloud types are discussed on the basis of representative case studies. To document the cloud conditions, a MERIS 'quasi true color image' of the scene and a photo taken from the aircraft are displayed in each case. Within the true color images there is the flight track plotted in red with the overpass interval marked in blue. The whole time series of the aircraft measurements is displayed below with the overpass time frame underlayed white and illustrated in detail underneath. In these figures the POLIS cloud-top height (black) values are compared with the value of the closest MERIS pixel (red).

3.3.2.1 Stratocumulus clouds

Observations related to this category took place in the presence of a closed stratocumulus cloud cover with a comparatively homogeneous top height. The 7th of June was chosen for a case study (Fig. 3.2). The displayed photo and the true color images give a rough idea of the cloud conditions. They show a smooth cloud layer without discontinuities.

The comparison of the measurements shows a very high agreement between cloud-top heights by MERIS and POLIS. Even the small-scale variability of the cloud-top height is reproduced accurately. However, MERIS does not correctly detect all clouds but misses some part of the cloud cover (e.g. 9:46 - 9:49 UTC). This deficiency probably results from a not properly working cloud mask (see section 3.3.2.3).

Apparently, the POLIS cloud-top height values are increasing during the flight, while the MERIS measurements stay on the same level around $1800 - 1900$ m. This is due to the mentioned different velocities of the satellite and the aircraft (see section 3.3.2). The steady rise of the cloud-top height observed by POLIS is due to the development of the clouds during the day. A similar effect can be observed in figure 3.3. Hence, the most significant measurements are those at the overpass time of MERIS. A time frame of ± 5 min of POLIS data around this moment was chosen as a data basis for the analysis. These time frames and the corresponding measurements are displayed at the bottom of each figure.

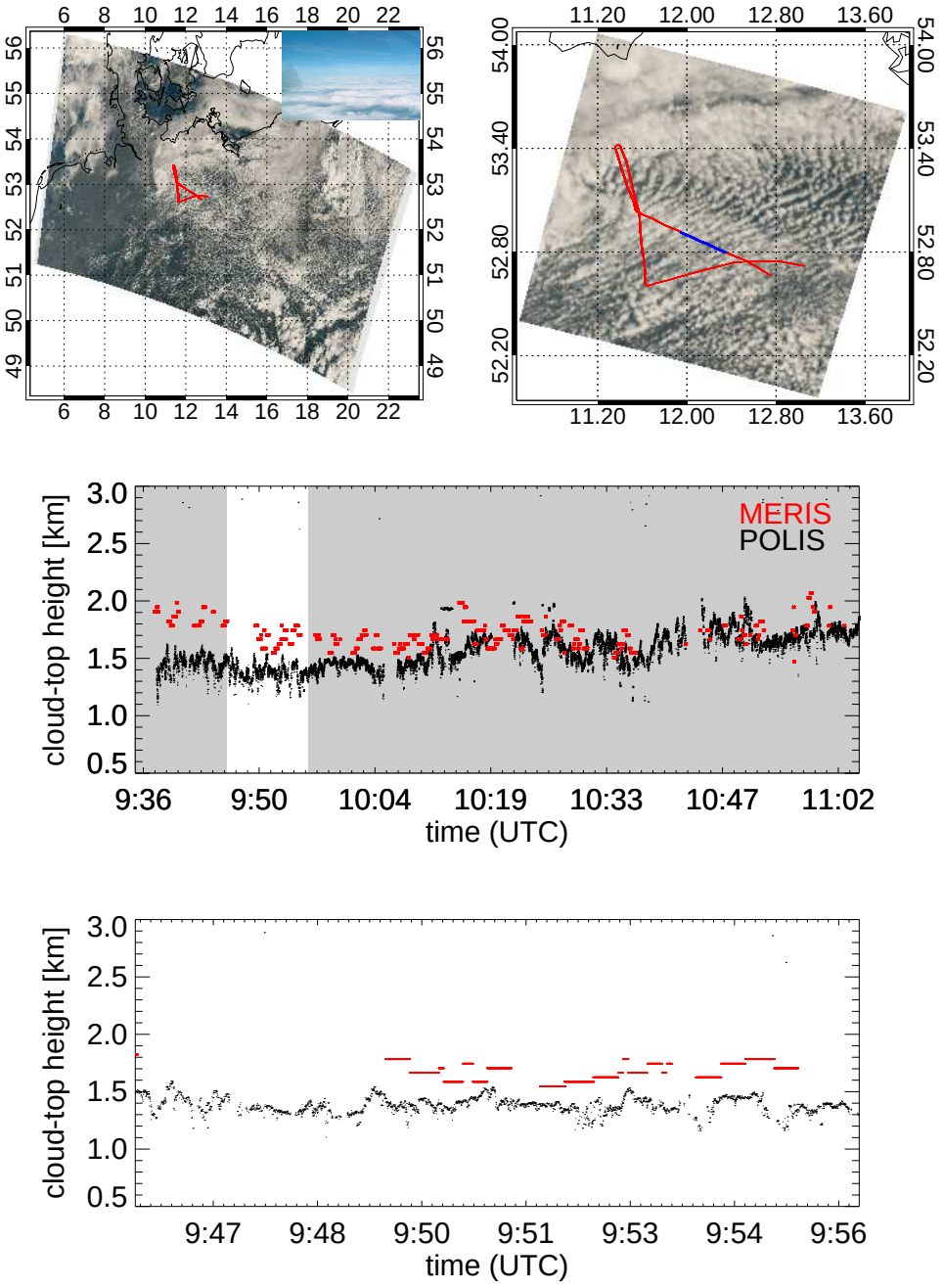

Figure 3.2: 2004/06/07, flight track and comparison of MERIS and POLIS.

3.3.2.2 Stratocumulus and cumulus clouds

This set of cases includes the observations with a mixture of stratocumulus and cumulus clouds. The cloud-top height is uneven because of penetrating cumulus tops. The 26th of May was chosen as a representative day (Fig. 3.3), for it perfectly matches the described criteria.

Again the comparison shows a high correlation between MERIS and POLIS values. Especially during the ENVISAT overpass the cloud-top heights and their small-scale structures are represented accurately by MERIS (e.g. 9:30 - 9:32 UTC). Here the overestimation of the cloud-top height by MERIS is in the range of $0-500\,\mathrm{m}$ ($0-40\,\mathrm{hPa}$ at a mean cloud-top height of 2.5 km). Again the development of the cloud-top height during the flight becomes apparent in view of the decreasing discrepancy between MERIS and POLIS measurements.

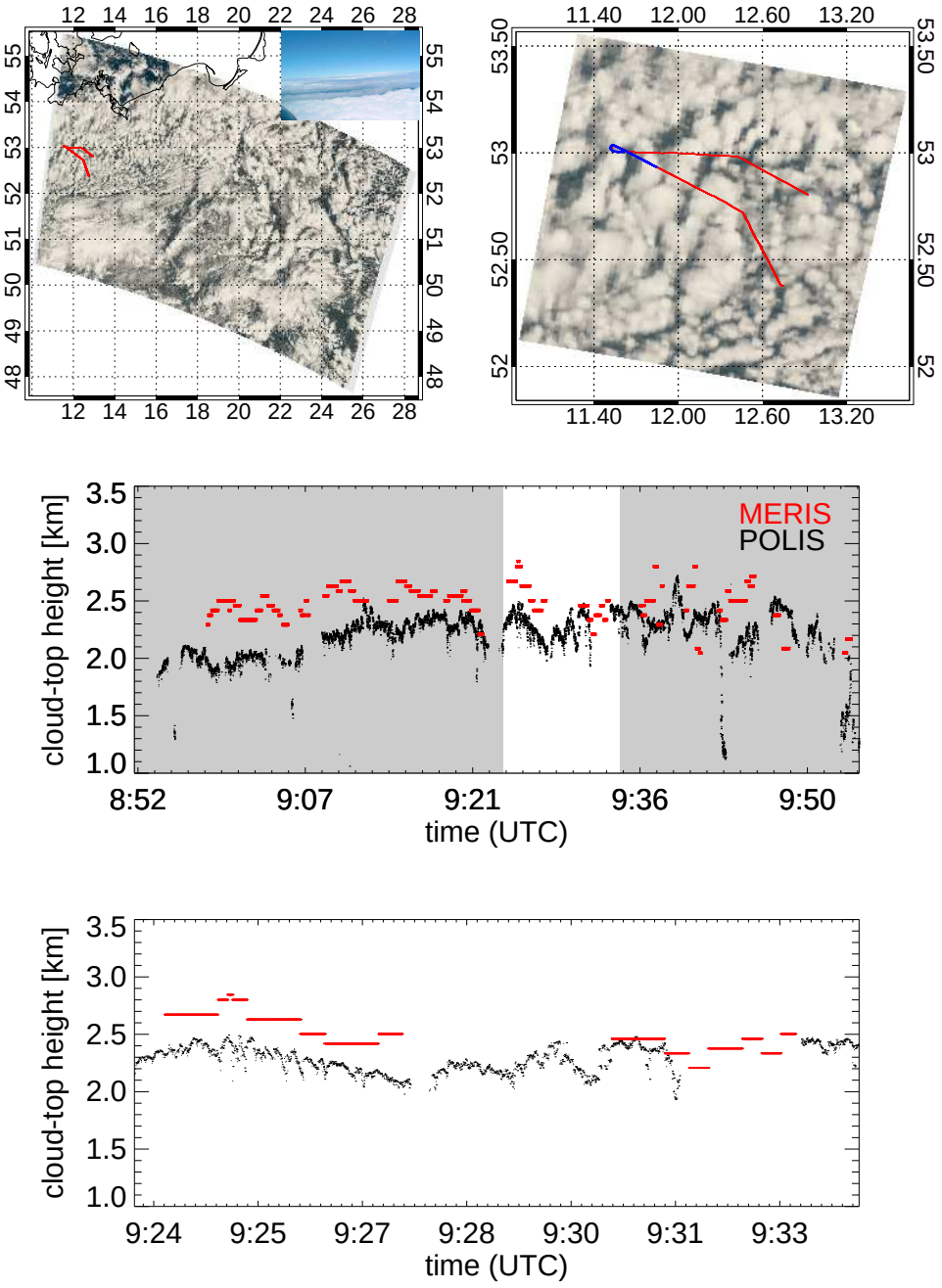

Figure 3.3: 2004/05/26, flight track and comparison of MERIS and POLIS.

3.3.2.3 Cumulus clouds

Observations related to this category took place in the presence of cumulus clouds with more or less broad gaps between the clouds. The measurements show a rather high variance of cloud-top height compared to the other cases.
The 3rd of June (Fig. 3.4), as a representative for this category, was only slightly clouded. The true color images show a field of scattered cumulus cells in the measurement area. Within the ENVISAT overpass time frame (10:11 - 10:21 UTC) there is only one clouded MERIS pixel (at 10:12 UTC) with a deviation of $300 - 400$ m from the POLIS value.
The dimensions of the cloud cells can be estimated from the POLIS data. They are partially at the limit of the resolution of MERIS and are thus not detected. Nevertheless the fraction of correctly identified clouds is too small. The ESA cloud mask takes into account several parameters like Rayleigh-corrected reflectances, derived surface pressure and cloud-top pressure values and returns a value that is 1 (clouded) or 0 (cloudless). This classification seems to be conservative for cloudy cases, i.e. the algorithm does not mistake clear pixels as cloudy. On the other hand the cloud mask obviously bares weaknesses in the identification of clouds, so that many pixels are classified as cloudless that should be classified as cloudy. This behaviour needs further investigation in order to find out if there is a dependency on the height of the classified clouds, that could lead to errors in further derived products.

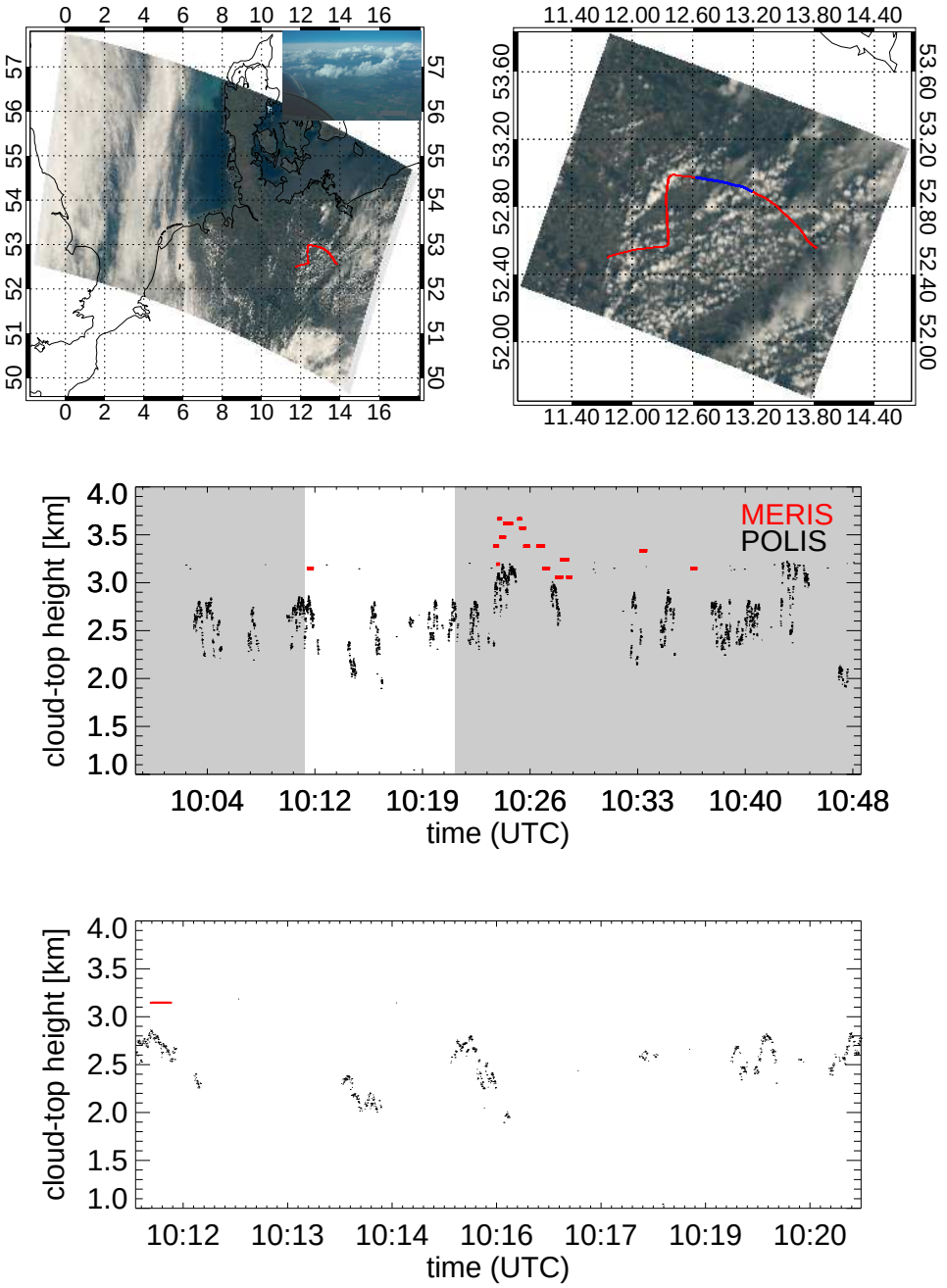

Figure 3.4: 2004/06/03, flight track and comparison of MERIS and POLIS.

3.3.2.4 Low-level and cirrus clouds

This set of days includes the cases with a presence of thin cirrus clouds above the examined cloud cover and the aircraft. They are thus not suitable for a validation of MERIS cloud-top heights.
The presence of a cirrus layer above the flight track can be guessed from the true color images of the 11th of June (Fig. 3.5), showing the characteristic untextured veil around the measurement area. This assumption was verified with quasi-simultaneous measurements of MODIS (**Mod**erate Resolution **I**maging **S**pectroradiometer). The photo diplays the low cumulus field below the cirrus layer and the aircraft.
The comparison of MERIS and POLIS observations shows the expected deviation of MERIS cloud-top heights towards too high values. Instead of representing the height of either the higher or the lower cloud layer, the MERIS-derived cloud height corresponds to an effective scattering height, located between the two cloud layers.

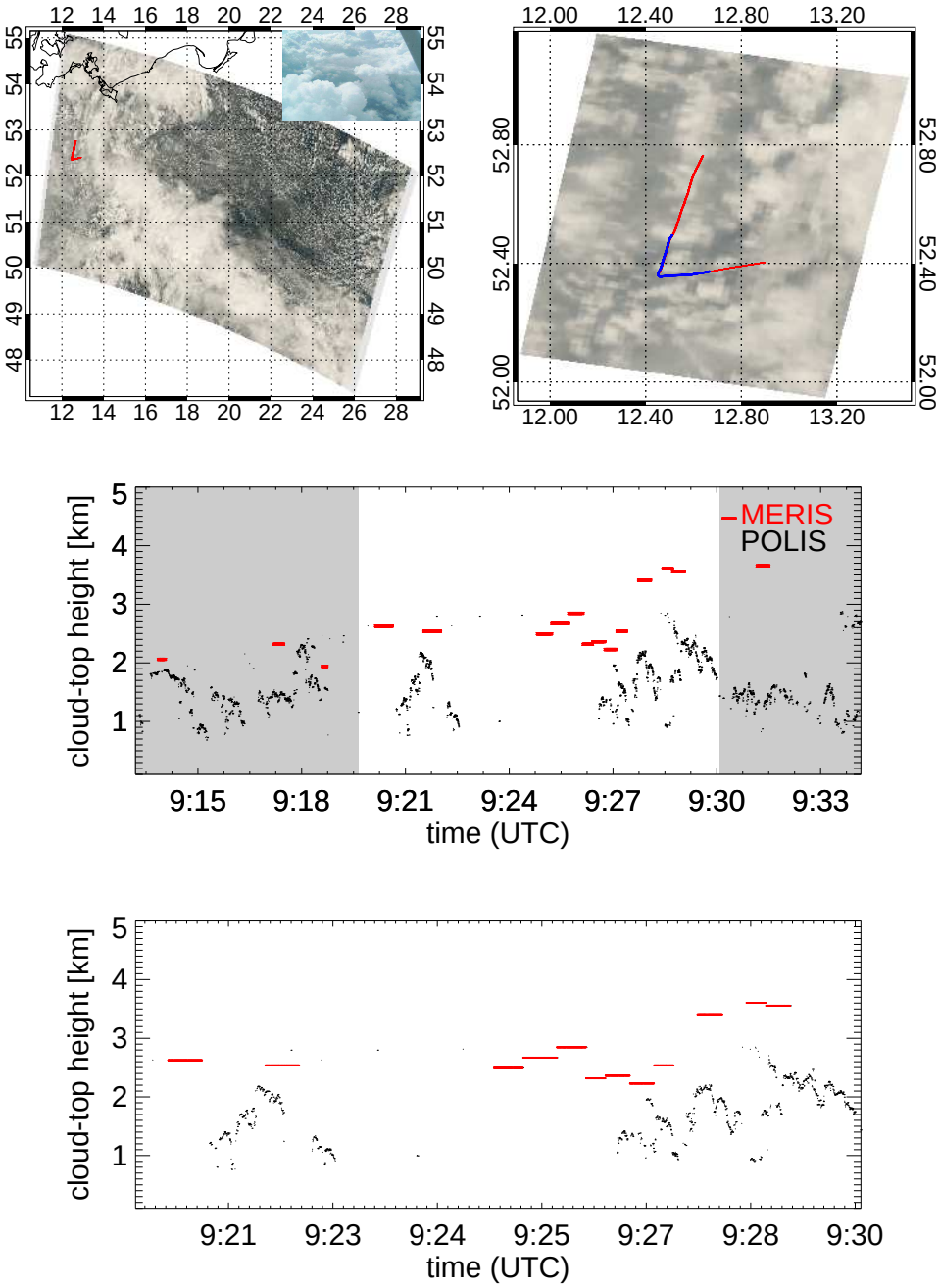

Figure 3.5: 2004/06/11, flight track and comparison of MERIS and POLIS.

3.3.3 Summary of validation experiment

The statistical analysis reveals a high accuracy of the cloud-top pressure product of MERIS. Figure 3.6 shows a scatterplot of 91 corresponding MERIS and POLIS values. The grey crosses mark the measurements in the presence of cirrus clouds. These observations were not included into the statistical analysis but are displayed here to document the deviation of MERIS cloud-top heights towards too high values. The error bars mainly result from the standard deviation of the 10 MERIS pixels located closest to the POLIS measurement position and the standard deviation of the POLIS cloud-top heights within the corresponding MERIS pixel, respectively. As mentioned, MERIS cloud-top pressure measurements were converted to cloud-top heights on the basis of radiosonde data from Lindenberg (52° 13'N, 14° 07'E) at 12 UTC. In order to account for the spatial and temporal distance between the MERIS measurements and the radiosonde ascents, gradients of air pressure in space and time were determined with additional radiosonde measurements at 6 UTC and data from Greifswald (54°06'N, 13°40'E) and Bergen (52° 49'N, 9° 56'E). The resulting deviations of up to 2 hPa ($\sim$ 20 m) were factored into the MERIS cloud-top height uncertainty for each case.
The statistical analysis reveals a root mean square error of MERIS of 249 m with a bias of $+232$ m, which corresponds to pressure values of 24 hPa and -22 hPa at a level of 2000 m. The tested retrieval algorithm thus systematically overestimates cloud-top heights. The 'bias-corrected' root mean square error is 90 m ($\simeq$ 9 hPa). The two datasets are highly correlated with a correlation coefficient of 0.97.

3.4 Conclusion

A validation of MERIS cloud-top pressure was accomplished by a comparison with airborne lidar measurements using the **Po**rtable **Li**dar **S**ystem. 12 validation flights were conducted in the north-eastern part of Germany between April and June 2004. A Cessna 207 T of the Freie Universität Berlin served as a measurement platform.
Apart from deficiencies of the MERIS cloud mask and a systematic underestimation of cloud-top pressure the validation campaign revealed a high quality of MERIS CTP. The accuracy was found to be 24 hPa with a bias of -22 hPa in cases of low clouds. The small-scale variability of cloud-top pressure can be resolved by MERIS. The presence

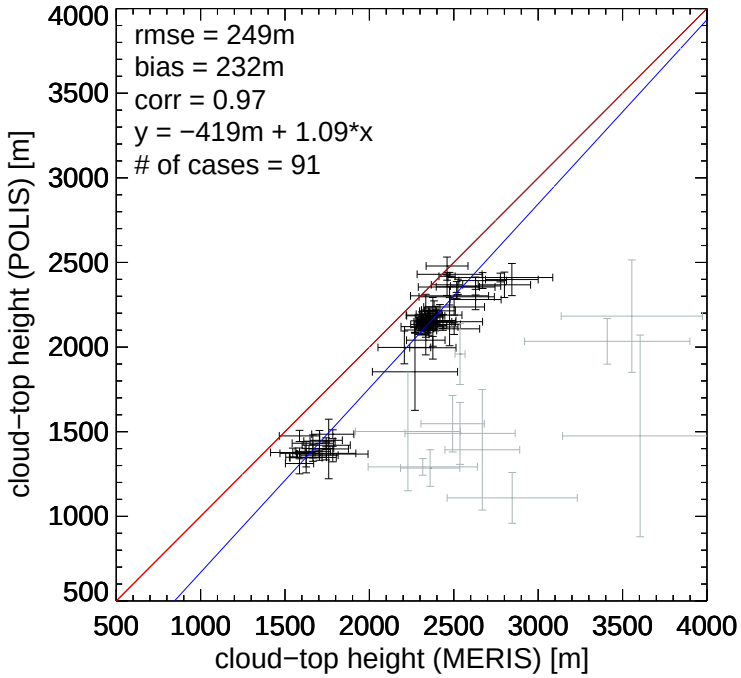

Figure 3.6: Comparison of POLIS- and MERIS-cloud-top heights. Grey crosses mark cases with presence of cirrus clouds. The one-to-one-line and the regression line are displayed in red and blue, respectively.

of thin cirrus leads to a significant decrease of the accuracy of MERIS CTP. This is due to the modification of the photon paths by scattering at the ice particles. Additional measurements, as provided by AATSR (**A**dvanced **A**long **T**rack **S**canning **R**adiometer) on ENVISAT will be used in future to identify cirrus clouds, in order to account for the mentioned effects. The critical optical thickness of a cloud needed to be "noticed" by MERIS can be estimated to $\tau \sim 0.5$. Further sensitivity studies are needed to assess the critical optical thickness needed by the algorithm to be able to correctly retrieve the height of cirrus clouds (see chapter 4).

The authors suppose that the observed systematic overestimation of cloud-top heights is caused by a too small extinction assumed by the algorithm (see section 3.2.1).

Further investigation is needed to define the effects of high surface albedo and differences between the individual cameras on the MERIS CTP product.

A similar validation study is planned for high clouds. As the flying height of the aircraft

used for this study is limited to 3000 m, this could be performed using lidar measurements of ICESAT (**I**ce, **C**loud and Land **E**levation **SAT**ellite, Zwally et al., 2002). The outstanding applicability of lidar for the determination of cloud-top heights will furthermore be exploited by the satellites CALIPSO (**C**loud-**A**erosol **L**idar and **I**nfrared **P**athfinder **S**atellite **O**bservations, Winker et al. (2004)) and EarthCARE (**Earth C**louds **A**erosols and **R**adiation **E**xplorer, Kondo et al., 2003). Both satellites will carry lidar instruments for the measurement of vertical profiles of aerosols and cloud-top heights. The oxygen *A* band method will be applied to data of the **O**rbiting **C**arbon **O**bservatory (OCO, Crisp et al., 2004) which is planned to be launched in 2008. The cloud-top pressure will be a byproduct used to determine the concentration of carbon dioxide in cloudy atmospheres with high accuracy.

Acknowledgements

The financial support for this campaign was granted by ESA/ESRIN (RFQ/3-10848/04/I-OL). Thanks for useful comments by M. Schröder.

4 Remote sensing of multilayer cloud-top pressure using combined measurements of MERIS and AATSR aboard ENVISAT

Lindstrot, R., Preusker, R. and Fischer, J., submitted to Journal of Applied Meteorolgy and Climatology (2009)

Abstract

A novel and unique algorithm for the retrieval of multilayer cloud-top pressure is presented, relying on synergetic observations of MERIS and AATSR onboard ENVISAT. The retrieval is based on the exploitation of the differing signals observed in the thermal infrared spectral region (AATSR) and the oxygen *A* band at 0.76 µm (MERIS). Past studies have shown that the cloud-top pressure retrieved fom MERIS measurements is highly accurate in case of low single-layered clouds. In contrast, in the presence of multilayered clouds like cirrus overlying water clouds, the derived cloud height is biased. In the frame of this work, an optimal estimation algorithm for the correction of the measured O_2 *A* transmission for the influence of the upper cloud layer was developed. The algorithm is best applicable in cases of optically thin cirrus ($1 \leq \tau \leq 5$) above optically thick water clouds ($\tau > 5$), as found frequently in the vicinity of convective or frontal cloud systems. The split window brightness temperature difference technique is used for the identification of suitable cases. The sensitivities of AATSR and MERIS measurements to multilayered clouds are presented and discussed, revealing that in case of dual-layered clouds, the AATSR-derived cloud height is close to the upper cloud layer, even if it is optically thin. In contrast, the cloud height retrieved from MERIS measurements represents the optical center of the cloud system which is close to the lower layer in case the upper layer is optically thin. Two case studies of convective, multilayered cloud systems above the Northern Atlantic are shown, demonstrating the plausibility of the approach. The presented work is relevant especially in view of the upcoming GMES Sentinel-3 satellite to be launched in 2012 that will carry the follow-up instruments OLCI (MERIS) and SLSTR (AATSR).

4.1 Introduction

Cloud systems appear to be multilayered frequently, especially if associated with convective clusters or frontal systems. In several studies low level clouds were found in ~50 % of cases where cirrus clouds were present (Fye (1978); Hahn et al. (1984); Mace et al. (1997)). Based on **N**ational **O**ceanic and **A**tmospheric **A**dministration's (NOAA's) **A**dvanced **V**ery **H**igh **R**esolution **R**adiometer (AVHRR) data, Heidinger and Pavolonis (2005) analyzed the global cloud overlap statistics. They concluded that between 60°N and 60°S, roughly 40 % of all ice clouds were classified as cirrus overlapping lower clouds. In a recent study, exploiting the measurements of the **C**loud-**A**erosol **L**idar and **I**nfrared **P**athfinder **S**atellite **O**bservations (CALIPSO), Mace et al. (2009) found that multilayered clouds were present in about 60% of the profiles recorded above the Tropical Western Pacific, Equatorial South America and Africa. Above the tropical ocean, the multilayered clouds systems were predominantely formed by cirrus above low-level clouds.

In contrast to these findings, most satellite-based algorithms for the retrieval of cloud properties rely on the assumption of single-layered clouds. This oversimplifying assumption results in errors in the derived cloud properties like e.g. the cloud-top pressure (hereafter referred to as CTP). The existing algorithms, if applied in multilayered cases, tend to derive either the height of one of the layers or return a height level located somewhere between the cloud layers. Thermal techniques, for instance, based on the exploitation of the emission of the cloud layers in the thermal infrared (hereafter referred to as TIR), are typically sensitive to the uppermost unit of optical depth (Holz et al. (2007)), as clouds are strongly absorbing in the infrared spectral region. In contrast, the height derived from observations within the oxygen A band at 0.76 µm is influenced by scattering at and within all cloud layers and thus rather represents an optical center of the cloud system than the cloud-top height of one of the cloud layers (Fischer and Grassl (1991); Wang et al. (2008)). The information retrieved by each of these single-layer approaches is both valuable but insufficient to properly describe the vertical distribution of clouds and thus the heating and cooling rates within the vertical column in case of cloud overlap. Past studies regarding the treatment of multilayer clouds were almost completely based on TIR-measurements and mostly limited to the detection of cloud overlap (e.g. Baum et al. (2003); Nasiri and Baum (2004)) and subsequent correction

of the contribution of the lower cloud layer to the measured signal (e.g. Baum et al. (1994); Baum and Wielicki (1994)). By pursuing this strategy, the accuracy of the derived cirrus height could be greatly improved, whereas the height of the lower layer was either not derived or determined by looking at cirrus-free regions in the vicinity (Chang and Li (2005b)). Since the mentioned approaches are either based on the CO_2-Slicing technique (e.g. Smith and Platt (1978); Wielicki and Coakley (1981); Menzel et al. (2006)), which is known to be unable to retrieve cloud properties of heights less than approximately 3km (Baum et al. (1995)), or a simple determination of the cloud-top temperature using the brightness temperature at 11 µm, the reliability of the derived low level cloud heights is limited.

The most promising approach to improve the retrieval in case of multilayer clouds is a combination of independent techniques, exploiting the differing sensitivities of separated methodologies to the individual cloud layers. This paper presents an approach to combine the measurements of MERIS (**Me**dium **R**esolution **I**maging **S**pectrometer) and AATSR (**A**dvanced **A**long **T**rack **S**canning **R**adiometer), two imaging, multi-spectral radiometers mounted on ENVISAT (**Envi**ronmental **Sat**ellite). Since both instruments perform measurements at a similar spatial resolution in overlapping fields of view and differing spectral regions, a synergistic retrieval of cloud-top height is possible using independent techniques, namely the oxygen *A* band method in case of MERIS and a retrieval based on the cloud's thermal emission in the TIR in case of AATSR. In order to demonstrate the difference of the individual retrievals, a comparison with spaceborne lidar and radar measurements as provided by CALIOP (**C**loud-**A**erosol **Li**dar with **O**rthogonal **P**olarization on board CALIPSO, Winker et al. (2009)) and CloudSat (Stephens et al. (2002)) was performed. Due to the differing satellite orbits of ENVISAT and the A-train, simultaneous cloud observations of MERIS/AATSR and CALIOP/CloudSat are rare and can only be found at high latitudes, limiting the informative value due to high solar zenith distance angles and the time difference between the satellite overpasses.

Figure 4.1 shows the comparison of CTP as derived from CALIOP and MODIS (**Mod**erate Resolution **I**maging **S**pectroradiometer on board AQUA) and the individual retrievals from MERIS and AATSR (only available between 71°N and 75.5°N due to narrow swath) measurements for a scene north of Scandinavia on July 31st, 2007, underlayed with the CloudSat radar reflectivity. Several conclusions can be drawn from

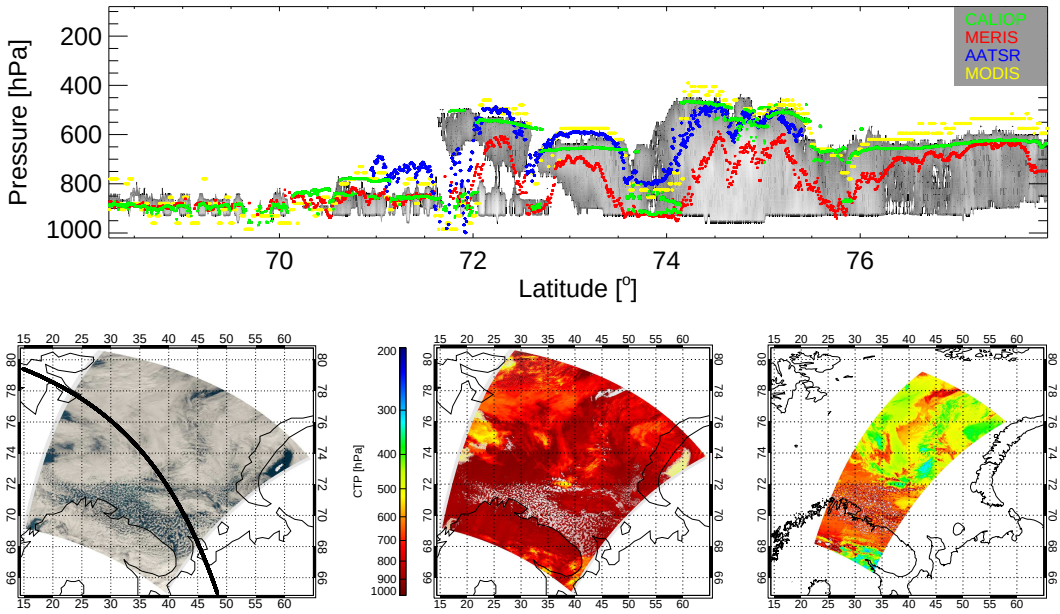

Figure 4.1: Comparison of CALIOP-, MODIS-, MERIS- and AATSR-derived CTP for scene north of Scandinavia on 2008/07/31, underlayed with CloudSat radar reflectivity. Bottom panels: MERIS-RGB with A-train track in black, (left, time gap between CALIPSO and ENVISAT: 9 minutes) and CTP for whole scene, as derived from MERIS (middle) and AATSR 11 µm BT (right).

the comparison:

1. The height of single-layered low level clouds is accurately determined using the MERIS oxygen *A* band technique (below 72° N). This finding is in agreement with earlier validation results (Lindstrot et al. (2006)). TIR-based retrievals like MODIS show a higher scattering here.

2. In case of vertically extended or mutlilayered cloud systems (above 72°N), the MERIS-derived cloud height is significantly too low. This can be explained with a strong influence of the unknown multiple scattering inside the cloud or between separated cloud layers.

3. TIR-based retrievals, like CO_2-Slicing (MODIS) or a simple determination of the cloud-top temperature using the 11 µm brightness temperature (AATSR), are

closer to the cloud-top. In case of multilayered clouds (~72°N - 73°N), the retrieved cloud height is close to the upper cloud layer.

4. In case of very low cloud extinction, as presumably present between 73.5° and 74°N where even CALIOP only detects a low cloud, the TIR-derived cloud height represents a level inside the cloud rather than the cloud top.

In view of the differing sources of signals observed by MERIS and AATSR, a synergistic cloud retrieval using these two independent data sets seems to provide a gain of information about the vertical structure of multilayered cloud systems. As the AATSR-derived cloud height corresponds to the upper cloud in case its optical thickness is large enough, it can be used for the correction of the transmission in the oxygen *A* band, as measured by MERIS. In the following, the synergistic observations of the two instruments are therefore used for the retrieval of CTP in cases of semi-transparent cirrus overlying warm water clouds, as identified by the 11 µm - 12 µm split window difference method.
Section 4.2 gives a short overview of the used instruments and the individual methodologies used for the retrieval of cloud height. Simulation studies regarding the sensitivity of MERIS and AATSR to multilayered cloud systems are shown in section 4.3. The approach for the synergistic retrieval, based on the detection of overlapping clouds using the split window technique and the subsequent determination of the layer heights within a full optimal estimation scheme, is presented in section 4.4. Section 4.5 contains two case studies of multilayered, convective cloud systems above ocean.

4.2 Instruments and methods

4.2.1 MERIS

MERIS is a programmable, medium-spectral resolution, imaging spectrometer (Rast et al. (1999)). It is one of ten core instruments on the polar orbiter ENVISAT, flying at 800 km in a sun-synchronous orbit with an equator crossing time of 10:30AM, descending node, and 98.5° inclination. MERIS consists of 5 identical pushbroom imaging spectrometers operating in the solar spectral range (390 to 1040 nm), arranged in a fan shape configuration which covers a total field of view of 68.5° and spans a swath width

of around 1150 km. The spectral dispersion is achieved by mapping the entrance slit of a grating spectrometer onto a CCD array. The integration time, instrument optics and CCD array resolution are adjusted such that MERIS has a spatial resolution of 260 m * 300 m and a spectral sampling of 1.25 nm. The instrument electronic data rate provides 15 channels between 400 and 900 nm which are programmable by ground command in width and in position. In the regular operation mode the spatial resolution is reduced by a factor of 4 along and across track (reduced resolution mode). In the full resolution mode, the full spatial resolution is transmitted.
The algorithm for the retrieval of CTP from MERIS measurements utilizes a radiance ratio of the channels 10 at 753 nm and 11 at 761 nm, allowing for the approximation of the transmission in the O_2 *A* band, which is a function of mass of oxygen. Since oxygen is well mixed in the atmosphere, the traversed mass of oxygen is equivalent to the traversed mass of air. Above clouds, the measured air mass is a function of the well known viewing geometry and the cloud height. Determining the cloud optical thickness using the window radiance at 753 nm allows for the estimation of the in-cloud multiple scattering, causing an extension of the average photon path length. The theoretical basics of the retrieval algorithm are detailed in Fischer and Grassl (1991) and Preusker and Lindstrot (2009) (see chapter 2). The algorithm is operationally applied within the MERIS ground segment. The retrieval was validated using airborne lidar measurements of cloud-top height, revealing an accuracy of 25 hPa in case of low level, single-layered clouds (Lindstrot et al. (2006), see chapter 3). However, the retrieval is known to be biased in case of multilayered or vertically extended clouds, in case the cloud extinction is under- or overestimated, as detailed in section 4.3.

4.2.2 AATSR

AATSR, the **A**dvanced **A**long **T**rack **S**canning **R**adiometer (Huot et al. (2001)), is a dual view, conically scanning radiometer, primarily designed for the remote sensing of sea surface temperature. Like MERIS, AATSR is mounted on ENVISAT, providing measurements in 7 spectral channels between 0.55 µm and 12 µm in a 500-km nadir swath at a spatial resolution of 1 km at nadir. AATSR measurements allow the retrieval of cloud-top height from two different techniques. The first one is based on the stereo view, exploiting the height-dependent parallax of the cloud when looked at from dif-

ferent angles (Muller et al. (2007a)), the second, applied in the frame of this work, is purely based on the measurement of the thermal emission of the cloud at 11 µm, allowing for the determination of the cloud-top temperature. At a wavelength of 11 µm the atmosphere is transparent to electromagnetic radiation, apart from a weak absorption by water vapour. In contrast, clouds are strongly absorbing at this wavelength range, causing the signal observed in the AATSR 11 µm channel to originate from the emission in the top part of the uppermost cloud layer. This assumption is fulfilled in case the cloud is optically thick ($\tau \gtrsim 1$), as will be shown in section 4.3. In the following, the cloud-top temperature is thus determined from the measured brightness temperature at 11 µm and converted to CTP using vertical temperature profiles. This simple approach was chosen, as the measurements of AATSR lack further important information about clouds obtainable from channels in the CO_2 absorption band around 15 µm. The so-called CO_2-Slicing technique, as applied to e.g. MODIS (Smith and Platt (1978); Wielicki and Coakley (1981); Menzel et al. (2006)), provides better sensitivity to semi-transparent cirrus clouds and their optical properties and is thus superior to a simple 11 µm brightness temperature based retrieval, especially if applied in cases of cirrus overlapping water clouds (e.g. Chang and Li (2005b)).

4.3 Sensitivity studies

In order to study the influence of multilayered clouds on the retrieval of CTP from TIR- and O_2 *A* band-measurements, simulation studies were performed, using MOMO (**M**atrix **O**perator **Mo**del, Fischer and Grassl (1984); Fell and Fischer (2001)) for simulating the MERIS-measurements in the solar spectral range. RTTOV9.1 (**R**adiative **T**ransfer for (A)**TOVS**, Saunders et al. (2008)) has been used for simulating the thermal infrared measurements of AATSR.

4.3.1 MOMO simulations

MOMO is a radiative transfer model based on the matrix operator method, designed for simulations of the radiative transport in the solar spectral range. Assuming a plane-parallel atmosphere, media of any optical thickness with any vertical inhomogeneity as well as any spectral resolution can be considered by MOMO, whereas three dimensional

effects can not be simulated. An advanced k-distribution technique is used to calculate the gaseous absorption in the atmosphere (Goody and Young (1989); Bennartz and Fischer (2000)). These calculations were based on the HITRAN 2004 data set (Rothman et al. (2005)), providing shape and strength parameters of the single absorption lines of the main atmospheric gases. The scattering properties of the liquid clouds were caluclated using a Mie code, assuming an effective particle size of 15 µm. The scattering properties of the ice clouds were calculated using the bulk scattering models provided by Baum et al. (2005a,b), assuming effective particle sizes of $r_{eff}^{ice} = 35$ µm, 55 µm and 78 µm, respectively. Both cloud layers were assumed to have a cloud fraction of 1.

4.3.2 RTTOV simulations

RTTOV is a radiative transfer model for fast calculations of top of atmosphere radiances for a range of space-borne infrared and microwave radiometers. It allows the simulation of top-of-atmosphere radiances, brightness temperatures and layer-to-space plus surface-to-space transmittance for each channel and given input atmospheric profile. RTTOV is widely used for the simulation of infrared and microwave radiances. A detailed description of the model can be found in Saunders et al. (2008) and references therein.

The cloud setup for the simulation of AATSR radiances with RTTOV was arranged in consistence with the MOMO setup. As in the RTTOV input profiles clouds are described with respect to their liquid and ice water content, the visible optical thickness of the lower cloud layer τ_{liq} was converted to liquid water path LWP using

$$LWP = 2/3 * \tau_{liq} \rho_l r_{eff}^{liq}$$

with $\rho_l = 1000\,\mathrm{kgm}^{-3}$ the density of liquid water and $r_{eff}^{liq} = 15$ µm. A parameterization proposed by Heymsfield et al. (2003) was used to calculate the ice water path IWP of the cirrus layer from the visible optical thickness τ_{ice} of the ice cloud:

$$IWP = \tau_{ice}[g_0(1 + g_1/g_0) * 1/r_{eff}^{ice}]^{-1}$$

with $g_0 = 0.01256$ and $g_1 = 0.725$ two empirical constants. In accordance with the MOMO simulations, the effective radius of the ice particles was set to $r_{eff}^{ice} = 35$ µm,

55 µm and 78 µm, respectively. Both cloud layers were assumed to have a cloud fraction of 1.

4.3.3 Sensitivity to multilayered cloud systems

The operational algorithm for the retrieval of CTP from MERIS measurements in the oxygen *A* band is based on a single-layer assumption, as the information needed for the discrimination of single-layered and multilayered cloud systems is not available from MERIS spectral channels. In case the observed cloud system is in fact multilayered, the retrieved CTP is the particular level of a virtual single-layered cloud resulting in the same average photon path length as the multilayered cloud system. The dependence of this effective single-layer height (hereafter referred to as CTP_{SL}^{MERIS}) on the properties of the multilayered system is shown in figure 4.2 (dashed lines). Here the combined visible optical thickness of the two cloud layers is held constant at $\tau_{total} = 50$, whereas the distribution of optical depth among the layers is modified along the x-axis. Apparently, an optically thin ice cloud ($\tau_{ice} \leq 5$) above an optically thick low cloud ($\tau_{liq} = \tau_{total} - \tau_{ice} \geq 45$) causes an extension of the average photon path length, resulting in a retrieved single-layer height even lower than that of the bottom cloud layer. This is due to a predominance of the path-extending effect of multiple scattering of photons between the cloud layers as compared to the shielding effect of the high cirrus. In case the optical thickness of the system is evenly distributed among the cloud layers, the effective single-layer height is located between the actual layers. Even an optically thin layer underlying an optically thick layer causes CTP_{SL}^{MERIS} to be biased. The effective single-layer height additionally depends on the viewing geometry with low zenith distance angles causing a strengthening of the path-extending effect and high zenith distance angles supporting the path-shortening effect (see grey lines). A detailed discussion of photon paths in cloudy atmospheres is given in Bennartz and Preusker (2006).

The corresponding TIR effective cloud height is the particular level of a virtual single-layer cloud that results in the same brightness temperature measurement as the dual-layered cloud system. In order to find CTP_{SL}^{AATSR} in multilayered cases (shown in figure 4.2, solid lines), the emission of the same cloud system was simulated for the AATSR TIR channels using RTTOV.

Several conclusions can be drawn from figure 4.2:

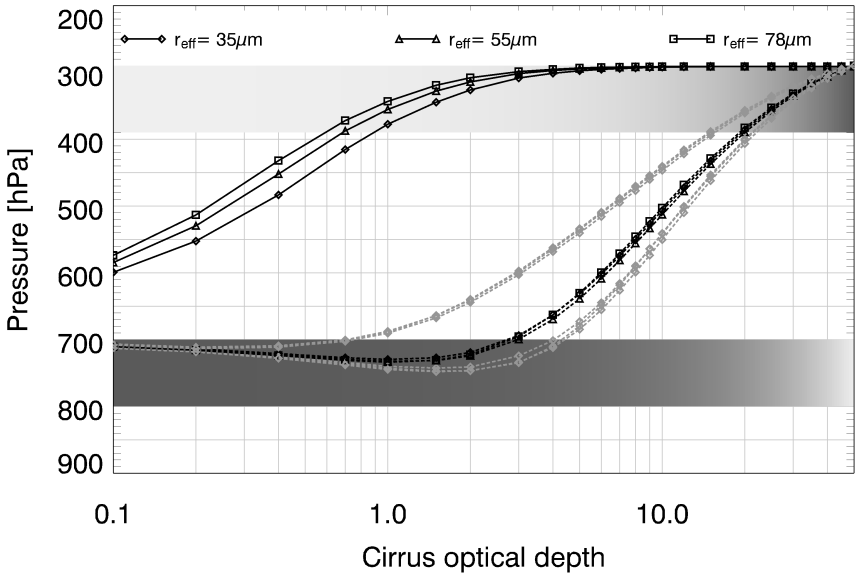

Figure 4.2: Effective single-layer cloud height as derived from AATSR 11 µm-BT (solid lines) and MERIS O_2 *A* transmission (dashed lines) in case of double-layered cloud system ($CTP_{DL1} = 290$ hPa, $CTP_{DL2} = 700$ hPa) with constant combined optical thickness of 50, depending on upper layer optical thickness. Both cloud layers are vertically homogeneous, upper cloud is composed of ice particles (r_{eff} as indicated in figure), lower cloud is composed of liquid water ($r_{eff} = 15\,\mu$m). Results are shown for viewing zenith angle of 10°. MERIS retrieval shown for solar zenith angle of 60° (upper grey lines), 15° (lower grey lines) and for average of effects for all solar zenith angles (15°$\leq \theta_{sun} \leq$60°, black lines).

1. CTP_{SL}^{AATSR} is very sensitive to even optically thin cirrus clouds. For $\tau_{ice} \gtrsim 1$, there is no significant influence of lower level emissions.

2. There is a weak dependence of the AATSR-sensitivity on the particle size of the cirrus layer. For small particles, the sensitivity to the cirrus is slightly reduced. The MERIS retrieval is hardly affected by the effective particle size of the cirrus.

3. In case of very thin cirrus ($\tau_{ice} < 1$), CTP_{SL}^{AATSR} is significantly biased towards a level located between the two cloud layers. On the other hand, for optically thick ice clouds ($\tau_{ice} > 5$), the MERIS-derived cloud height is very sensitive to the

unknown τ_{ice}. For these cases, the information provided by MERIS and AATSR is not sufficient to determine the height of both cloud layers.

4. In the range of $1 \leq \tau_{ice} \leq 5$, the AATSR-derived height corresponds to the cirrus whereas the MERIS retrieval is dominated by the lower layer signal. In these cases it is therefore possible to synergistically use the two instruments for the simultaneous retrieval of both layer heights. Without any correction of the cirrus influence on the O_2 A transmission, the lower layer height is slightly biased.

5. For $\tau_{ice} \leq 5$, CTP_{SL}^{MERIS} depends only weakly on the exact value the cirrus optical depth takes. By making a reasonable assumption about the cirrus optical depth, the MERIS-derived lower level height can be corrected for the cirrus influence on the O_2 A transmission. For different solar angles, the cirrus effect on the O_2 A transmission is stronger (see grey lines), necessitating the correction.

Figure 4.2 only shows the sensitivity of the retrieved effective cloud height on the ice cloud particle size. There is hardly any influence of the lower cloud particle size on the MERIS CTP retrieval, as demonstrated by Preusker and Lindstrot (2009). In summary, the retrieval of CTP of two overlapping cloud layers is possible using MERIS and AATSR in cases of optically thin ice clouds ($1 \leq \tau_{ice} \leq 5$) above optically thick water clouds ($\tau_{liq} > 5$), whereas there is a lack of information in case the cloud system has a different characteristic. Following Chang and Li (2005a), who globally analyzed the optical properties of single-layered and overlapping clouds, the described situations correspond to a significant fraction of multilayered clouds. In overlapping cases, they found a mean visible cirrus optical thickness of $\tau_{ice} \approx 1.5$ overlying water clouds with a latitude-dependent mean optical thickness between 8 and 30. The split window brightness temperature difference technique can be used for the identification of suitable cases, as will be shown in section 4.4.1.

4.4 Algorithm description

4.4.1 Detection of multilayer cases

The exploitation of the split window brightness temperature difference between 11 µm and 12 µm is a well established technique for general cloud classification (e.g. Inoue

(1987)) and the detection of cirrus overlapping water clouds (e.g. Ou et al. (1996)). As described by Pavolonis and Heidinger (2004), measurements at three different spectral ranges are needed, namely at 11 µm, 12 µm and in an atmospheric window in the visible or near infrared, as e.g. 0.66 µm. Due to the spectral dependence of the ice and water absorption coefficients, above clouds there is a brightness temperature difference between 11 µm and 12 µm. The so-called split window difference decreases with increasing cloud optical thickness but in general is larger in case of separated cloud layers than in case of single-layered clouds. In contrast, the visible reflectance at 0.66 µm as a first approximation only depends on the cloud system's total optical thickness, no matter whether it is single- or double-layered. The combined knowledge of the visible reflectance and the split window difference above clouds therefore allows for the identification of overlapping cloud layers. Figure 4.3 shows the split window difference $\Delta T = BT_{11} - BT_{12}$ depending on the visible reflectance $R_{0.66}$ for four different overlapping and non-overlapping cloud systems. The results for an ice cloud with $0.1 \leq \tau_{ice} \leq 10$ above a liquid cloud with $\tau_{liq} = 5$, 10, 20 and 40 (Cases A, B,

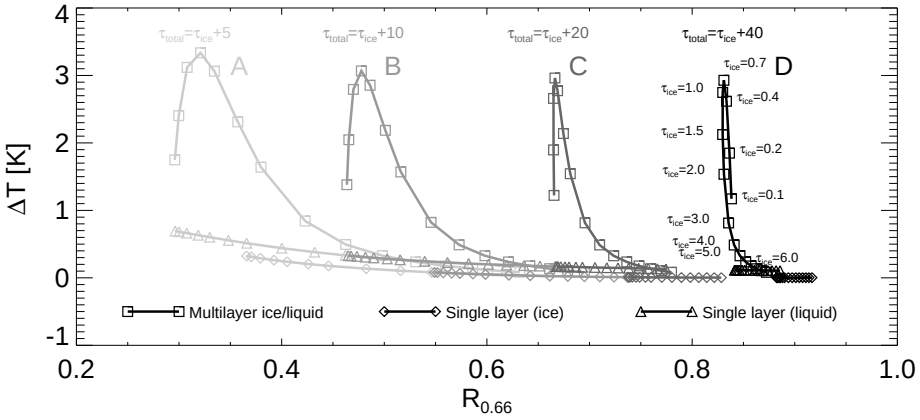

Figure 4.3: Split window brightness temperature difference $\Delta T = BT_{11} - BT_{12}$, depending on visible reflectance at 0.66 µm, for 4 cases of single-layered and double-layered clouds with variable optical thickness. Shown with squares: Cirrus optical depth varies from $\tau_{ice} = 0.1$ to $\tau_{ice} = 10$ above liquid cloud with optical thickness of $\tau_{liq} = 5$, 10, 20, 40 (Cases A, B, C, D, light grey to dark grey). Shown with diamonds and triangles: ΔT in case of single-layered ice or liquid cloud with corresponding combined optical thickness.

C, D, shown with squares) are compared with the corresponding results for a single-layered ice (diamonds) and liquid (triangles) cloud with the equivalent combined optical thickness (Case A: $5.1 \leq \tau_{ice,liq} \leq 15$, Case B: $10.1 \leq \tau_{ice,liq} \leq 20$, etc.). Apparently, multilayered clouds are separable from single-layered liquid and ice clouds using the split window technique in case the upper layer is optically thin. The threshold τ^*_{ice} for detectability slightly depends on the lower layer optical thickness and varies between $\tau^*_{ice} \approx 4$ and $\tau^*_{ice} \approx 6$ for liquid clouds between $\tau_{liq} = 5$ and $\tau_{liq} = 40$. Ice clouds with an optical thickness larger than τ^*_{ice} above liquid clouds are not distinguishable from single-layered liquid or ice clouds. The lower threshold of τ_{ice} for detectability is below 0.1 for all considered cases. It should be noted here, that the method is not sensitive to cases of ice clouds above optically very thin water clouds ($\tau_{liq} < 1$), as single-layered ice clouds result in a similar split window difference. The detected cases therefore represent optically thin ice clouds above optically moderately thick to thick water clouds.
The split window difference provides only little information on the cirrus optical depth, as ΔT peaks for $\tau_{ice} \approx 0.7$ and is ambiguous elsewhere. E.g., a cirrus with $\tau_{ice} = 0.1$ is not distinguishable from a cirrus with $\tau_{ice} = 2$, using the split window difference technique.
Pavolonis and Heidinger (2004) provide thresholds for ΔT depending on the visible reflectance $R_{0.66}$ and the viewing geometry that allow for the detection of cloud overlap. The thresholds have been developed for the AVHRR sensors onboard the NOAA satellites. In order to apply these thresholds to the measurements of AATSR, radiative transfer simulations have been performed to find the deviations in visible reflectance and brightness temperature caused by the different spectral response functions of the 0.66 µm, 11 µm and 12 µm channels of AATSR and AVHRR. Although the 0.66 µm channel of AVHRR is spectrally much wider than the AATSR channel, there is no significant difference in observed reflectance due to the absence of gaseous absorption and the fact that cloud properties are spectrally independent within this spectral range. Figure 4.4 shows the difference in brightness temperature at 11 µm and 12 µm as observed by AATSR and AVHRR (NOAA-17) for a two-layered cloud system, depending on the upper layer visible optical thickness. The brightness temperatures observed by AATSR are slightly lower than those of AVHRR. Since the deviation has the same sign and is almost similar at 11 µm and 12 µm, the resulting difference in ΔT does not exceed 0.08 K and is therefore negligible. Following these results, the thresholds developed for

AVHRR were assumed to be valid for AATSR as well.

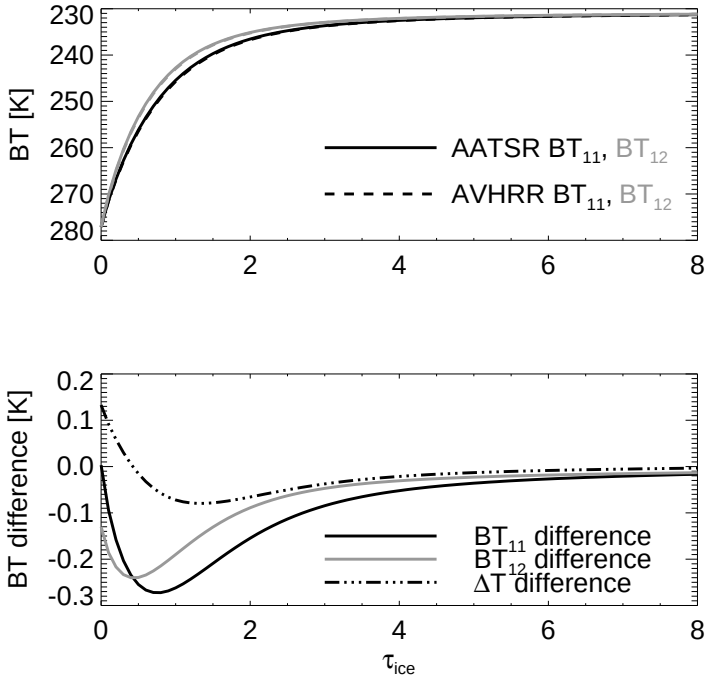

Figure 4.4: Brightness temperature at 11 µm and 12 µm as measured by AATSR and AVHRR for ice cloud ($0 \leq \tau_{ice} \leq 8$) above liquid cloud ($\tau_{liq} = 30$) and resulting difference in split window brightness temperature difference ΔT.

4.4.2 Optimal estimation

The algorithm introduced here is based on the operational MERIS CTP retrieval logic, briefly introduced in section 4.2 and described in detail in Fischer and Grassl (1991) and Preusker and Lindstrot (2009). It was extended to account for multilayer cloud systems using synergistic observations of MERIS and AATSR and implemented using an optimal estimation technique. The algorithm was designed for the retrieval of multilayer CTP in case of optically thin ice clouds ($0.5 \leq \tau_{ice} \leq 4$) above optically thick liquid clouds ($5 \leq \tau_{liq} \leq 200$).

The elements of a 4-elemental state vector, namely the height and optical thickness of the two cloud layers, are adjusted by matching the simulated and measured channel ratio of MERIS bands 11 and 10. As the AATSR-derived CTP in multilayered cases is

close to the upper layer top height (see section 4.2.2), it is used as a proxy for the cirrus height. The assumed cirrus optical thickness is predefined to a value between $\tau_{ice} = 1$ and $\tau_{ice} = 4$. The two remaining elements of the state vector, the lower layer top height and optical thickness are adjusted using an optimal estimation technique. In the frame of this paper, only a brief overview of the optimization theory can be given. An in-depth discussion can be found in Rodgers (2000).

In retrieval theory concepts the state vector x usually denotes the atmospheric parameters to be retrieved. Assuming a linear behaviour within the error bounds of the retrieved state, the state vector can be related to the measurement vector y, containing all available, individual measurements, via the weighting function $\mathbf{K}$ (Jacobian matrix) and a random error vector ε. This can be written as

$$y - y_0 = \mathbf{K}(x - x_0) + \varepsilon$$

for an arbitrary linearisation point, defined by x_0 and y_0. Since $\mathbf{K}$ can usually be assumed to behave linearly only in a small range around the actual state, the true state x can not be determined directly. Instead, iterative methods like optimal estimation have to be applied.

Prior to any measurement, a background knowledge x_a about the state vector x is given, potentially provided by independent measurements. If there is no additional source of information, the lowest possible level of knowledge about x is provided by the climatological means of the retrieval parameters, with the climatological variances representing the accuracy of this knowledge. Analogously, assumptions about measurement errors like radiometric noise are made. Within the optimization scheme, the measurement and background error covariances are compiled in the measurement error covariance matrix $\mathbf{S}_\varepsilon$ and the background error covariance matrix $\mathbf{S_a}$. Starting from a first guess given by the prior knowledge x_a, the state vector x is adjusted iteratively using

$$x_{i+1} = x_i + S_i(\mathbf{K}_i^T \mathbf{S}_\varepsilon^{-1}(y - F(x_i)) + \mathbf{S_a^{-1}}(x_a - x_i))$$

with $S_i = \mathbf{K}_i^T \mathbf{S}_\varepsilon^{-1} \mathbf{K}_i + \mathbf{S_a^{-1}}$ and $F(x)$ representing the simulated measurement, based on an assumed state x. The calculation of the weighting function $\mathbf{K}$ and the forward simulation $F(x)$ are repeated within each iteration step during the minimization of the error measure

$$\chi^2 = (y - F(x))^T \mathbf{S}_\varepsilon^{-1} (y - F(x)) + (x_a - x)^T \mathbf{S}_a^{-1} (x_a - x)$$

χ^2 thus represents the deviation between $F(x)$ and y, weighted with the measurement accuracy, and x and x_a, weighted with the prior knowledge accuracy, respectively.
In our case, the state vector x is composed of four elements, two cloud layer heights and two optical depths, whereas the measurement vector y only contains two radiances of MERIS bands 10 and 11:

$$x = [CTP_{DL2}, \tau_{DL2}, CTP_{DL1}, \tau_{DL1}]$$

$$y = [L_{10}^{MERIS}, L_{11}^{MERIS}]$$

In order to solve this ill-posed problem, CTP_{DL1} was fixed to the AATSR-derived value and the cirrus optical depth τ_{DL1} was set to a value between 1 and 4, leaving only two free parameters, CTP_{DL2} and the lower layer optical depth τ_{DL2}. This was realized by properly defining the prior knowledge x_a and simultaneously setting the prior knowledge uncertainty close to zero for the two fixed parameters. In simple words, assuming the cloud system to be double-layered, the upper layer was forced to the AATSR-derived height with a fixed optical thickness whereas the lower layer height and optical thickness were optimized to match the MERIS O_2 A measurement with the simulation.

4.4.3 Neural network forward operator

The forward operator used within the Optimal Estimation framework is based on the **M**atrix **O**perator **Mo**del (MOMO, see section 4.3.1 and Fischer and Grassl (1984); Fell and Fischer (2001)).
The atmospheric profiles serving as input to MOMO were defined by the US standard atmosphere (McClatchey et al. (1972)) and contained two cloud layers, an optically thin cirrus layer and an optically thick water cloud layer underneath. In analogy to the cloud setup assumed in the sensitivity studies, the scattering properties of the cloud layers were calculated using a Mie code in case of the lower layer, assumed to be purely composed of liquid droplets ($r_{eff} = 15\,\mu m$). The scattering properties of the modelled cirrus clouds were taken from the bulk scattering properties provided by Baum et al. (2005b),

assuming an effective particle size of $r_{eff} = 55\,\mu m$. Both cloud layers were assumed to be vertically homogeneous with a constant cloud volume extinction of $20\,km^{-1}$ for the liquid cloud and $5\,km^{-1}$ in case of the cirrus cloud. These simplifying assumptions were made as both the actual cloud microphysical composition and the vertical extinction profile are unknown and highly variable in reality. As this study was purely aimed at testing the feasibility of a two-layer retrieval approach, the algorithm was kept as simple as possible.
In order to achieve a both fast and accurate MERIS O_2 *A* forward operator, as needed within the optimal estimation scheme, an Artificial Neural Network (ANN) was trained to perform the forward simulation. ANNs are used in a wide field of remote sensing applications. If trained and applied properly, they are fast and accurate tools for both the inversion of satellite measurements and the forward simulation (e.g. Krasnopolsky (2007)). The data base for the training of the ANN was created by a large number of MOMO simulations, covering the whole range of variation of all parameters of interest. The input to the ANN is composed of the two cloud layer heights, the two cloud layer optical depths, the viewing geometry and the center wavelength of MERIS channel 11. The output is the TOA radiance in MERIS channels 10 and 11.

4.5 Case studies

The proposed two-layer retrieval of CTP has been applied to two case studies. Extended convective cloud systems above the Northern Atlantic were selected and tested for cloud overlap using the split window technique. The pixels of MERIS and AATSR were binned on the same spatial grid using a nearest neighbour technique.
Figures 4.5 and 4.6 each show a MERIS RGB image of the scene and the multilayer flag for those pixels identified as cloudy by both MERIS and AATSR (top row). The retrieved layer heights are shown in the middle row, the distance of the retrieved layers in the bottom left panel. A section plot along the track indicated in the layer distance plot is shown in the bottom right panel. The derived cirrus heigth CTP_{DL1} is shown in blue and the derived lower layer height CTP_{DL2} in red to yellow, depending on the assumed cirrus optical depth τ_{ice}.

4.5.1 Case study I: 26th September, 2005

Figure 4.5 shows the results for an extended convective storm system over the Northern Atlantic. The RGB image indicates the presence of cirrus, blown off the top of the convective storm center, above low level clouds in the outer regions of the cloud system. This hypothesis is supported by the cloud overlap test that was only applied to pixels with a visible reflectance $R_{066} \geq 0.3$ and $CTP_{SL}^{AATSR} \leq 500\,\text{hPa}$ to limit the analysis to optically thick cases in the presence of high clouds. The retrieved layer heights for the hypothetical upper and lower cloud layer are shown for all pixels where the retrieval converged (non-convergence is shown in dark grey). In general, the distance between the retrieved layers increases towards the outer parts of the cloud system, which is in agreement with both the impression given by the RGB image and the knowledge about the structure of convective cloud systems. The distance is close to zero in the convective storm center where the clouds are either single-layered or the upper layer is optically thick and therefore does not qualify for the proposed multilayer retrieval, as indicated by the cloud overlap flag. The layer distance is up to 400 hPa towards the boundaries of the cloud system. Apparently the cirrus shield covers the whole north-eastern part of the scene, however, low level clouds are detected only for some areas, e.g. around $-49.5°$ longitude, $38.8°$ latitude. Here the presence of both cirrus and low level clouds is clearly visible in the RGB image as well. Between $-51°$ and$-52°$ longitude, $36°$ and $37°$ latitude, there are some zones of non-convergence, showing that the simplified two-layer model is not applicable here, which is in agreement with the cloud overlap flag indicating a single cloud layer. The section plot (bottom right panel) clearly shows the differing behaviour of the dual layer retrieval in the center and the outer parts of the cloud system. In the region identified as dual-layered the layers are vertically seperated whereas similar heights are retrieved in the single-layered parts. There is a weak dependence on the assumed cirrus optical depth, as predicted by the multilayer sensitivity studies (see section 4.3).

Figure 4.7 (left panel) shows a scatter plot of MERIS single-layer retrieval CTP_{SL} and the retrieved lower layer height CTP_{DL2} for those pixels identified as double-layered, assuming a cirrus optical depth of 2. The comparison of the two retrievals shows no bias and a root mean square deviation of 24 hPa. A maximum bias of -40 hPa with a rmsd of 50 hPa is found when a cirrus optical depth of 4 is assumed (right panel).

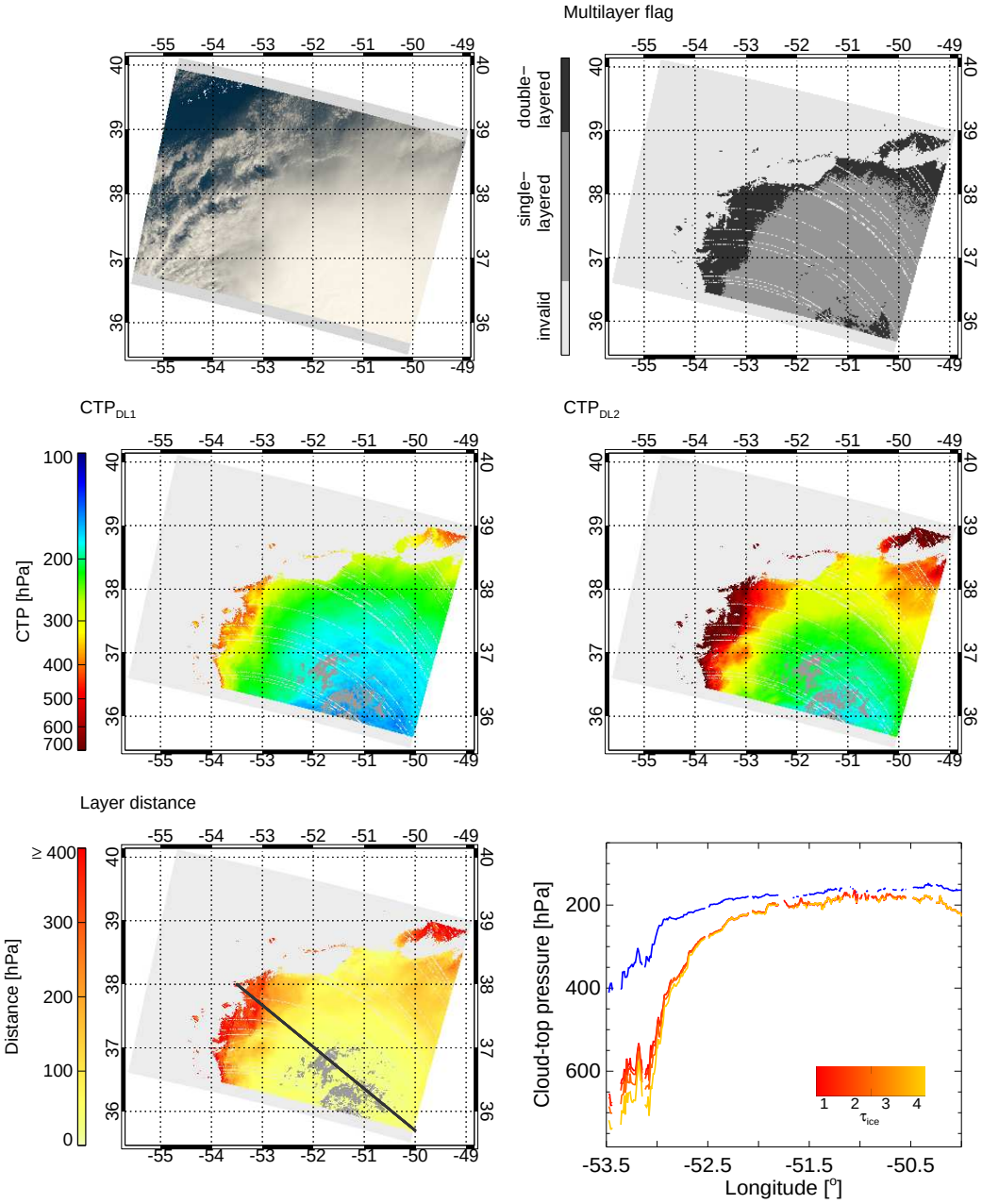

Figure 4.5: Case study of storm system above Northern Atlantic on 26th September, 2005. RGB image and multilayer flag shown in upper row. Retrieved upper and lower layer height shown in middle row. Layer distance and section plot along indicated leg shown in bottom row. Colors in section plot belong to derived cirrus height (blue) and derived lower layer height, depending on assumed cirrus optical depth (red to yellow).

4.5.2 Case study II: 29th August, 2005

The second case study is a more chaotic scene in the same geographic area on the 29th of August, 2005. The RGB image shows multiple cells of deep convection surrounded by the cirrus anvils blown off the tops of the individual cells. The multilayer flag indicates single cloud layers in the vicinity of the convective cloud-tops and a more extended area around $-50°$ longitude, 35° latitude with a presumably optically thick upper cloud layer. The retrieved layer heights show spots of non-convergence in the centers of the convective cells, where the two-layer assumption is not applicable, surrounded by zones of low layer distance. This behaviour can be followed in the section plot, showing the biggest layer distance in the southern part of the track (33.6° - 34.2° latitude), similar layer heights for the convective cells at 34.3° and 34.7° latitude and moderate layer distances in the northern part ($> 35°$ latitude). The latter is flagged as single-layered for the most and is presumably covered by optically thick cirrus clouds. The comparison of the derived lower layer height with the MERIS single-layer retrieval (figure 4.7, middle panel) shows a bigger bias (24 hPa) as compared to case study I, dropping to 5 hPa in case a cirrus optical depth of 4 is assumed. These differing results are caused by the fact that the effect of cirrus on the O_2 *A* transmission depends in a complex way on the viewing geometry, the optical thickness and the vertical separation of the two cloud layers and results in a predominance of one of the competing effects of shortening or extending the average photon path length.

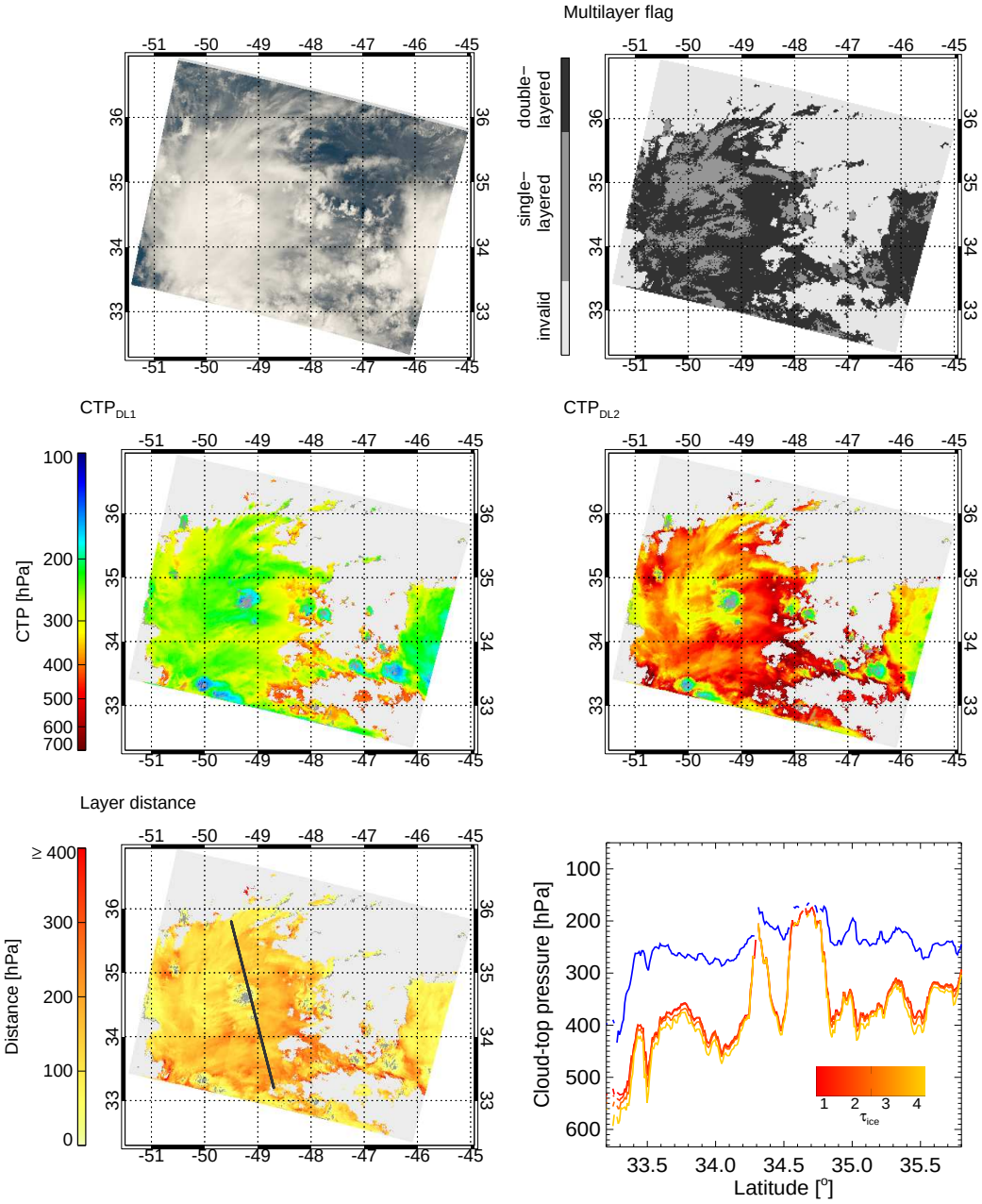

Figure 4.6: As for figure 4.5, for case study on 29th August, 2005.

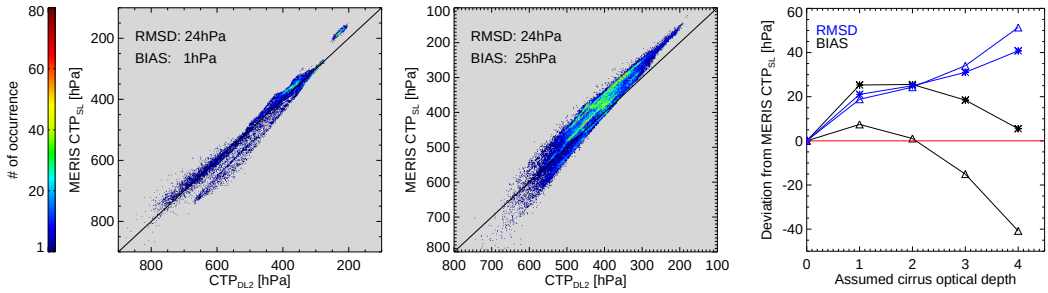

Figure 4.7: Scatter plots of MERIS single-layer derived CTP_{SL}^{MERIS} and lower layer derived height CTP_{DL2} for pixels identified as multilayered, for case study I (left panel) and II (middle panel) for assumed cirrus optical depth of 2 and dependency of root mean square deviation and bias on assumed cirrus optical depth for case study I (triangles) and II (asterisks) (right panel).

4.6 Conclusion

The combination of different techniques for the retrieval of cloud-top pressure provides a gain of information about the vertical structure of cloud systems. By combining the observations of AATSR in the thermal infrared spectral region and MERIS in the oxygen *A* band at 0.76 µm, the retrieval of mutlilayer cloud-top pressure is possible in cases of cirrus above optically thick liquid clouds. Suitable cases can be identified using the split window brightness temperature difference technique, exploiting the visible reflectance at 0.66 µm, and the difference of the brightness temperatures observed at 11 µm and 12 µm. The proposed retrieval algorithm thus represents a unique tool for the retrieval of multilayer CTP, based on data of passive, imaging satellite instruments. The retrieval is limited to cases of cirrus optical depth $1 \leq \tau_{ice} \leq 5$, as in case of optically thick cirrus the influence on the O_2 *A* transmission measured by MERIS is uncertain and the AATSR-derived cloud height represents a level located between the cloud layers in case of very thin cirrus. Additional information is needed here, as could e.g. be provided by multiple, spectrally highly resolving channels inside the oxygen absorption band or additional channels in the carbon dioxide absorption band around 15 µm.

The proposed retrieval scheme was successfully applied to two case studies of extended convective cloud systems above the Northern Atlantic. The derived layer heights corre-

spond well with the split window multilayer flag, showing large layer distances where the cloud system was identified as multilayered and low layer distances where it was classified as single-layered. As there are no active lidar or radar measurements for the retrieval of cloud height available from ENVISAT, a quantitative validation of the retrieved layer heights is not possible. Airborne lidar measurements on board the **H**igh **A**ltitude and **Lo**ng Range Research Aircraft (HALO) will enable validation campaigns from 2012.

The measurements of MERIS and AATSR will be continued by the follow-up instruments OLCI (**O**cean and **L**and **C**olour **I**nstrument) and SLSTR (**S**ea and **L**and **S**urface **T**emperature **R**adiometer) onboard the GMES Sentinel-3 satellite to be launched in 2012 (Aguirre et al. (2007)). Since OLCI will provide additional channels inside the oxygen *A* band, the retrieval of cloud-top pressure of single- and multi-layered clouds will be further developed and improved. Currently, the retrieval is hampered by the lack of knowledge about the cirrus optical depth. An exploitation of the stereo view provided by AATSR / SLSTR can help to separate the signals of cirrus and underlying low level clouds, as proposed by Gonzalez et al. (2002).

The proposed retrieval scheme can in principle be transferred to combined measurements of MODIS and POLDER (**Pol**arization and **D**irectionality of the **E**arth's **R**eflectances) instrument on board the A train satellite PARASOL (**P**olarization and **A**nisotropy of **R**eflectances for **A**tmospheric **S**ciences coupled with **O**bservations from a **L**idar). POLDER performs measurements in two spectral channels within the oxygen *A* band that can be used for a CTP determination similar to the MERIS retrieval scheme. Since the CO_2 slicing algorithm applied to MODIS radiances shows a higher sensitivity to optically thin cirrus as compared to the simple 11 µm brightness temperature retrieval, a more accurate retrieval seems possible, hampered however by the limited spatial resolution of POLDER ($6 * 6\,km^2$).

Acknowledgments

This work was funded by DFG (reference nr. FI 435/15-1). The authors thank Andrew Heidinger and Martin Stengel for useful comments and advise.

5 The retrieval of land surface pressure from MERIS measurements in the oxygen *A* band

---

Lindstrot, R., R. Preusker, and J. Fischer, (2009), J. Atmos. Oceanic Technol., 26 (7), 1367–1377.

Abstract

Measurements of MERIS (**Me**dium **R**esolution **I**maging **S**pectrometer) on ENVISAT (**Envi**ronmental **Sat**ellite) are used for the retrieval of surface pressure above land and ice surfaces. The algorithm is based on the exploitation of gaseous absorption in the oxygen *A* band at 762 nm. The strength of absorption is directly related to the average photon path length, which in clear sky cases above bright surfaces is mainly determined by the surface pressure with minor influences from scattering at aerosols.
Sensitivity studies regarding the influences of aerosol optical thickness and scale height and the temperature profile on the measured radiances are presented. Additionally, the sensitivity of the retrieval to the accuracy of the spectral characterization of MERIS is quantified. The algorithm for the retrieval of surface pressure (SP_{FUB}) is presented and validated against surface pressure maps constructed from ECMWF sea level pressure forecasts in combination with digital elevation model data. The accuracy of SP_{FUB} was found to be within 10 hPa above ice surfaces at Greenland and 15 hPa above desert and mountain scenes in Northern Africa and Southwest Asia. In a case study above Greenland the accuracy of SP_{FUB} could be enhanced to better than 3 hPa by spatial averaging over areas of 40 km * 40 km.

5.1 Introduction

The development of an algorithm for the retrieval of surface pressure from satellite based observations is of great interest due to its potential to fill the gaps of surface based measurement networks. Representing one of the main driving quantities of the weather on earth, a precise knowledge of the global distribution of surface pressure is an important input parameter for weather models. The remote sensing of surface pressure from space is on the other hand a highly ambitious task because of the precision needed: In order to be of any use as model input data, the accuracy of a retrieval algorithm should be in the range of 1 hPa ($\equiv 0.1$ % at 1000 hPa, Bengtsson (1979)). The air pressure at a given location on the earth surface is determined by the mass of air in the vertical column above. In order to measure this mass from space, the "differential absorption technique" can be applied, which is based on exploiting spectral gaseous absorption features. The absorbing gas has to be well mixed in the atmosphere and moderately absorbing in the spectral range under consideration in order to allow the determination of the air mass traversed by the detected photons. Using a band with too much absorption results in saturated absorption bands that do not carry any information about photon path length, whereas a weak absorption band does not provide enough sensitivity. Therefore, the oxygen *A* band at 762 nm perfectly qualifies for a retrieval of surface pressure, since

1. oxygen is moderately absorbing at this particular spectral range, is well mixed and has a constant concentration in the atmosphere.

2. the absorption band is undisturbed by absorption of other atmospheric species or emission of the atmosphere or the earth.

Various authors have outlined the potential usefulness of measurements in the oxygen *A* band for the retrieval of surface pressure (Barton and Scott (1986); Mitchell and O'Brien (1987); O'Brien and Mitchell (1989)). The method has been applied to measurements of POLDER by Breon and Bouffies (1996), who tried to use the deviation of the "apparent pressure", derived on a clear sky assumption, as an indicator for cloud appearance. They found an accuracy of apparent pressure of 100 hPa. O'Brien et al. (1998) found more promising results using an airborne grating spectrograph with high spectral resolution, directed towards sun glint areas above ocean. Using two channels with moderate

spectral resolution ($\Delta\lambda = 0.5$ nm) they found an accuracy of 20 hPa, whereas a use of highly resolved spectra ($\Delta\lambda = 0.05$ nm) allowed the determination of surface pressure with a precision of 1 hPa. The difference in accuracy appears due to the fact that spectrally highly resolved measurements enable a separation of the fractions of signal that are caused by reflection at the surface and in the atmosphere, whereas a single channel in the oxygen *A* band only provides one piece of information, namely the average photon path length.
MERIS (**Me**dium **R**esolution **I**maging **S**pectrometer) onboard ENVISAT, primarily designed for ocean color remote sensing, provides measurements in 15 channels between 0.4 µm and 1.0 µm (see table 2.1), three of them located in the vicinity of the O_2 *A* band (MERIS channels 10, 11 and 12). Since there is only one channel within the absorption band and MERIS observations do not provide sufficient information about aerosols and the temperature profile, the achievable accuracy of a retrieval of surface pressure is limited. Therefore, this work does not aim at deriving surface pressure with sufficient accuracy to serve weather models, but demonstrating the performance of a state-of-the-art retrieval algorithm based on existing satellite data. Future satellite missions like EnMap (Stuffler et al. (2007)) or OCO (Crisp et al. (2004)) will provide spectrally higher resolved measurements in the oxygen *A* band and thus allow more accurate retrievals of surface pressure.

5.2 MERIS

MERIS is a programmable, medium-spectral resolution, imaging spectrometer (Rast et al. (1999)). It is one of ten core instruments on the polar orbiter ENVISAT (**Envi**ronmental **Sat**ellite, launched on March 1st, 2002) flying at 800 km in a sun-synchronous orbit with an equator crossing time of 10:30AM, descending node, and 98.5° inclination. MERIS consists of 5 identical pushbroom imaging spectrometers operating in the solar spectral range (390 to 1040 nm), arranged in a fan shape configuration which covers a total field of view of 68.5° and spans a swath width of around 1150 km. The spectral dispersion is achieved by mapping the entrance slit of a grating spectrometer onto a CCD array. The integration time, instrument optics and CCD array resolution are adjusted such that MERIS has a spatial resolution of 260 m * 300 m and a spectral sampling of 1.25 nm. The instrument electronic data rate provides 15 channels

which are programmable by ground command in width and in position. In the regular operation mode the spatial resolution is reduced by a factor of 4 along and across track (reduced resolution mode). In the full resolution mode, the full spatial resolution is transmitted. The central wavelengths of the spectral channels as listed in table 2.1 vary slightly across the field of view of MERIS. This "spectral smile" is caused by curvature of the image of the slit formed in the focal plane array, resulting in viewing angle-dependent central wavelengths of the spectral MERIS channels. In order to accurately determine the spectral smile of MERIS, spectral calibration campaigns are conducted repeatedly, using the full possible spectral resolution in the oxygen *A* band and solar Fraunhofer lines (Delwart et al. (2007)).

5.3 Algorithm description

The algorithm for the retrieval of surface pressure described herein is based on the exploitation of the absorption of solar radiation by oxygen at 0.76 µm. The strength of absorption can be related to the traversed absorber mass, since the transmission decreases as the traversed absorber mass increases. The so-called "differential absorption technique" is implemented in a wide field of remote sensing algorithms for the estimation of masses, e.g. the retrieval of atmospheric water vapour or trace gases. Since oxygen is well mixed in the atmosphere, the measured mass of oxygen is strongly related to average photon path length in the atmosphere. In case of clear sky measurements above bright land surfaces, the vast majority of photons detected by MERIS stems from reflection at the surface, enabling the retrieval of surface pressure.
The quantity carrying the information about the photon path length is the atmospheric transmission at 0.76 µm, which can not be measured directly but is approximated by the ratio r of an absorbing channel within the oxygen *A* band (MERIS band 11 at 761.875 nm) and an artificial non-absorbing measurement at the same spectral location:

$$r = L_{11}/L^{window}$$

The virtual non-absorbing measurement L^{window} is approximated by interpolating two window channels below and above the oxygen *A* band (MERIS bands 10 at 753.75 nm and 12 at 778 nm, see table 2.1), accounting for the spectral slope of the surface albedo.

The surface pressure retrieval algorithm is based on radiative transfer simulations using the **M**atrix **O**perator **Mo**del (MOMO, Fischer and Grassl (1984); Fell and Fischer (2001)). The simulations, covering all combinations of influencing parameters within the physically reasonable bounds, were used to derive coefficients of a multi-dimensional non-linear regression, relating the measured radiance to the surface pressure. The regression approach was chosen in order to obtain an algorithm which is able to operate in near real time without needing a high amount of calculation power and main memory. Artificial neural networks have proven to be suitable tools to perform the regression.

5.3.1 MOMO

Assuming a plane-parallel atmosphere, media of any optical thickness with any vertical inhomogeneity as well as any spectral resolution can be considered by MOMO, whereas three dimensional effects can not be simulated. An advanced k-distribution technique is used to incorporate gaseous absorption (Goody and Young (1989); Bennartz and Fischer (2000)). These calculations were based on the HITRAN 2004 data set (Rothman et al. (2005)), providing shape and strength parameters of the single absorption lines of the main atmospheric gases.

5.3.2 Artificial neural network

Artificial neural networks (ANN) are used in a wide field of remote sensing applications. If trained and applied properly, ANN algorithms are fast and accurate tools for the inversion of satellite measurements. The artificial neural network used for inverting MERIS radiances to surface pressure values is a multi layer perceptron (MLP) with three layers and 200 hidden neurons. Using MOMO simulations as training data bases, four ANN-versions were developed for different temperature regimes, namely tropical, mid-latitude summer, mid-latitude winter and subarctic summer profiles. These model atmospheres (McClatchey et al. (1972)) have been widely used in the atmospheric research community and provide standard vertical profiles of pressure, temperature, water vapor and ozone density. The input to the networks is composed of the window radiance L^{window}, the radiance ratio r, the central wavelength of MERIS band 11, the aerosol

optical thickness and the viewing geometry.

5.4 Sensitivity studies

In order to determine the sensitivity of MERIS measurements to the individual influencing quantities, radiative transfer calculations were performed, using again the radiative transfer model MOMO. The simulations were analyzed with respect to the influence of surface pressure and other geophysical parameters like aerosol optical thickness and scale height, surface albedo and the temperature profile. Additionally, the influences of instrumental parameters (spectral channel position and width) were determined.

5.4.1 The sensitivity to surface pressure, aerosol properties and instrumental parameters

Since the sensitivities to the examined parameters depend on the surface brightness and the aerosol loading, four different cases were studied:

- *a)* an optically thin aerosol layer above a dark land surface ($AOT = 0.1, \alpha = 0.2$),
- *b)* an optically thick aerosol layer above a dark land surface ($AOT = 0.8, \alpha = 0.2$),
- *c)* an optically thin aerosol layer above a bright land surface ($AOT = 0.1, \alpha = 0.6$),
- *d)* an optically thick aerosol layer above a bright land surface ($AOT = 0.8, \alpha = 0.6$).

The sensitivities were determined for a tropical atmosphere, a surface pressure of 1000 hPa and an aerosol scale height of 2 km, assuming an exponentially decreasing profile of extinction and a non-absorbing aerosol. For all four cases, the relative sensitivity of r to the examined parameters was determined with respect to an increase of surface pressure of 10 hPa (ξ_{SP}), an increase of AOT of 0.2 (ξ_{AOT}), an increase of aerosol scale height of 1 km (ξ_{ASH}), a shift of spectral channel position of 0.1 Å (ξ_{cp}) and an increase of channel width of 0.1 Å (ξ_{cw}). These values were chosen, because they cause a change of signal in the same order of magnitude.

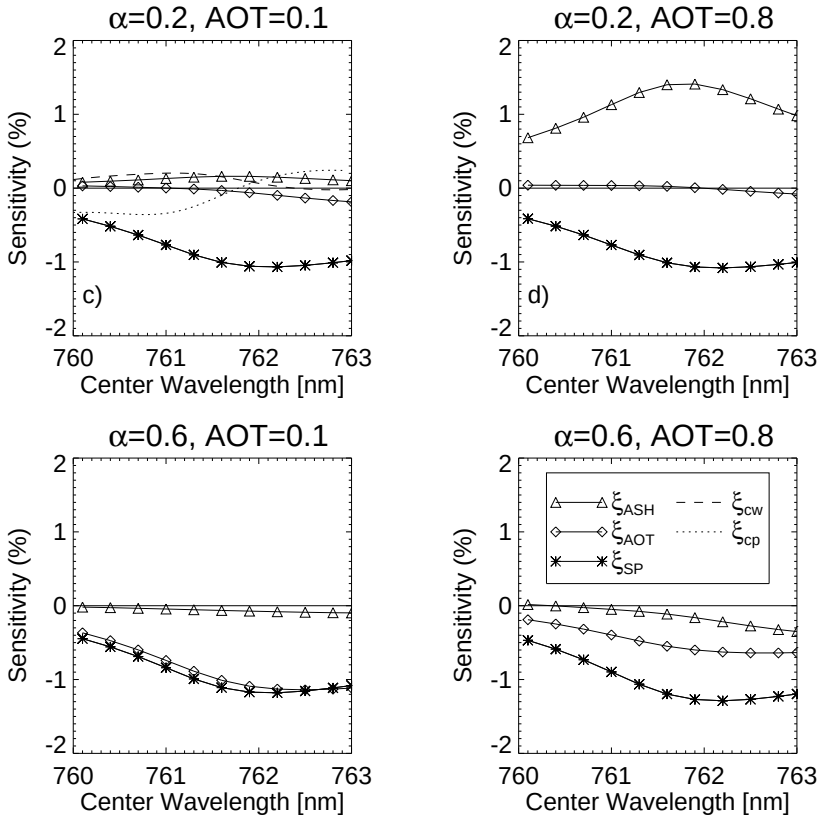

Figure 5.1: Sensitivity of channel ratio r to surface pressure ($\Delta SP = 10\,\text{hPa}$), aerosol optical thickness ($\Delta AOT = 0.2$), aerosol scale height ($\Delta ASH = 1\,\text{km}$), channel position ($\Delta cp = 0.1\,\text{Å}$) and channel width ($\Delta cw = 0.1\,\text{Å}$), depending on channel position of MERIS band 11. Sensitivities shown for nadir view and solar zenith of 36°.

Figure 5.1 shows the resulting sensitivities as percentage of r for all four cases. The sensitivity to surface pressure ξ_{SP} is shown by the stars, whereas the squares and crosses represent the spectral channel sensitivities ξ_{cw} and ξ_{cp}, respectively (shown exclusively for case *a)*, since there is no dependence on the cases). The triangles and diamonds correspond to the aerosol sensitivites ξ_{ASH} and ξ_{AOT}, respectively. Several conclusions can be drawn from figure 5.1:

- The sensitivity of r to a change of surface pressure has its maximum ($\sim -1\%/10\,\text{hPa}$) at about 762 nm, which is close to the nominal wavelength of MERIS band 11. There is only a weak dependence of ξ_{SP} on the aerosol loading

and the surface albedo.

- r is very sensitive to a change of channel position cp and channel width cw, regardless of the atmospheric state. Below 761 nm, a shift of 0.1 nm of cp towards longer wavelengths is equivalent to a change of surface pressure of about 50 hPa. An increase of cw here corresponds to a decrease of surface pressure of 20 - 40 hPa. Both ξ_{cp} and ξ_{cw} vanish in the region of 762 nm, due to the balancing effect of the weakly absorbing Q-branch of the oxygen absorption band. Towards longer wavelengths ξ_{cp} has a positive sign, whereas ξ_{cw} is close to zero. The strong sensitivities and their variability across the absorption band emphasize the need of an accurate spectral calibration. The nominal center wavelength of MERIS band 11 was initially set to 761.875 nm to avoid artefacts caused by inaccurate spectral calibration. However, the actual center wavelength varies roughly between 761 nm and 763 nm, due to the spectral smile effect.

- The sensitivity to aerosols strongly depends on the case under consideration. Above bright surfaces (cases *c)* and *d)*), both ξ_{AOT} and ξ_{ASH} are negative, indicating that an increase of aerosol optical thickness or scale height causes an increase of absorption. In case of ξ_{AOT}, this is caused by longer photon paths due to the "trapping" of photons between surface and the aerosol layer. The small negative effect of an increase of scale height (leaving the optical thickness unchanged) is caused by the increased distance covered by the photons between the scattering events. Above dark surfaces (cases *a)* and *b)*), an increase of scale height by 1 km has a strong effect for a high optical thickness (case *b)*), due to to the shielding of absorption in the lower atmosphere. At 762 nm, it corresponds to a decrease of surface pressure by 15 hPa. The effect is on the order of -2 hPa for a low optical thickness (case *a)*).

The influence of the aerosol optical thickness seems to be hard to predict, since it changes both sign and magnitude for each case. This is due to a dependence of ξ_{AOT} on the surface albedo, as shown in figure 5.2. Above dark surfaces like ocean ($\alpha \lesssim 0.05$), an increase of AOT at a scale height of 2 or 4 km causes longer photon paths and a decrease of r, since the scattering at aerosols occurs below the Rayleigh scattering ($h_{Raileigh} \approx 8$ km). For a moderate surface albedo ($\alpha \lesssim 0.3$) an increase of AOT causes

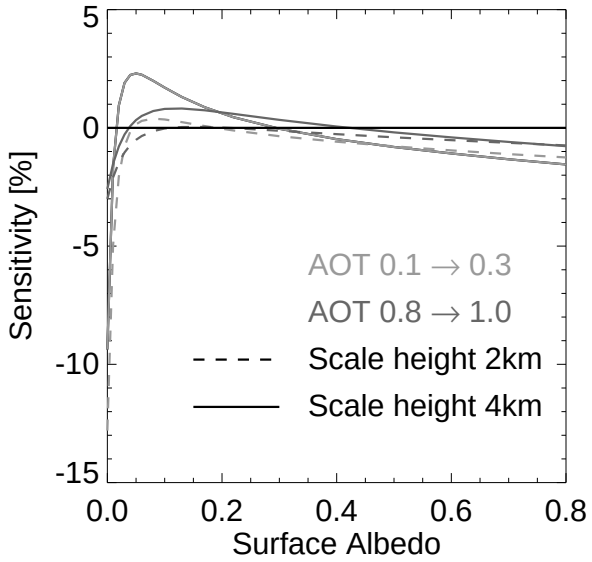

Figure 5.2: Sensitivity of channel ratio r to change of aerosol optical thickness ($\Delta AOT = 0.2$) for optically thin (light grey lines) and optically thick case (dark grey lines) and 2 km (dashed lines) and 4 km scale height (solid lines), depending on surface albedo. Sensitivity shown for nadir view and solar zenith of 36°.

shorter photon paths, because of the shielding of absorption by the aerosols. For bright surfaces ($\alpha \gtrsim 0.3$), the mentioned mechanism of trapping of photons between surface and aerosols dominates, resulting in path extensions and a decrease of r. There are additional dependencies on the solar zenith angle and the aerosol scale height and optical thickness. Regarding the surface pressure retrieval, the uncertainty introduced by assuming average values for the aerosol optical thickness does not exceed 10 hPa for a surface albedo $\alpha \geq 0.2$.

5.4.2 The sensitivity to the temperature profile

The oxygen *A* band is composed of several hundred individual absorption lines, that are subject to pressure- and temperature-dependent broadening processes in the atmosphere. In the lower atmosphere, the dominant process is pressure broadening. The resulting line can approximately be described by the Lorentz line shape:

$$f(\nu - \nu_0) = \alpha_L/\pi/((\nu - \nu_0)^2 + \alpha_L^2)$$

where α_L is the Lorentz half-width at half maximum, which is roughly proportional to the number of collisions per unit time (Petty (2006)):

$$\alpha_L \propto pT^{-1/2}$$

Obviously, an increase of temperature at constant pressure results in narrower, more intense absorption lines, whereas a decrease of temperature causes broader lines with weaker centers. It is therefore important to examine the effect of different temperature profiles on the measured broadband transmission within the oxygen *A* band. A simulation study was conducted using seven different standard temperature profiles as defined by McClatchey et al. (1972), namely a tropical, a mid-latitude summer and winter, a subarctic summer and winter and a US standard atmosphere (see Figure 5.3, left panel). In addition, a calculation using a US standard temperature increased by 1 K at all height levels was performed. The middle and right panels of figure 5.3 show the resulting deviations of the channel ratio *r* and the corresponding change of surface pressure for five profiles, relative to the US Standard atmosphere. At a height niveau of 1000 hPa, a maximum deviation of 40 hPa can be found for a subarctic winter profile. However, since in the subarctic region MERIS can hardly measure during wintertime due to the absence of sunlight, it is more reasonable to confine the analysis to the remaining profiles. As the deviation rises with pressure level due to the increase of traversed air mass, maximun errors of 20 hPa can be found at sea level. In case the temperature profile is known within 1 K, the errors do not exceed 5 hPa, which is to be taken as an upper boundary as the deviation from the real profile will generally not be a constant offset at all height levels. In case the error in the temperature profile changes its sign at some height level, the resulting error in surface pressure cancels out at least in parts.

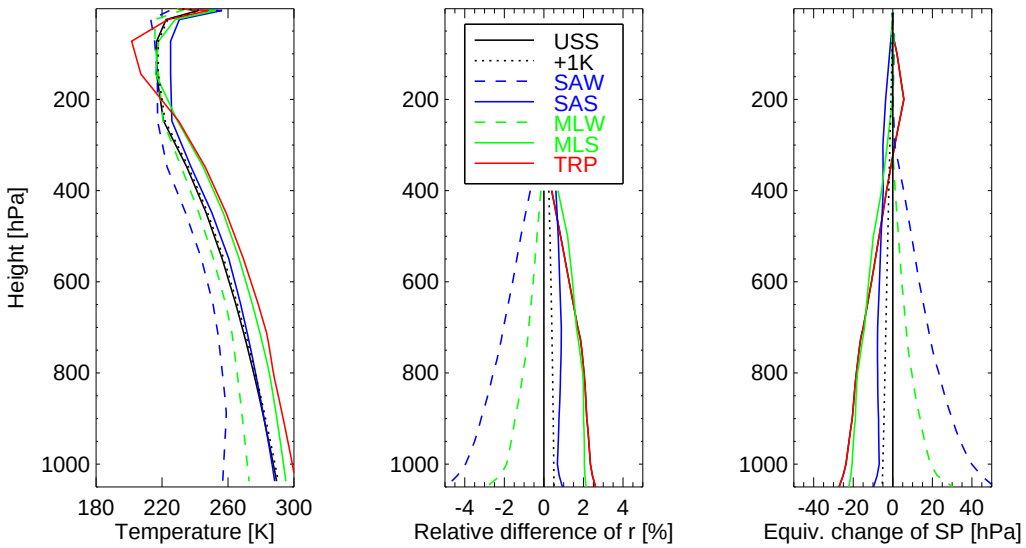

Figure 5.3: Left panel: Assumed standard temperature profiles (US Standard, US Standard+1 K, subarctic winter, subarctic summer, mid-latitude winter, mid-latitude summer, tropical profile). Middle panel: Relative difference of channel ratio r for used profiles, relative to US standard case, depending on height. Right panel: Equivalent change of surface pressure, relative to US standard case, depending on height. Sensitivities shown for nadir view and solar zenith of 40°, central wavelength $\lambda_{11} = 761.875$ nm.

5.4.3 Conclusion

Measurements within the oxygen A band show a high sensitivitiy to surface pressure. At a MERIS-like spectral resolution, the maximum sensitivity is found around 762 nm. In the vicinity of this spectral location the errors caused by the uncertainty of the exact channel position and width are small, the nominal center wavelength of MERIS channel 11 is therefore well defined. The uncertainty caused by the unknown aerosol loading and vertical profile is ≤ 10 hPa, except for cases of very high aerosol loading above dark surfaces. The temperature profile has to be known with high precision in order to prevent a large bias in retrieved surface pressure. A deviation of 1 K at all height levels results in errors ≤ 5 hPa. A further source of error is the unknown water vapour column amount, as the measurements are only sensitive to the dry air pressure. In the tropics, the partial pressure of water vapour can reach values of up to $8-10$ hPa. Assuming an appropriate average humidity, the resulting errors in surface pressure are ≤ 4 hPa in

extreme cases and lower otherwise. Both the uncertainty caused by the aerosol optical thickness and the water vapour amount can be limited by using the values retrieved from MERIS as implemented in the operational MERIS groud segment.

5.5 Algorithm performance

The trained artificial network (herein after referred to as SP_{FUB}) was used to derive surface pressure for several clear sky scenes above bright land. The derived values were then compared to surface pressure maps (herein after referred to as SP_{DEM}), constructed from a combination of ECMWF sea level pressure forecasts, as provided in MERIS Level 1 data, and the global digital elevation model (DEM) GTOPO30. GTOPO30 has a spatial resolution of 30 arc-seconds (roughly 1 km) and was built up by a combination of various data sets (U.S.GeologicalSurvey (1996)). The accuracy of GTOPO30 depends on the source data set, with a maximal accuracy of 18 m ($\approxeq$ 2 hPa) achieved in large parts of Asia, Europe, Africa and North America. These highly accurate regions of the DEM were chosen for building the surface pressure map, resulting in an excellent cross-check data set for the validation of the surface pressure retrieval.
Figure 5.4 shows the surface pressure as derived from ECMWF / GTOPO30 (upper left panel) and the SP_{FUB} algorithm (upper right panel) for a scene over North Africa on the 8th of August, 2005. The lower panels show the difference of both retrievals and an intersection plot along the line indicated in the upper panels. For the retrieval, a non-absorbing aerosol with an optical thickness of 0.15 and a tropical temperature profile were assumed. The scene is almost cloud free and shows a high correlation of both data sets (correlation coefficient $\rho = 0.95$). SP_{FUB} reproduces the orographic structures very well and is free of systematic errors ($bias = -1$ hPa, see figure 5.5). There is no bias, since the assumed tropical profile well matched the mean temperature profile of the scene. The overall root mean square deviation (*rmsd*) of 11 hPa is likely to be caused by unknown influencing parameters like the aerosol loading and the exact temperature profile for each location (see sections 5.4.1 and 5.4.2). The deviation of SP_{FUB} from SP_{DEM} in the mountainous region around 26°N, 8°E might in parts be caused by undetected clouds or sand storms, since obviously both data sets perfectly match in the northern mountain region (around 35°N, 7°E). Figure 5.5 shows a height-independent agreement between both data sets.

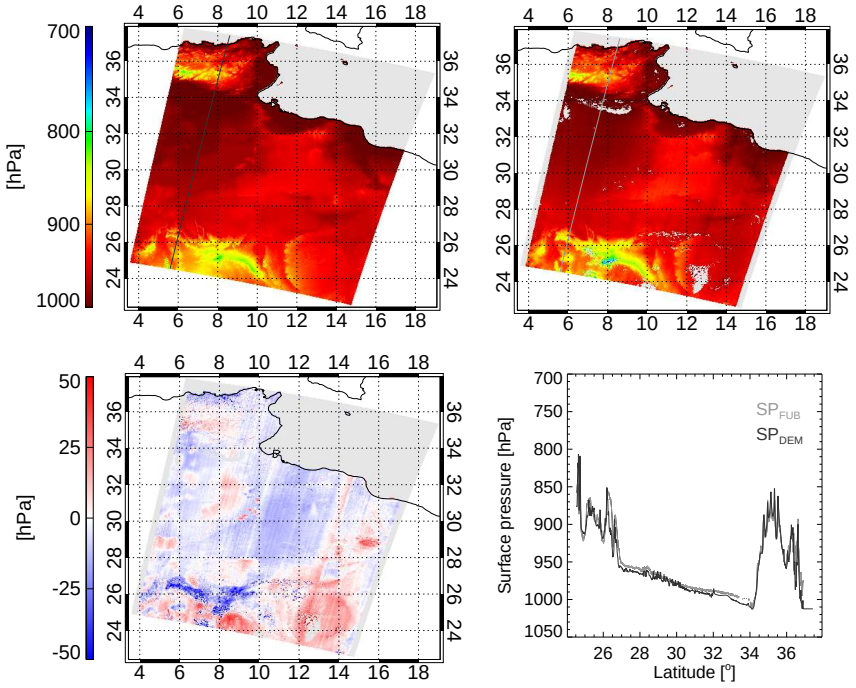

Figure 5.4: Surface pressure above Northern Africa on August 8th, 2005, as derived from DEM (GTOPO30) (upper left panel) and retrieved by SP_{FUB}(upper right panel). Bottom row: Difference SP_{FUB} - SP_{DEM} and intersection plot along lines indicated in upper panels.

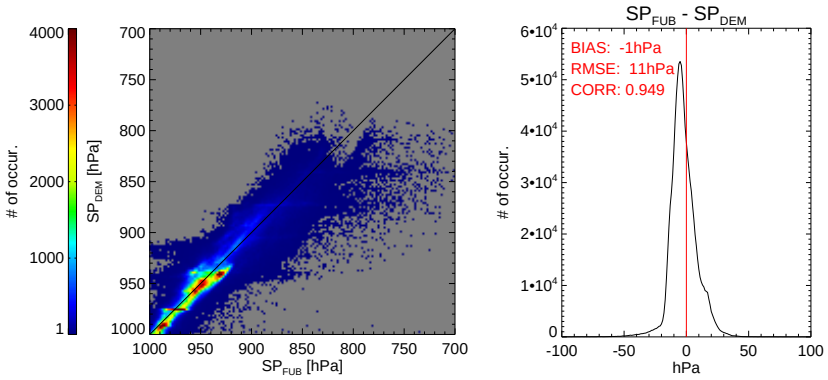

Figure 5.5: Scatterplot of surface pressure values of SP_{FUB} vs. SP_{DEM} (left panel) and frequency distribution of deviation of SP_{FUB} from SP_{DEM} (right panel) for scene above Northern Africa on August 8th, 2005.

Further scenes were analyzed in order to test the robustness of the retrieval to the measuring conditions and the surface properties. Figures 5.6 and 5.7 show the results for a scene above Southwest Asia on June 2nd, 2005. Since the version of SP_{FUB} applied here was only trained for surface pressure values between 1050 and 700 hPa, the retrieval could not be applied to higher elevated areas that are masked out, e.g. in the northeastern corner of the scene, above the western part of the Hindukush mountains. Across the scene, some scattered clouds could be spotted. These cloud fields are masked out for the most part, however the MERIS cloud mask fails for some pixels, especially at cloud edges. Again, a non-absorbing aerosol with an optical thickness of 0.15 and a tropical temperature profile were assumed for the retrieval. The comparison of both surface pressure maps again reveals a bias-free retrieval by SP_{FUB} at all height levels. The assumed temperature profile well matched the mean temperature profile of the scene, whereas the slightly higher root mean square deviation (14 hPa) indicates a higher variety of temperature profiles. However, it might as well be caused by undetected clouds or aerosol effects. The two data sets are again highly correlated ($\rho = 0.98$) and the intersection plot shows clearly that SP_{FUB} correctly reproduces the orographic structures.

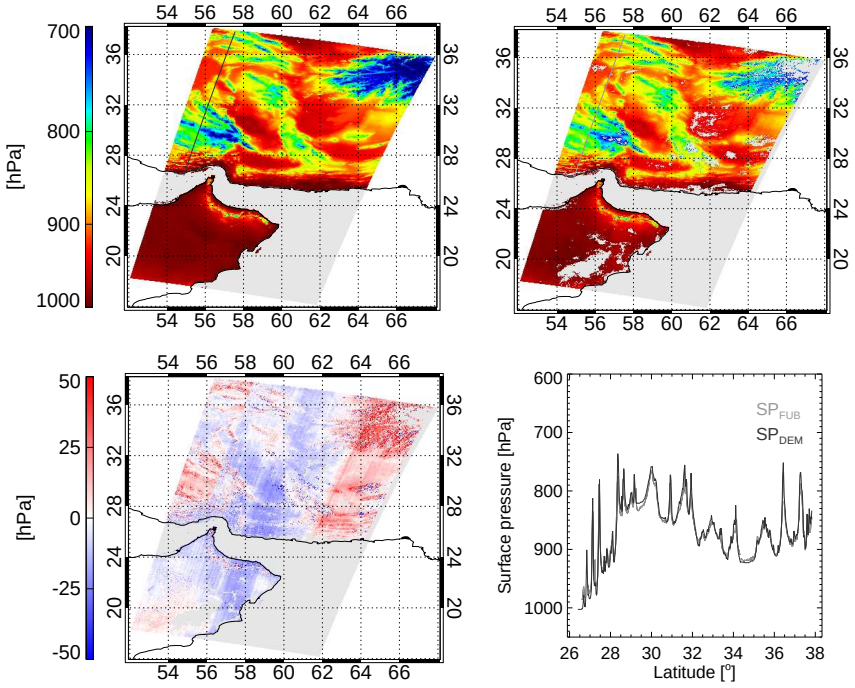

Figure 5.6: Surface pressure above Southwest Asia on June 2nd, 2005, as derived from DEM (GTOPO30) (upper left panel) and retrieved by SP_{FUB} (upper right panel). Bottom row: Difference SP_{FUB} - SP_{DEM} and intersection plot along lines indicated in upper panels.

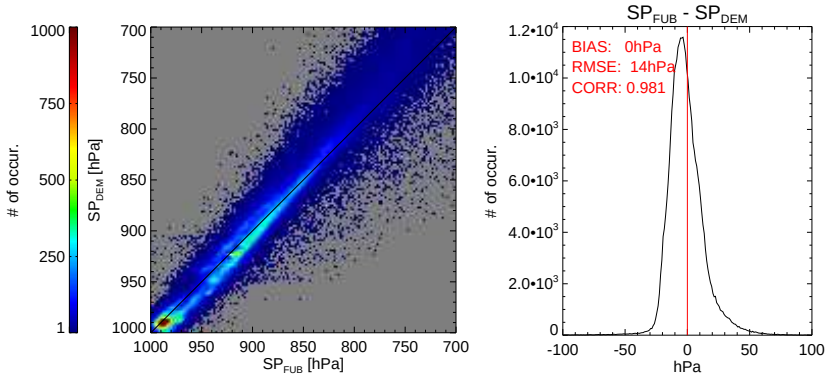

Figure 5.7: Scatterplot of surface pressure values of SP_{FUB} vs. SP_{DEM} (left panel) and frequency distribution of deviation of SP_{FUB} from SP_{DEM} (right panel) for scene above Southwest Asia on June 2nd, 2005.

Finally, a scene above Greenland was chosen for a comparison, in order to examine the behaviour of the surface pressure retrieval above ice. Since the GTOPO30 accuracy is not sufficient here, a digital elevation model of Greenland constructed from lidar measurements of GLAS on ICESAT was used (DiMarzio et al. (2007)). The highly accurate lidar data set can be regarded as almost free of errors for the purposes of this work. For the retrieval of surface pressure using SP_{FUB}, a subarctic summer profile with an aerosol optical thickness of 0.05 was assumed. The comparison, shown in figures 5.8 and 5.9, was made for the ice-covered, cloud-free part of Greenland on July 20th, 2005. The surface pressure field derived by SP_{FUB} shows discontinuities across the field of view that are caused by imprecise correction of stray light within the individual cameras of MERIS. Apart from that, the comparison reveales a high correlation coefficient ($\rho = 0.98$) and the smallest standard deviation ($rmsd = 8$ hPa) of all scenes investigated. The high reflectivity of the ice cover obviously enables the most accurate determination of surface pressure. Additionally, there is hardly any disturbing influence of aerosols in typically pristine arctic air. On the other hand, operational cloud screening above ice surfaces is difficult using MERIS measurements.

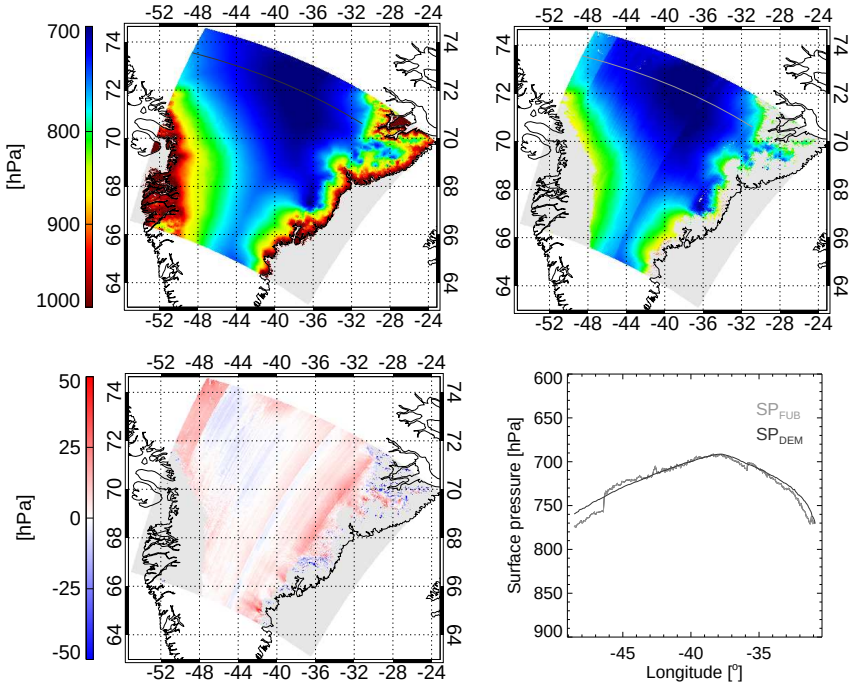

Figure 5.8: Surface pressure above ice-covered areas of Greenland on July 20th, 2005, as derived from DEM (IceSat) (upper left panel) and retrieved by SP_{FUB} (upper right panel). Bottom row: Difference SP_{FUB} - SP_{DEM} and intersection plot along lines indicated in upper panels.

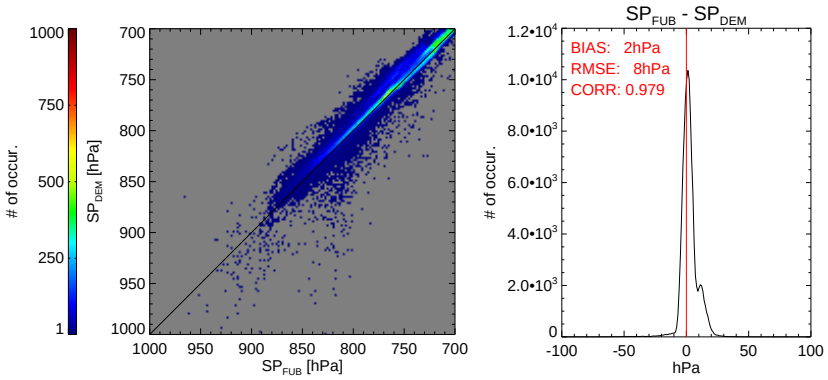

Figure 5.9: Scatterplot of surface pressure values of SP_{FUB} vs. SP_{DEM} (left panel) and frequency distribution of deviation of SP_{FUB} from SP_{DEM} (right panel) for scene above Greenland on July 20th, 2005.

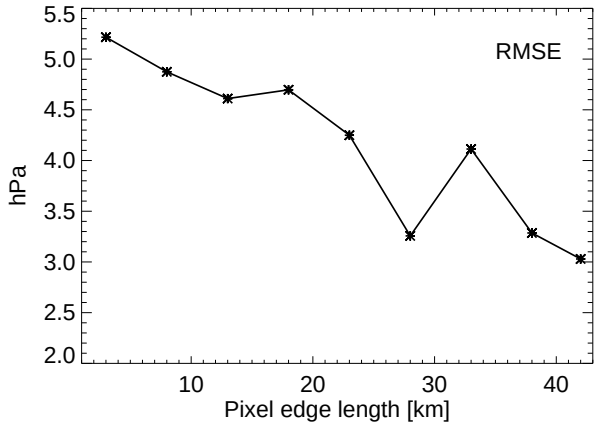

Figure 5.10: Effect of pixel averaging on retrieval accuracy of SP_{FUB} for inland area above Greenland on July 20th, 2005.

In order to examine the potential to further improve the performance of SP_{FUB}, the effect of pixel averaging on the retrieval accuracy was studied. Therefore a rectangular cloud-free area in the central part of Greenland was chosen (~210 km * 220 km). The edge length of the retrieval pixels was increased successively by spatially averaging MERIS pixels. Figure 5.10 shows the effect on the retrieval accuracy, depending on the pixel edge length. For the selected area, the standard deviation of both data sets drops from 5 to 3 hPa for an edge length of 40 km. As all geophysical error sources like the temperature profile and the aerosol properties do not vary considerably on these scales, the increase of accuracy is mainly due to the cancellation of instrument noise. Regarding a typical horizontal pressure gradient of 0.01 hPa/km (in cloud-free areas), a spatial averaging of pixels appears to be a helpful tool for increasing the pressure retrieval accuracy.

5.6 Conclusion

The newly developed algorithm for the retrieval of surface pressure SP_{FUB} shows good results above bright land surfaces. The derived surface pressure values are bias-free, as the comparison with surface pressure maps constructed from ECMWF / GTOPO30 data and ECMWF / GLAS data revealed. The remaining noise (8 hPa$\leq$ *rmsd* $\leq$ 14 hPa,

depending on scene under consideration) can be well explained with undetected clouds, the uncertainty introduced by the unknown aerosol loading and profile and the exact temperature profile, as shown in section 5.4. For a selected test case above Greenland the retrieval error of SP_{FUB} could be reduced to $rmsd < 3$ hPa by spatial averaging of 40 * 40 pixels of MERIS.

The retrieval algorithm can be adapted to sun glint cases over ocean. A higher accuracy might be possible here because of the absence of topography and the resulting smaller values margin. However, the lack of information about aerosols will hamper the retrieval here as well. Above the dark ocean, where information about aerosols is available, the signal from the reflection at the water surface is too weak for a retrieval of surface pressure.

The accuracy of surface pressure above land as found in this study is not sufficient to serve weather models. Instead, this work demonstrates a state-of-the-art retrieval of surface pressure using the oxygen *A* band, based on existing measurements of MERIS. The synergetic use of various sources of information about photon path length, aerosol distribution and the temperature profile could significantly enhance the accuracy of the retrieval. Spectrally highly resolved measurements in the oxygen *A* band, as the **O**rbiting **C**arbon **O**bservatory (OCO, Crisp et al. (2004)) will prospectively provide from mid 2009, have the potential to retrieve surface pressure with a theoretical accuracy of 2 hPa (Mitchell and O'Brien (1987)).

Acknowledgments

This work was funded by DFG (reference nr. FI 435/15-1) and ESA (contract nr. 20693 / 07 / I-OL).

6 Empirical correction of stray light within the MERIS oxygen *A* band channel

---

Lindstrot, R., R. Preusker, and J. Fischer, (2009), submitted to Journal of Atmospheric and Oceanic Technology

Abstract

Spaceborne spectrometers like MERIS (**Me**dium **R**esolution **I**maging **S**pectrometer) onboard ENVISAT (**Envi**ronmental **Sat**ellite) are widely used for the remote sensing of atmospheric and oceanic properties and make an important contribution to the monitoring of the earth atmosphere system. In order to enable retrievals with high accuracy the spectral and radiometric properties of the instruments have to be characterized with high precision. One of the main sources of radiometric errors is stray light caused by multiple reflection and scattering at the optical elements within the instruments. If not corrected for properly the stray light-induced offsets of measured intensity can lead to significant errors in the derived parameters. The effect of stray light is particularly momentous in case of measurements inside strong aborption bands like the oxygen *A* band at 0.76 µm or the $\rho\sigma\tau$-absorption band of water vapour around 0.9 µm. For example, the retrieval of surface and cloud-top pressure from MERIS measurements in the O_2 *A* band can be biased due to an insufficient correction of stray light in the operational processing chain.

In order to correct for the residual stray light influence after the operational stray light correction in the O_2 *A* band channel of MERIS, an empirical stray light correction of the measured radiance at 0.76 µm has been developed based on optimizing the coefficients of a simple brightness-dependent stray light model. The optimal model coefficients were found by adjusting the retrievals of surface and cloud-top pressure to accurate reference data for several selected scenes. In order to account for the limited accuracy of the MERIS spectral calibration, the center wavelength of the O_2 *A* band channel was additionally adjusted within a ± 0.1 nm tolerance range. The correction was tested on a variety of clear and cloudy scenes at different locations by applying the surface and cloud-top pressure retrieval algorithms to data recorded over the whole lifetime of MERIS. The results indicate the potential to greatly improve the accuracy of the retrieved pressure values using the proposed correction factors.

6.1 Introduction

Satellite observations provide an indispensable contribution to the monitoring of atmosphere, earth and ocean. Since it is impossible to operationally perform in-situ measurements of cloud properties, the spaceborne remote sensing of clouds is of special importance. The methodologies for the retrieval of cloud properties from satellite data have been constantly advanced during the past decades. In case of the retrieval of cloud altitude, representing one of the most decisive parameters for the cloud radiative effect, several techniques have been developed. The most popular methodologies make use of either the thermal emission of the clouds, allowing for the determination of the cloud's temperature and height (e.g. Smith and Platt (1978); Wielicki and Coakley (1981); Menzel et al. (1982, 2006)) or stereoscopic views, exploiting the height-dependent parallax of clouds when looked at from different angles (e.g. Seiz et al. (2006)). Another possibility for the detection of cloud height is the exploitation of measurements within the oxygen *A* absorption band at 0.76 µm (Yamamoto and Wark (1961); Wu (1985); Fischer and Grassl (1991); Preusker and Lindstrot (2009)): The mass of oxygen along the path of reflected sunlight is derived from measurements inside the absorption band. Since oxygen is well mixed in the atmosphere, the traversed mass of air can directly be determined, allowing for the retrieval of cloud-top pressure. Since the launch of ENVISAT (**Envi**ronmental **Sat**ellite) on March 1st, 2002, measurements inside the O_2 *A* band are available from MERIS (**Me**dium **R**esolution **I**maging **S**pectrometer, Rast et al. (1999)). MERIS, primarily designed for the remote sensing of coastal waters, is operationally used for the retrieval of cloud properties like optical thickness and height. The oxygen *A* band method allows for accurate retrievals of cloud-top pressure, especially in case of low clouds, where the common techniques exploiting the thermal emission of clouds are less sensitive. In a validation campaign using airborne lidar measurements of cloud-top height, Lindstrot et al. (2006) found an accuracy of 25 hPa for low, single-layered clouds. In case of clear sky, the MERIS measurements inside the oxygen *A* band can be used for a retrieval of surface pressure which can be an important tool for cloud detection in satellite imagery. Currently, the measurements of MERIS allow a surface pressure retrieval accuracy of approximately 10-15 hPa (Lindstrot et al. (2009)). Apart from the uncertainty introduced by the influence of geophysical parameters like e.g. the temperature profile, the upper limit for the achievable retrieval accuracy is fixed by in-

strumental constraints like sensor noise. In case of MERIS measurements in the O_2 *A* band, one of the largest sources of error is instrumental stray light.

Instrumental stray light is caused by multiple scattering and reflection at optical elements within the spectrometer like lenses or gratings. The correction of stray light is particularly important in absorption bands since weak intensities are affected strongly even by small offsets caused by stray radiation. Therefore, the O_2 *A* band based algorithms for the retrieval of surface and cloud-top pressure from MERIS are susceptible to errors caused by instrumental stray light. Although there is a correction for stray radiation in the operational MERIS processing chain (MERIS ground segment, Merheim-Kealy et al. (1999)), artifacts are apparent in the pressure retrievals in particular, that are likely to be caused by residual stray light. The quantification of the stray light effect on the retrieval errors is complicated by a high correlation with the effect of the spectral calibration uncertainty: A spectral shift of the oxygen *A* band channel towards weaker or stronger absorption causes a similar signal as an under- or overestimation of the stray light contribution to the measured radiance. Since the MERIS swath is composed of the measurements of 5 identical cameras with individual characteristics (see section 6.2.1), the errors induced by stray light and spectral calibration issues become evident particularly at the borders of the field-of-view of the cameras, resulting in discontinuities of the derived pressure. In the past, these errors as a whole were attributed to the spectral calibration inaccuracy, assuming that the operational stray light correction scheme worked to a satisfying degree. Therefore, an individual spectral calibration was performed for the MERIS oxygen *A* band channel, deviating from the operational spectral calibration by up to 0.2 nm. In view of the contradicting results of the two calibration efforts, hinting at the presence of residual stray light in the oxygen *A* band, and the fact that the errors in the derived pressure products could not be eliminated following this approach, the authors pursued a different strategy. Using the operational spectral calibration, the coefficients of a simple stray light model were optimized along with adjusting the retrieved pressure values to reference maps. This procedure was applied to operational level 1 data, already subject to the operational stray light correction in advance, as well as to MERIS spectral campaign data. MERIS spectral campaigns are a series of consecutive orbits dedicated to the spectral calibration of MERIS, conducted repeatedly during the the lifetime of the mission and characterized by a modified spectral band setting, providing the maximal possible spectral resolution inside the oxygen *A*

band. Due to the modified spectral band setting, the operational stray light correction is not applied to this data. In case of the operationally corrected data, the results obtained with our method will not represent a realistic estimate of the stray light contribution to the oxygen *A* band channel, but provide a possibility to correct the operational O_2 *A* band radiance in order to eliminate the artifacts in derived pressure products. In case of the spectral campaign data, the retrieved stray light correction coefficients indicate the actual amount of stray light in the oxygen *A* band, averaging out at roughly 5% of the radiance available in the absorption-free vicinity of the absorption band (see 6.4).
The instrument MERIS and the stray light model used in the frame of this work are introduced in section 6.2. Section 6.3 describes the correction strategies used for the surface and cloud-top pressure retrievals. The results of the stray light optimization and applications to independent MERIS data are shown in sections 6.4 and 6.5.

6.2 MERIS

6.2.1 Instrument overview

MERIS is a programmable, medium-spectral resolution, imaging spectrometer (Rast et al. (1999)). It is one of ten core instruments on the polar orbiter ENVISAT (**Envi**ronmental **Sat**ellite, launched on March 1st, 2002), flying at 800 km in a sun-synchronous orbit with an equator crossing time of 10:30AM, descending node, and 98.5° inclination. MERIS consists of 5 identical pushbroom imaging spectrometers operating in the solar spectral range (390 to 1040 nm), arranged in a fan shape configuration which covers a total field of view of 68.5° and spans a swath width of around 1150 km. The fields-of-view of the five spectrometers therefore cover each a different area on ground while all cameras are observing the same spectral range. The spectral dispersion is achieved by mapping the entrance slit of a grating spectrometer onto a CCD array. The integration time, instrument optics and CCD array resolution are adjusted such that MERIS has a spatial resolution of 260 m x 300 m, a maximum spectral resolution of 1.6 nm and a spectral sampling of 1.25 nm. The instrument electronic data rate provides 15 channels which are programmable by ground command in spectral width and position with each channel obtained by integrating over several detector rows in spectral direction of the CCD array. In the regular operation mode the spatial resolu-

tion is reduced by a factor of 4 along and across track (reduced resolution mode). In the full resolution mode, the full spatial resolution is transmitted. The central wavelengths of the spectral channels as listed in table 2.1 vary slightly across the field of view of MERIS. This "spectral smile" is caused by curvature of the image of the slit formed in the focal plane array, resulting in viewing angle-dependent central wavelengths of the spectral MERIS channels. In order to accurately determine the spectral smile of MERIS, spectral calibration campaigns are conducted repeatedly, using the full possible spectral resolution in the oxygen *A* band and solar Fraunhofer lines (Delwart et al. (2007)).

6.2.2 Stray light and spectral calibration

Stray light can e.g. refer to light of other frequency than intended or light following paths other than intended. It is typically caused by multiple reflection and scattering at optical elements like lenses or gratings. As a result, both the spectral as well as the spatial purity are degraded, e.g. causing a virtual monochromatic point source to be imaged slightly blurred both spectrally and spatially. According to the MERIS pre-flight characterization, stray light within the instrument is composed of two differing contributions: a diffuse part, caused by internal light scatter and grating ghosts. Within MEGS (MERIS ground segment, Merheim-Kealy et al. (1999)), the measured radiances are corrected for instrumental stray light. However, for computing performance reasons, the current operational stray light correction uses a rather coarse spectral sampling. As the diffuse part of the stray light is spectrally smooth, it is correctly accounted for by the operational stray light correction where the input spectra are smooth as well. This requirement is fulfilled for all MERIS bands except for channel 11 within the oxygen A band. The less pronounced ghost contributions are poorly corrected for the same reason (L. Bourg, ACRI-ST, 2009, personal communication).
As large discontinuities in the derived products can be found especially at the borders of the field-of-view of the MERIS cameras, the correction scheme is suspected to be insufficient. In order to improve the performance of the MERIS pressure retrievals, a secondary empirical stray light correction was developed in the frame of this work. A similar correction scheme has been developed for the MERIS spectral calibration orbits, characterized by a modified band setting with a maximal spectral resolution within the O_2 *A* band (Delwart et al. (2007), see figure 6.1). These measurements are not subject to

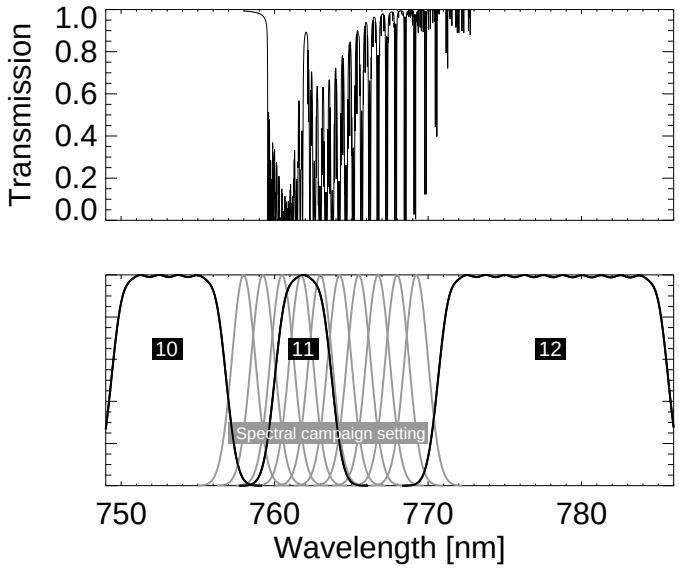

Figure 6.1: Atmospheric transmission around 0.76 µm (airmass=1, upper panel) and MERIS spectral channel response functions for nominal and spectral campaign band setting (lower panel).

the operational stray light correction and therefore enable a determination of the amount of stray light using the empirical correction approach.

The stray light effect is stronger in case the target is bright, since the more photons are available the more stray light is to be expected. The modelled instrumental stray light was therefore related to the brightness of the observed scene. In order to account for in-camera slopes of the stray light and effects of higher order at the camera boundaries, an additional dependency on the across-track pixel number of MERIS had to be taken into account. Stray light within and close-by the O_2 *A* band was therefore assumed to depend linearly on the brightness in window channel 10 at 754 nm with a polynomial dependence on the normalized across-track pixel index x, with $-1 \leq x \leq 1$:

$$f = a + bx + cx^4$$

where f is a factor relating the amount of radiance of band 10 to the corrective offset to be subtracted from the O_2 A band channel:

$$L^*_{O_2A} = L_{O_2A} - f * L_{10}$$

Since the error caused by instrumental stray light is a radiance offset, it is hard to separate from the spectral uncertainty of MERIS band 11, which causes the channel to be slightly shifted towards weaker or stronger gaseous absorption as compared to the nominal position. The MERIS spectral calibration is operationally performed by analyzing the position of well-known solar Fraunhofer lines in the measured spectrum of MERIS. As an exception the O_2 A band channel was spectrally calibrated by analyzing the shape of the oxygen A band, exploiting the full possible spectral resolution of 1.25 nm between 758 and 770 nm available during the spectral calibration orbits (Delwart et al. (2007)). The difference between the two calibration approaches is in the region of 0.2 nm and is suspected to be caused by either residual stray light in the oxygen A band or the temperature dependence of the absorption lines. Consequently, in the frame of this study the center wavelength of MERIS band 11 was set to the values found by the Fraunhofer calibration and adjusted within a range of ± 0.1 nm, represented by the fourth parameter d to be optimized:

$$\lambda^*_{11} = \lambda^{Fraunhofer}_{11} + d$$

The coefficients a, b, c and d were found by minimizing the retrieval errors of surface and cloud-top pressure, as detailed in section 6.3. Therefore, the bias of the pressure retrievals was analyzed at regularly spaced gridpoints of the parameter space spanned by the coefficients a, b, c and d. The optimal set of coefficients was found by iteratively narrowing the values margin for each coefficient, centered around the state resulting in the smallest pressure bias in the previous iteration step. This procedure was performed separately for each MERIS camera in order to account for the deviating behaviour of the individual modules. The pressure adjustment was conducted simultaneously for a numer of selected clear sky and cloudy scenes in order to assure the global validity of the found correction coefficients.

6.3 Correction strategy

6.3.1 Surface pressure

The algorithm for the retrieval of land surface pressure from MERIS measurements (hereafter SP_{FUB}) is based on the exploitation of the gaseous absorption by oxygen around 762 nm. As oxygen is well mixed both horizontally and vertically in the atmosphere, the observed amount of oxygen along the light path is directly related to the traversed air mass, allowing for the determination of the surface pressure. The amount of oxygen is derived from the transmission in the oxygen *A* band, approximated by the radiance ratio of the absorption channel 11 and a virtual absorption-free channel at the same spectral location, interpolated from channels 10 and 12 (see figure 6.1). The inversion of the TOA radiance measurements is performed by an Artificial Neural Network (ANN) trained with radiative transfer simulations. The Matrix Operator Model (MOMO, Fell and Fischer (2001)) was used to build the data base for the training of the ANN. An advanced k-distribution technique was used for the calculation of the oxygen absorption (Bennartz and Fischer (2000)), assuming a fixed temperature profile. A detailed description of SP_{FUB} can be found in Lindstrot et al. (2009) (chapter 5). In order to use SP_{FUB} for the optimization of surface pressure in the spectral campaign orbits, the ANN had to be adapted to the spectral campaign band setting, using 3 narrow channels inside the oxygen *A* band instead of the nominal channel 11 (see figure 6.1).
The surface pressure retrieval algorithm is well suited for the optimization of the O_2 *A* stray light model, since

1. the main piece of information is provided by the O_2 *A* channel to be corrected,
2. accurate reference data is available from terrain-corrected sea level pressure.

The ECMWF sea level pressure is available from MERIS level 1 data files while the surface elevation could be extracted from digital elevation models (DEM). The DEM derived from measurements of the **G**eoscience **L**aser **A**ltimeter **S**ystem (GLAS) onboard the A-train satellite IceSat (DiMarzio et al. (2007)) was used to calculate the surface pressure above Greenland, the SRTM (**S**huttle **R**adar **T**opography **M**ission, Farr et al. (2007)) DEM was used elsewhere. Both data sets are spatially highly resolving (spatial resolution: 1 km (GLAS / Greenland), 90 m (SRTM)), accurate height models that can

be regarded as nearly free of errors for the purpose of this work. In order to obtain the DEM-corrected pressure SP_{DEM}, the ECMWF sea level pressure P_{ECMWF} was converted using the terrain height h and the surface temperature t:

$$SP_{DEM} = P_{ECMWF}/exp(gh/(R(t + Ce + \gamma h/2)))$$

with $g = 9.80665\,\mathrm{ms}^{-2}$ representing the gravitation constant, $R = 287.05\,\mathrm{Jkg}^{-1}\mathrm{K}^{-1}$ the specific gas constant of dry air, $C = 0.11\,\mathrm{KhPa}^{-1}$ a constant accounting for the influence of the humidity, e the vapor pressure at the surface, and $\gamma = 0.0065\,\mathrm{Km}^{-1}$ the temperature lapse rate in the atmosphere. This formula, accounting for the temperature at the surface, was chosen instead of assuming an average atmosphere in order to be consistent with the standard procedures of reducing in-situ measured surface pressure to sea level.

6.3.2 Cloud-top pressure

Similar to the retrieval of surface pressure, the cloud-top pressure (hereafter CTP) can be derived from MERIS measurements in the oxygen A band (Preusker and Lindstrot (2009), see chapter 2). Here the inversion of the measured radiance ratio is further complicated by the unknown influence of multiple scattering inside the cloud layer and between the surface and the cloud. In order to account for these effects, the surface albedo is extracted from a global albedo data base (MERIS AlbedoMap, Muller et al. (2007b)), whereas the in-cloud scattering is estimated from the cloud optical thickness, reasonably well derivable from measurements of the window channel 10 at 754 nm (Fischer and Grassl (1991)). The algorithm for the retrieval of cloud-top pressure (hereafter $\mathrm{CTP}_{\mathrm{FUB}}$) is an ANN, trained with MOMO radiative transfer simulations (Fischer et al. (1997)). $\mathrm{CTP}_{\mathrm{FUB}}$ was not adapted to the spectral campaign band setting and only used for the optimization of stray light in the nominal band setting.
Since the true height of the clouds observed by MERIS is not known with sufficient accuracy, the adjustment of $\mathrm{CTP}_{\mathrm{FUB}}$ was limited to eliminating the discontinuities in CTP at the borders of the field-of-view of the MERIS cameras. MERIS scenes providing extended homogeneous stratocumulus fields in the Southern Atlantic Ocean were selected for the optimization. In order to account for small across-track trends in cloud height, simultaneous observations of SEVIRI (**S**pinning **E**nhanced **V**isible and **I**nfra**r**ed **I**mager, Aminou (2002)) onboard MSG (**M**eteosat **S**econd **G**eneration) were analyzed:

The cloud-top temperature as observed by SEVIRI at 10.8 µm was converted to cloud-top pressure using ECMWF temperature profiles. This simple method for the retrieval of CTP is susceptible to the temperature profile inaccuracy and the unknown amount of water vapour above the low stratocumulus deck and therefore is likely to result in a biased CTP retrieval. However, the derived cloud heights are free of any MERIS-like camera effects and therefore served as a relative reference: The SEVIRI-derived CTP was shifted to make both cloud height retrievals match on average. Then the MERIS camera effects were eliminated by fitting CTP_{FUB} to the shifted SEVIRI-derived CTP by optimizing the stray light coefficients, as detailed in section 6.2.2.

6.3.3 Scene selection

6.3.3.1 Nominal band setting

Various MERIS scenes above desert (from orbits 18598, 18755, 18897 and 18926) and Greenland (from orbits 17714, 17728, 17729) were selected for the surface pressure adjustment. The scenes were thoroughly checked for being free of clouds, using the MERIS cloud mask and visual inspection, and matching the temperature profiles used for the training of the SP_{FUB} artificial neural networks on average. A tropical and a subarctic summer temperature profile were assumed for the desert and greenland scenes, following the defintion by McClatchey et al. (1972). However, the heterogeneity of the temperature profile over the selected scenes causes a small, variable bias in surface pressure, reducing the accuracy of the optimized correction factors. In addition to the clear sky observations, several homogeneous cloud scenes above the Benguela current region (from orbits 16394, 18899, 18956) were chosen for the optimization of the CTP retrieval. The resulting scene composite, entirely recorded between April and October 2005 and shown in figure 6.2 (left panel), covers the whole swath of MERIS to assure that all cameras are represented in the optimization data set.

6.3.3.2 Spectral campaign band setting

The stray light optimization was performed on clear sky scenes only, using the SP_{FUB} algorithm adapted to the spectral campaign band setting. The optimization data set was composed of three desert scenes above the Arabian Peninsula, the Libyan desert and the

Western Sahara, recorded during a spectral campaign on December 13th, 2008 (MERIS orbits 35488 - 35490). The scenes are shown in figure 6.2 (right panel).

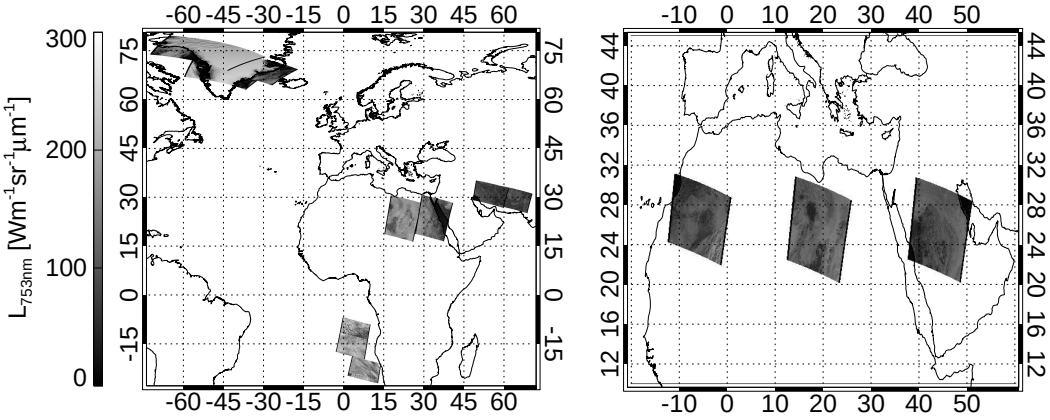

Figure 6.2: MERIS scenes used for the optimization of the stray light model for the nominal band setting (left panel) and the spectral campaign band setting (right panel).

6.4 Results

6.4.1 Nominal band setting

The effect of the optimization on the retrieved pressure is shown separately for scenes over desert, ice and clouds in figure 6.3. The displayed curves are median values of the along-track columns depending on the across-track pixel number, in order to demonstrate the camera effects visible in the across-track direction. For all regimes, the retrieval based on the Fraunhofer spectral calibration and unmodified level 1 radiances exhibits strong discontinuities at the borders and artificial slopes inside the field-of-view of the individual cameras. The deviation from the reference pressure exceeds 100 hPa at some locations. In contrast, the retrieval based on stray light corrected radiances is close to the reference data for all regimes and shows hardly any camera artefacts. Apparently, the assumed simple stray light model is suitable for the removal of the strong camera effects and the correction quality does not depend on the regime under consideration. The

correction is therefore applicable over clear sky and cloudy scenes at different brightness levels.

The resulting factor f for the correction of MERIS band 11 radiance and the deviation from the operational Fraunhofer calibration as found by the optimization algorithm are shown in figure 6.4. As detailed in section 6.2.2, the nominal band setting data is operationally corrected for stray light in the MERIS ground segment, so f does not represent the actual amount of stray light present within MERIS band 11 but rather is a correction factor, compensating for a too strong or too weak correction within the MERIS ground segment. Following the optimization results, the operational correction scheme under-

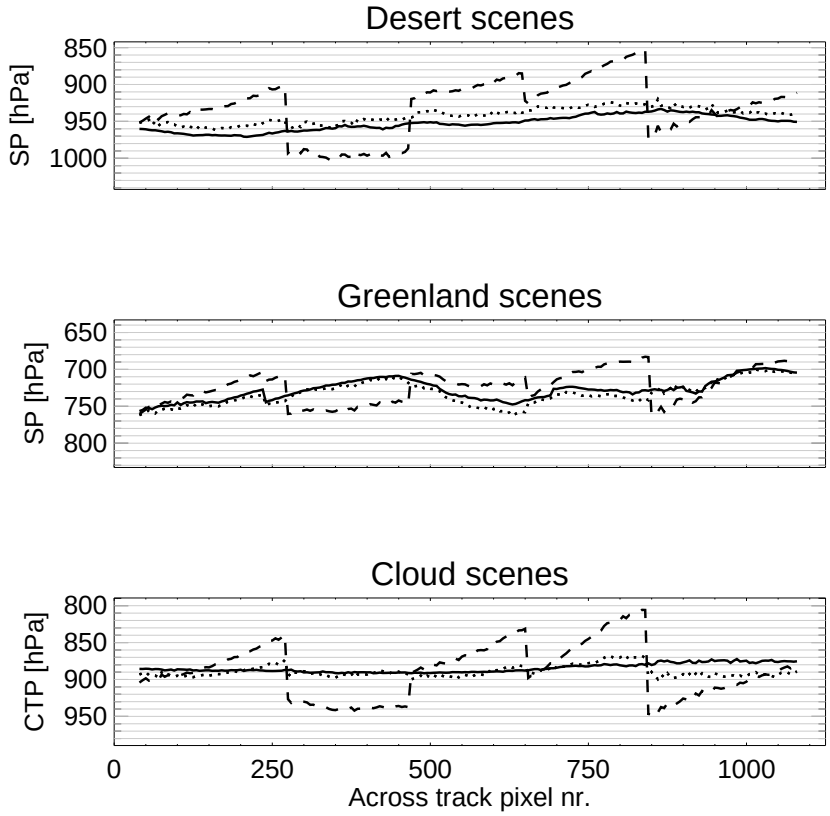

Figure 6.3: Upper and middle panel: Along-track median values of surface pressure above desert and Greenland derived from DEM (solid line), and MERIS measurements before (dashed) and after (dotted) optimization. Bottom panel: Same for cloud-top pressure, solid line represents MSG-derived CTP, shifted to match average MERIS-derived CTP.

estimates the amount of stray light for cameras 1-3 and 5, whereas it is overestimated for camera 4. In addition, the Fraunhofer calibration is modified by the optimization approach, exhibiting a positive wavelength shift for cameras 1, 2 and 5 and a negative shift for cameras 3 and 4. There is a high correlation of the correction factor f and the center wavelength of band 11, presumably caused by the disability of the operational correction scheme to seperate the effects of spectral shifts and stray light.

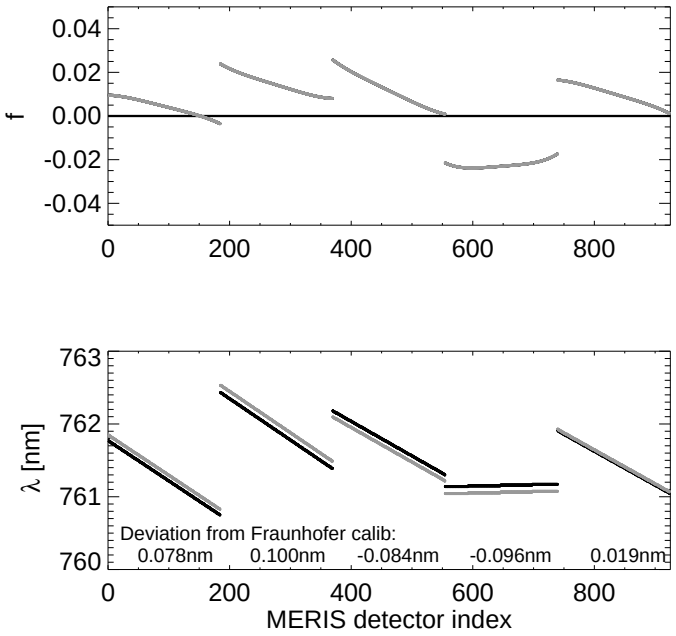

Figure 6.4: Optimization results for nominal band setting: Additive stray light factor f (upper panel) and central wavelength of MERIS channel 11 as resulting from optimization (grey) and Fraunhofer calibration (black), depending on MERIS detector index.

6.4.2 Spectral campaign band setting

As mentioned in section 6.2.2, the spectral campaign data is not operationally corrected for stray light. The correction factor f, found by the pressure adjustment algorithm, therefore does not merely represent a correction factor but corresponds to the actual amount of stray light present within the oxygen A band channels. Similar to figure 6.3 for the nominal band setting case, figure 6.5 shows the effect of the stray light

optimization on the retrieved surface pressure. Here the retrieval based on uncorrected radiance shows a large negative bias of surface pressure for all cameras, as compared to the terrain-corrected sea level pressure. The in-camera slopes of the bias are less pronounced, so are the discontinuities at the borders of the field-of-view of the cameras. The mean bias of the retrieved surface pressure is about -100 hPa. The retrieval based on stray light corrected radiances is very close to the terrain-corrected sea level pressure without any visible camera artefacts.

The correction factor f and the deviation from the spectral Fraunhofer calibration as found by the optimization approach are shown in figure 6.6. A relatively homogeneous amount of stray light was found in the oxygen A band, adding up to $4-7\,\%$ of the amount of radiance in band 10 L_{10}. Compared to the nominal band setting data, the in-camera slope of the stray light is negligible. The dependence of f on the across-track pixel index is not correlated to the spectral slope of the center wavelength. This supports the assumption, that the spectral Fraunhofer calibration is correct and a separation of the effects of spectral shifts and stray radiation is possible using the proposed empirical correction approach.

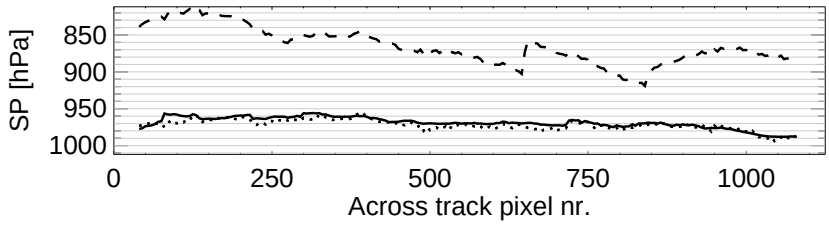

Figure 6.5: Along-track median values of surface pressure derived from DEM (solid lines) and MERIS spectral campaign measurements before (dashed) and after (dotted) optimization.

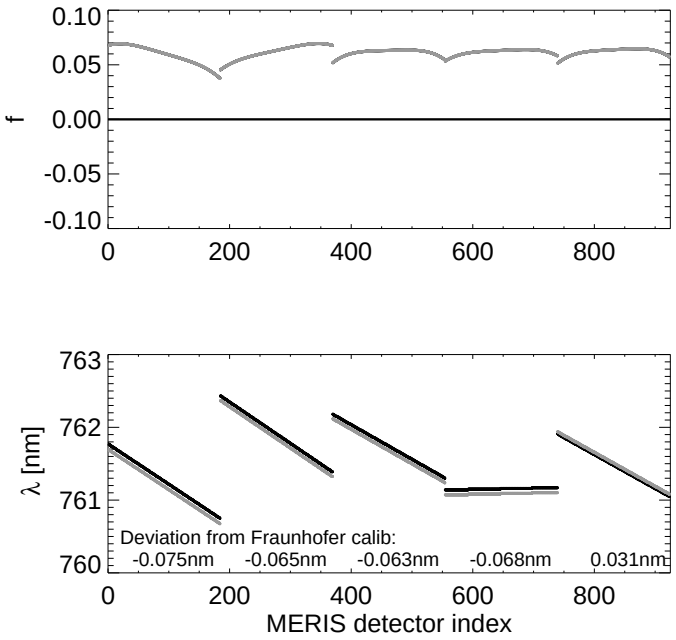

Figure 6.6: Same as for figure 6.4, but for spectral campaign band setting.

6.5 Application to independent MERIS data

The nominal band setting correction factors have been applied to MERIS scenes that were not part of the optimization scene composite, in order to demonstrate the global validity of the results. Two scenes are shown, a desert scene from October 15th, 2004 used for the retrieval of surface pressure and a stratocumulus cloud scene from May 16th, 2007.

6.5.1 Surface pressure

The selected clear sky scene is located above the Libyan desert. Figure 6.7 shows an RGB image of the scene, the surface pressure retrieval based on both uncorrected and corrected radiances and the terrain-corrected sea level pressure. In addition, scatter plots of the two retrievals and the terrain-corrected pressure and the along-track median of all three data sets are shown. Again, the retrieval based on unmodified radiances exhibits large camera effects with strong in-camera slopes and discontinuities at the borders of the field-of-view of the cameras of up to 120 hPa. The spatial structures of surface pressure are masked by the strong deviations caused by the insufficient correction for instrumental stray light. By applying the empirical correction factors, the camera effects completely disappear and the retrieved surface pressure is very close to the terrain-corrected sea level pressure. The root mean square error of the retrieval is reduced from 36 hPa to 5 hPa. Apparently, the correction factors found by optimizing selected surface and cloud-top pressure scenes are suitable for the correction of independent clear sky scenes.

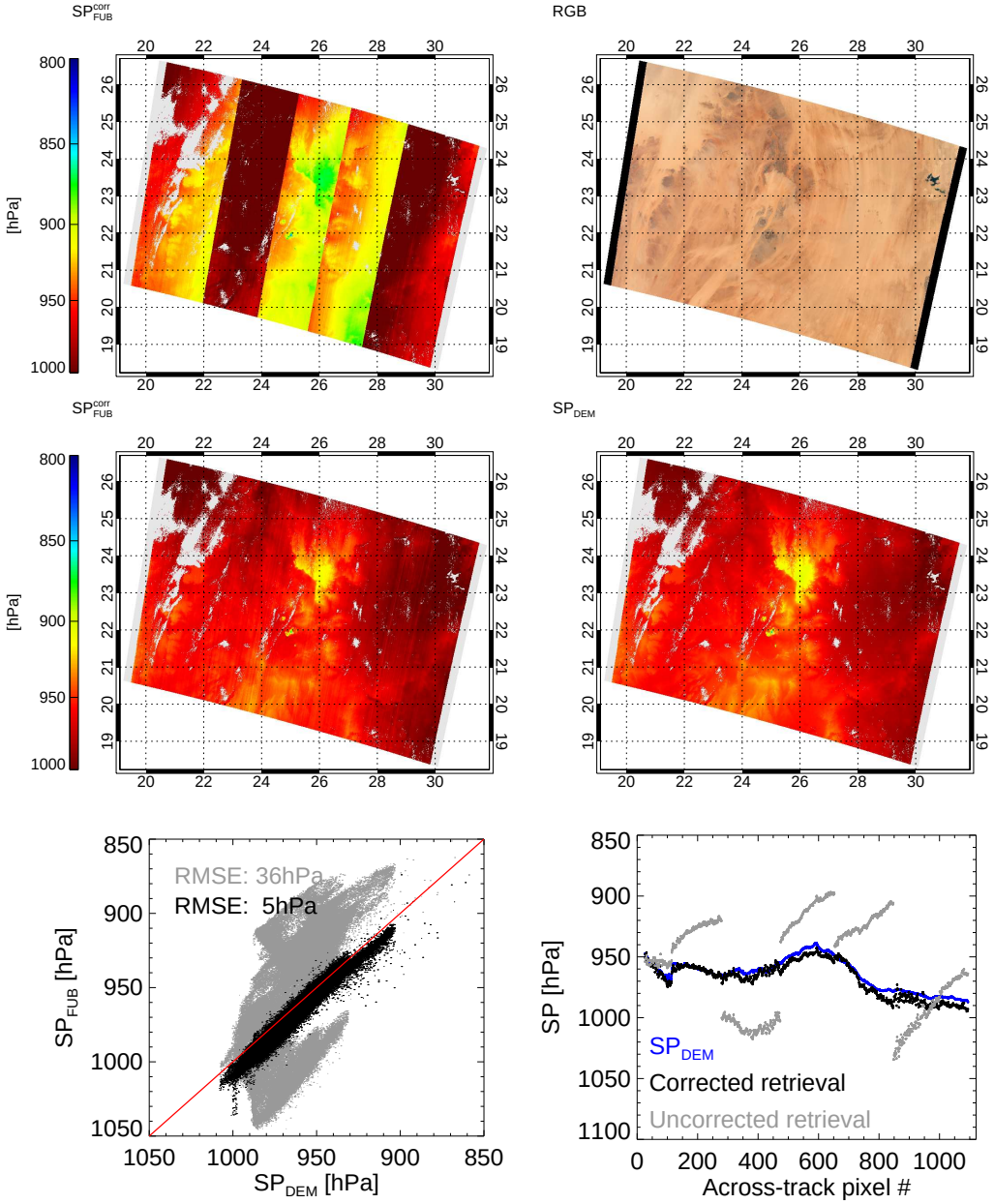

Figure 6.7: Effect of empirical stray light correction on retrieval of surface pressure: RGB image of Libyan desert on October 15th, 2004 (upper right panel), retrieved surface pressure (SP_{FUB}) from uncorrected (upper left panel) and corrected (middle left panel) radiances, terrain-corrected sea level pressure SP_{DEM} (middle right panel), scatter plot of corrected / uncorrected SP_{FUB} and SP_{DEM} (lower left panel), along-track median of SP_{FUB} and SP_{DEM} , depending on across-track pixel index (lower right panel).

6.5.2 Cloud-top pressure

The scene selected for the retrieval of cloud-top pressure is located above the Benguela current region and characterized by a homogeneous stratocumulus field. Figure 6.8 shows an RGB image, the CTP_{FUB}-retrieval based on both uncorrected and corrected radiances and the along-track median of both retrievals. Since the true cloud-top height is not known, the applied approach can only be evaluated with regard to what extent the artificial camera effects are reduced. Again, the uncorrected retrieval shows large camera artefacts caused by insufficient correction of stray light. The errors are strongly reduced in case stray light corrected radiances are used for the retrieval. However, residual camera effects are still visible.

6.6 Conclusion

A simple model of the instrumental stray light within the MERIS oxygen *A* band channel was optimized by fitting the retrieved pressure to accurate reference data. The main results of the stray light optimization are:

1. The simple stray light model, assuming a linear dependence on the brightness of the observed scene and a polynomial dependence on the spatial across-track pixel index of each camera, is suitable for a correction of the camera artefacts apparent in the derived pressure products.

2. A homogeneous amount of stray light was found in the spectral campaign orbits, that are not corrected for stray light in the operational processing chain. $4-7\,\%$ of the window radiance L_{10} have to be subtracted from the oxygen *A* band channels, in order to compensate the bias in derived surface pressure ($\sim -100\,\mathrm{hPa}$).

3. The correction factor found for the nominal band setting data shows strong in-camera slopes that follow the shape of the center wavelengths, indicating that the operational stray light correction scheme applied within the MERIS ground segment is not able to separate the effects of stray light and wavelength shifts.

4. The amount of stray light in the nominal channel 11 is overestimated for camera 4 and underestimated for all other cameras by the operational stray light correction

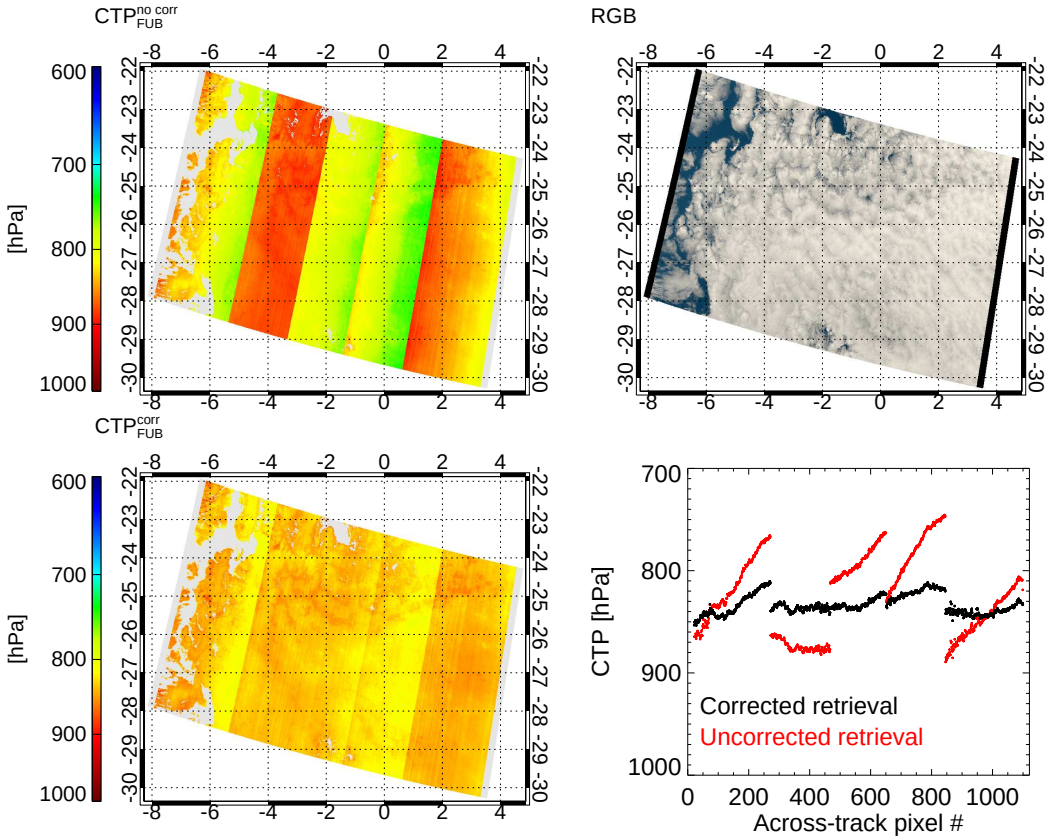

Figure 6.8: Effect of empirical stray light correction on retrieval of cloud-top pressure: RGB image of stratocumulus clouds above Benguela current on May 16th, 2007 (upper right panel), retrieved cloud-top pressure (CTP_{FUB}) from uncorrected (upper left panel) and corrected (lower left panel) radiances, along-track median of CTP_{FUB} for both retrievals depending on across-track pixel index (lower right panel).

scheme.

5. The center wavelength of MERIS band 11 is slightly adjusted by the optimization algorithm. The adjustment does not exceed ± 0.1 nm, which is the expected accuracy of the Fraunhofer calibration (Delwart et al. (2007)).

The current operational stray light correction scheme of the MERIS ground segment is not sufficient to correct the effects of stray radiation within the MERIS instrument. The proposed empirical correction factors are suitable for a significant reduction of the camera effects, as demonstrated by applying the correction to independent data (see section

6.5).
A further improvement of the correction accuracy will be obtained by extending the surface pressure retrieval. The current version is based on fixed temperature profiles, causing a bias in retrieved surface pressure in case the atmosphere is warmer or colder than assumed. The enhanced version will include the actual temperature profile, enabling a more accurate correction of stray light by a reduction of the surface pressure bias.

Acknowledgments

This work was carried out in the frame of the ESA-funded project "Exploitation of the MERIS oxygen *A* band" (contract nr. 20693 / 07 / I-OL). The authors would like to thank two anonymous reviewers for their comments and L. Bourg (ACRI-ST) for valuable information about the MERIS stray light characterization and nominal correction.

7 Conclusion

This work deals with the exploitation of satellite-borne measurements within the oxygen *A* absorption band around 0.76 µm for the retrieval of cloud height and the correction of instrumental stray light in the MERIS instrument onboard the ENVISAT satellite. It contains extensive studies regarding the sensitivity of single and multiple channels within the O_2 *A* band to cloud height and other influencing parameters like cloud optical and geometrical thickness, cloud microphysics, surface pressure and albedo, the temperature profile and instrumental calibration accuracy. The information content inherent to O_2 *A* measurements above clouds is analyzed and discussed with respect to the channel configuration. A maximum number of three independent pieces of information derivable from multispectral MERIS-like measurements in the oxygen *A* band is found, representing the cloud optical and geometrical thickness and the cloud height.

An algorithm for the retrieval of cloud-top pressure from MERIS measurements is presented and validated using airborne LIDAR measurements, revealing an accuracy of 25 hPa in case of low-level, single-layered clouds. However, large deviations are found for some cases, presumably situations with cirrus above the observed low-level clouds. Since MERIS provides only a single channel inside the oxygen absorption band, additional information is necessary to account for the effect of cirrus. Based on synergistic measurements of MERIS and AATSR, both mounted on ENVISAT, a new technique for the retrieval of multilayer cloud height in case of cirrus above low-level clouds is developed and presented. It is based on the fact that the cloud height derived from measurements in the thermal infrared spectral region, as provided by e.g. the 11 µm channel of AATSR, in the vast majority of cases corresponds to the uppermost cloud layer, even if it is optically thin. In contrast, the transmission within the O_2 *A* band, as measured by MERIS, is predominantely influenced by the optical center of the cloud system, which is close to the lower cloud layer in cases of cirrus above low-level clouds. By exploiting the split window brightness temperature difference of the 12 µm and the 11 µm channel of AATSR, cases with optically thin cirrus above optically thick low clouds are identified. The measurements of AATSR and MERIS are used for the retrieval of multilayer cloud height for these cases. The novel and unique methodolgy is demonstrated using the example of two multilayered cloud systems above the Northern Atlantic.

A second focus of this thesis is on the correction of instrumental stray light within MERIS, caused by multiple scattering and reflection at optical elements like lenses or gratings. Since stray light represents one of the main sources of errors of MERIS mea-

surements within the oxygen *A* band, empirical correction factors are determined and applied to MERIS data. Therefore, an algorithm for the retrieval of land surface pressure is developed and used for the optimization of derived pressure by adjusting the coefficients of a simple brightness-dependent stray light model. The operational stray light correction applied within the MERIS ground segment is found to work improperly in general, causing a pixel-dependent over- or underestimation of stray light. In case of previously uncorrected data an amount of $4-7$ % of stray light is found in the oxygen *A* band channel. The errors of derived surface and cloud-top pressure are greatly reduced by the empirical stray light correction, as demonstrated by applying the correction factors to independent cloudy and clear sky scenes.

The measurements of MERIS and AATSR will be continued and extended by OLCI (**O**cean and **L**and **C**olour **I**nstrument) and SLSTR (**S**ea and **L**and **S**urface **T**emperature **R**adiometer) onboard the GMES Sentinel-3 satellite, to be launched in 2012. Prospectively, OLCI will provide measurements in three spectral channels inside the oxygen *A* band, involving a gain of information about the height and vertical extent of clouds, as compared to the measurements of MERIS. A main focus of OLCI and SLSTR will be on the enhancement of the synergistic usage of both instruments. Thus, the results found in the frame of this thesis will help to develop adequate algorithms for the retrieval of cloud height of single- and dual-layered cloud systems and successfully exploit the synergy of both instruments.

Zusammenfassung

Die vorliegende Arbeit befasst sich mit der Auswertung von satellitengestützten Messungen innerhalb der Sauerstoff *A* Absorptionsbande bei 0.76 µm für die Bestimmung der Wolkenhöhe und die Korrektur von Streulicht im MERIS Instrument an Bord des ENVISAT-Satelliten. Sie enthält ausführliche Studien zur Sensitivität von sowohl einzelnen als auch mehreren Kanälen innerhalb der O_2 *A* Bande zur Wolkenhöhe sowie weiteren Einflussgrößen wie der optischen und geometrischen Wolkendicke, der Wolkenmikrophysik, dem Luftdruck am Boden, der Oberflächenhelligkeit, dem Temperaturprofil und der Genauigkeit der Instrumentenkalibration. Der Informationsgehalt von Messungen innerhalb der Sauerstoffbande über Wolken wird in Abhängigkeit der Kanalkonfiguration analysiert und diskutiert. Bei einer MERIS-ähnlichen spektralen Auflösungen sind maximal drei unabhängige Größen aus multispektralen Messungen innerhalb der O_2 *A* Bande ableitbar: die optische und geometrische Wolkendicke sowie die Wolkenhöhe.

Ein Algorithmus für der Bestimmung der Wolkenhöhe aus MERIS-Messungen wird vorgestellt und mit flugzeuggestützten LIDAR-Messungen validiert. Für tiefe Einschichtbewölkung ergibt sich für das MERIS-Verfahren eine Genauigkeit von 25 hPa, wohingegen sich der Fehler für Fälle mit Cirrus-Bewölkung oberhalb tiefer Wolken deutlich erhöht. Da MERIS innerhalb der O_2 *A* Bande lediglich Messungen in einem einzelnen Kanal liefert, müssen für die Berücksichtigung des Effektes von Cirrusbewölkung zusätzliche Informationen hinzugezogen werden. Basierend auf synergetischen Messungen der Instrumente MERIS und AATSR, jeweils an Bord von ENVISAT, wird eine neuartige Methode zur Bestimmung der Höhe zweier übereinander liegender Wolkenschichten vorgestellt. Sie basiert auf der Tatsache, dass die aus Messungen im thermisch-infraroten Spektralbereich, wie beispielsweise dem 11 µm-Kanal von AATSR, abgeleitete Wolkenhöhe in der Regel der Höhe der obersten Wolkenschicht entspricht. Im Gegensatz dazu wird die von MERIS gemessene Transmission in der

O_2 *A* Bande hauptsächlich vom optischen Zentrum des Wolkensystems bestimmt, das im Fall von optisch dünnem Cirrus über tiefen Wolken nahe der unteren Wolkenschicht liegt. Die Auswertung der Helligkeitstemperaturdifferenz zwischen dem 11 µm- und dem 12 µm-Kanal von AATSR erlaubt die Identifizierung geeigneter Fälle von optisch dünnem Cirrus über optisch dicken tiefen Wolken. Die Messungen von MERIS und AATSR werden genutzt um die Höhe beider Wolkenschichten in diesen Fällen zu bestimmen. Das einzigartige Verfahren wird anhand zweier Fallstudien von Mehrschichtbewölkung über dem Nordatlantik demonstriert.

Ein weiterer Fokus dieser Arbeit liegt auf der Korrektur von Streulicht innerhalb des MERIS-Instruments, das durch mehrfache Reflektion und Streuung an optischen Elementen wie Linsen oder Beugungsgittern entsteht. Da Streulicht eine der Hauptfehlerquellen für MERIS-Messungen innerhalb der O_2 *A* Bande darstellt, werden empirische Streulicht-Korrekturkoeffizienten ermittelt. Dies erfordert die Entwicklung eines Verfahrens zur Bestimmung des Luftdrucks am Boden aus MERIS-Messungen das im Folgenden für die Angleichung des abgeleiteten Luftdrucks in ausgewählten MERIS-Szenen durch Optimierung der Koeffizienten eines einfachen Streulicht-Modells genutzt wird. Das operationelle Verfahren zur Streulichtkorrektur, das innerhalb des MERIS ground segment zum Einsatz kommt, stellt sich als unzureichend heraus und führt je nach Blickwinkel zu Über- bzw. Unterschätzung des Streulichts. In zuvor unkorrigierten Daten wird ein Streulichtanteil von 4 - 7 % im MERIS O_2 *A* Kanal gefunden. Anhand von bewölkten und unbewölkten MERIS-Szenen wird gezeigt, dass die Fehler der abgeleiteten Wolkenhöhe und des Bodendrucks durch die empirische Streulichtkorrektur deutlich reduziert werden.

Mit den Instrumenten OLCI (**O**cean and **L**and **C**olour **I**nstrument) and SLSTR (**S**ea and **L**and **S**urface **T**emperature **R**adiometer) an Bord des Sentinel-3 Satelliten werden die Messungen von MERIS und AATSR ab ca. 2012 fortgesetzt und erweitert. OLCI wird voraussichtlich die Strahldichte in drei Kanälen innerhalb der O_2 *A* Bande messen, was gegenüber MERIS einen Informationsgewinn über die Höhe und die vertikale Struktur von Wolken bedeutet. Ein Hauptaugenmerk der OLCI- und SLSTR-Missionen wird auf dem Ausbau der synergetischen Nutzung der beiden Instrumente liegen. Die Ergebnisse der vorliegenden Arbeit werden daher helfen, geeignete Algorithmen für die Ableitung der Wolkenhöhe von Einschicht- wie Mehrschichtbewölkung zu entwickeln und die Synergieeffekte der simultanen Messungen auszunutzen.

List of Tables

List of Figures

Bibliography

Aguirre, M., B. Berruti, J.-L. Bezy, M. Drinkwater, F. Heliere, U. Klein, C. Mavrocordatos, P. Silvestrin, B. Greco, and J. Benveniste, 2007: Sentinel-3, The Ocean and Medium-Resolution Land Mission for GMES Operational Services. *ESA Bulletin*, **131**, 24–29.

Aminou, D., 2002: MSG's SEVIRI Instrument. *ESA Bulletin*, **111**, 15–17.

Ardanuy, P. E., L. L. Stowe, A. Gruber, and M. Weiss, 1991: Shortwave, Longwave, and Net Cloud-Radiative Forcing as Determined From Nimbus 7 Observations. *J. Geophys. Res.*, **96**, 18537 – 18549.

Barton, I. J. and J. C. Scott, 1986: Remote measurement of surface pressure using absorption in the oxygen A-band. *Appl. Opt.*, **25**, 3502 – 3507.

Baum, B., R. Frey, G. Mace, M. Harkey, and P. Yang, 2003: Nighttime Multilayered Cloud Detection Using MODIS and ARM Data. *J. Appl. Meteor.*, **42**, 905–919.

Baum, B., A. Heymsfield, P. Yang, and S. Bedka, 2005a: Bulk Scattering Properties for the Remote Sensing of Ice Clouds. Part I: Microphysical Data and Models. *J. Appl. Meteor.*, **44**, 1885 – 1895, doi:doi:10.1175/JAM2308.1.

Baum, B., T. Uttal, M. Poellot, T. Ackerman, J. Alvarez, J. Intrieri, D. Starr, J. Titlow, V. Tovinkere, and E. Clothiaux, 1995: Satellite Remote Sensing of Multiple Cloud Layers. *J. Atmos. Sci.*, **52**, 4210–4230.

Baum, B. and B. Wielicki, 1994: Cirrus Cloud Retrieval Using Infrared Sounding Data: Multilevel Cloud Errors. *J. Appl. Meteor.*, **33**, 107–117.

Baum, B. A., R. F. Arduini, B. A. Wielicki, P. Minnis, and S.-C. Tsay, 1994: Multi-level cloud retrieval using multispectral HIRS and AVHRR data: Nighttime oceanic analysis. *J. Geophys. Res.*, **99**, 5499–5515.

Baum, B. A., P. Yang, A. J. Heymsfield, S. Platnick, M. D. King, Y.-X. Hu, and S. T. Bedka, 2005b: Bulk scattering models for the remote sensing of ice clouds. Part 2: Narrowband models. *J. Appl. Meteor.*, **44**, 1896–1911.

Bengtsson, L., 1979: Problems of using satellite information in numerical weather prediction. *Proc. of Technical Conference on 'Use of Data from Meteorological Satellites', Lannion, France*, ESA SP-143, 87–100.

Bennartz, R. and J. Fischer, 2000: A modified k-distribution approach applied to narrow band water vapour and oxygen absorption estimates in the near infrared. *J. Quant. Spectrosc. Radiat. Transfer*, **66**, 539–553.

Bennartz, R. and R. Preusker, 2006: Representation of the photon pathlength distribution in a cloudy atmosphere using finite elements. *J. Quant. Spectrosc. Radiat. Transfer*, **98**, 202 – 219, doi:10.1016/j.jqsrt.2005.05.085.

Breon, F. M. and S. Bouffies, 1996: Land surface pressure estimate from measurements in the oxygen A absorption band. *J. Appl. Meteor.*, **35**, 69 – 77.

Buriez, J., C. Vanbauce, F. Parol, P. Goloub, M. Herman, B. Bonnel, Y. Fouquart, P. Couvert, and G. Seze, 1997: Cloud detection and derivation of cloud properties from POLDER (Processing Algorithms). *Int. J. Rem. Sens.*, **18**, 2785–2813.

Burrows, J., M. Weber, M. Buchwitz, V. Rozanov, A. Ladstaetter-Weissenmayer, A. Richter, R. de Beek, R. Hoogen, K. Bramstedt, K. Eichmann, M. Eisinger, and D. Perner, 1999: The Global Ozone Monitoring Experiment (GOME): Mission concept and first scientific results. *J. Atmos. Sci.*, **56**, 151–175.

Chang, F.-L. and Z. Li, 2005a: A Near-Global Climatology of Single-Layer and Overlapped Clouds and Their Optical Properties Retrieved from Terra/MODIS Data Using a New Algorithm. *J. Climate*, **18**, 4752–4771.

— 2005b: A New Method for Detection of Cirrus Overlapping Water Clouds and Determination of Their Optical Properties. *J. Atmos. Sci.*, **62**, 3993–4009.

Crisp, D., R. Atlas, F.-M. Breon, L. Brown, J. Burrows, P. Ciais, B. Connor, S. Doney, I. Fung, D. Jacob, C. Miller, D. O'Brien, S. Pawson, J. Randerson, P. Rayner, R. Salawitch, S. Sander, B. Sen, G. Stephens, P. Tans, G. Toon, P. Wennberg, S. Wofsy, Y. Yung, Z. Kuang, B. Chudasama, G. Sprague, B. Weiss, R. Pollock, D. Kenyon, and S. Schroll, 2004: The Orbiting Carbon Observatory (OCO) Mission. *Advances in Space Research*, **34**, 700–709.

Delwart, S., R. Preusker, L. Bourg, R. Santer, D. Ramon, and J. Fischer, 2007: MERIS inflight spectral calibration. *Int. J. Rem. Sens.*, **28**, 479 – 496.

DiMarzio, J., A. Brenner, R. Schutz, C. Shuman, and H. J. Zwally, 2007: GLAS/ICESat 1 km laser altimetry digital elevation model of Greenland. *Digital media*.

Diner, D. J., J. C. Beckert, T. H. Reilly, C. J. Bruegge, J. E. Conel, R. A. Kahn, J. V. Martonchik, T. P. Ackerman, R. Davies, S. A. W. Gerstl, H. R. Gordon, J. P. Muller, R. B. Myneni, P. J. Sellers, B. Pinty, and M. M. Verstraete, 1998: Multi-angle Imaging SpectroRadiometer (MISR) - Instrument description and experiment overview . *IEEE Transactions on Geoscience and Remote Sensing*, **36**, 1072–1087.

Farr, T. G., E. Caro, R. Crippen, R. Duren, S. Hensley, M. Kobrick, M. Paller, E. Rodriguez, P. Rosen, L. Roth, D. Seal, S. Shaffer, J. Shimada, J. Umland, M. Werner, M. Oskin, D. Burbank, and D. Alsdorf, 2007: The Shuttle Radar Topography Mission. *Rev. Geophys.*, **45**, doi:10.1029/2005RG000183.

Fell, F. and J. Fischer, 2001: Numerical simulation of the light field in the atmosphere-ocean system using the matrix-operator method. *J. Quant. Spectrosc. Radiat. Transfer*, **3**, 351–388.

Fischer, J., W. Cordes, A. Schmitz-Pfeifer, W. Renger, and P. Mörl, 1991: Detection of Cloud-Top Height from Backscattered Radiances within the Oxygen A Band. Part 2: Measurements. *J. Appl. Meteor.*, **30**, 1260–1267.

Fischer, J. and H. Grassl, 1984: Radiative transfer in an atmosphere-ocean system: an azimuthally dependent matrix-operator approach. *Appl. Opt.*, **23**, 1035–1039.

— 1991: Detection of Cloud-Top Height from Backscattered Radiances within the Oxygen A Band. Part 1: Theoretical Study. *J. Appl. Meteor.*, **30**, 1245–1259.

Fischer, J., R. Preusker, and L. Schüller, 1997: ATBD 2.3 Cloud Top Pressure. Algorithm Theoretical Basis Document PO-TN-MEL-GS-0006, European Space Agency.

Frey, R. A., B. A. Baum, W. P. Menzel, S. A. Ackerman, C. C. Moeller, and J. D. Spinhirne, 1999: A comparison of cloud top heights computed from airborne LIDAR and MAS radiance data using CO2-slicing. *J. Geophys. Res.*, **104**, 24547–24555.

Fye, F. K., 1978: The AFGWC Automated Cloud Analysis Model. Tech. Memo. 78-002, Available from Air Force Global Weather Central, Offutt Air Force Base, NE, (ADA057176).

Gonzalez, A., P. Wendling, B. Mayer, J.-F. Gayet, and T. Rother, 2002: Remote sensing of cirrus cloud properties in the presence of lower clouds: An ATSR-2 case study during the Interhemispheric Differences in Cirrus Properties From Anthropogenic Emissions (INCA) experiment. *J. Geophys. Res.*, **107**, 15 pp., doi:10.1029/2002JD002535.

Goody, R. M. and Y. L. Young, 1989: *Atmospheric Radiation (Theoretical basis)*. Oxford Univ. Press, 2nd edition, 519 pp.

Gurney, C. M., 1982: The use of contextual information to detect cumulus clouds and cloud shadows in Landsat data. *Int. J. Rem. Sens.*, **3**, 51–62.

Hahn, C. J., S. G. Warren, J. London, R. Chervin, M., and R. Jenne, 1984: Atlas of simultaneous occurrence of different cloud types over land. Tech. Note TN-241+STR, NCAR, Available from National Center for Atmospheric Research, Boulder, CO 80307.

Hansen, J., 1971: Multiple scattering of polarized light in planetary atmospheres. Part II: Sunlight reflected by terrestrial water clouds. *J. Atmos. Sci.*, **28**, 1400 – 1426.

Hasler, A. F., 1981: Stereographic observations from geosynchronous satellites: An important new tool for the atmospheric sciences. *Bull. Amer. Meteor. Soc.*, **62**, 194–211.

Heese, B., V. Freudenthaler, M. Seefeldner, and M. Wiegner, 2002: POLIS - A new POrtable LIdar System for ground-based and airborne measurements of aerosols and clouds. *Proceedings of the 21st ILRC, Quebec, Canada*, ICLAS, 71–74.

Heidinger, A. K. and M. J. Pavolonis, 2005: Global daytime distribution of overlapping cirrus cloud from NOAA's Advanced Very High Resolution Radiometer. *J. Climate*, **18**, 4772–4784.

Heymsfield, A. J., S. Matrosov, and B. Baum, 2003: Ice Water Path-Optical Depth Relationships for Cirrus and Deep Stratiform Ice Cloud Layers. *J. Appl. Meteor.*, **42**, 1369 – 1390.

Holz, R. E., T. Maestri, S. A. Ackerman, and L. E. Gumley, 2007: Comparing Actively Remote Sensed Lidar Cloud Properties with Passive AIRS and MODIS Retrievals. *Fourier Transform Spectroscopy/ Hyperspectral Imaging and Sounding of the Environment, OSA Technical Digest Series (CD)*, Optical Society of America, number HTuD2 in OSA Technical Digest Series.

Houghton, J. T., Y. Ding, D. Griggs, M. Noguer, P. J. van der Linden, and D. Xiaosu, 2001: *Climate Change 2001: The Scientific Basis* . Cambridge University Press.

Huot, J.-P., M. Rast, S. Delwart, J.-L. Bezy, G. Levrini, and H. Tait, 2001: The optical imaging instruments and their applications - AATSR and MERIS. *ESA Bulletin*, **106**, 56–66.

Inoue, T., 1987: A Cloud Type Classification With NOAA 7 Split-Window Measurements. *J. Geophys. Res.*, **92**, 3991 – 4000.

Kondo, K., R. Imasu, T. Kimura, M. Suzuki, A. Kuze, T. Ogawa, and T. Nakajima, 2003: Mission objectives and instrument design concept of EarthCARE FTS. *Multispectral and Hyperspectral Remote Sensing Instruments and Applications, Proceedings of the SPIE*, volume 4897, 91–98.

Krasnopolsky, V. M., 2007: Neural network emulations for complex multidimensional geophysical mappings: Applications of neural network techniques to atmospheric and oceanic satellite retrievals and numerical modeling. *Rev. Geophys.*, **45**, 34 pp., doi:10.1029/2006RG000200.

Kuze, A. and K. V. Chance, 1994: Analysis of cloud top height and coverage from satellites using the O_2A and B band. *J. Geophys. Res.*, **99**, 14481–14491.

Kyle, H., J. Hickey, P. Ardanuy, H. Jacobowitz, A. Arking, G. Campbell, F. House, R. Maschhoff, G. Smith, L. Stowe, and T. V. Haar, 1993: The Nimbus Earth Radiation Budget (ERB) Experiment: 1975 to 1992. *Bull. Amer. Meteor. Soc.*, **74**, 815–830.

Le Treut, H., R. Somerville, U. Cubasch, Y. Ding, C. Mauritzen, A. Mokssit, T. Peterson, and M. Prather, 2007: *Historical Overview of Climate Change In: Climate Change 2007: The Physical Science Basis. Contribution of Working Group I to the Fourth Assessment Report of the Intergovernmental Panel on Climate Change*. Cambridge University Press, Cambridge, United Kingdom and New York, NY, USA.

Lindstrot, R., R. Preusker, and J. Fischer, 2009: The retrieval of land surface pressure from MERIS measurements in the oxygen A band. *J. Atmos. Oceanic Technol.*, **26**, 1367 – 1377.

Lindstrot, R., R. Preusker, T. Ruhtz, B. Heese, M. Wiegner, C. Lindemann, and J. Fischer, 2006: Validation of MERIS cloud top pressure using airborne lidar measurements. *J. Appl. Meteor. Climat.*, **45**, 1612 – 1621.

Mace, G. G., T. P. Ackerman, and E. E. Clothiaux, 1997: A study of composite cirrus morphology using data from a 94-GHz radar and correlation with temperature and large-scale vertical motion. *J. Geophys. Res.*, **102**, 13581–13593.

Mace, G. G., S. Benson, and S. Kato, 2006: Cloud radiative forcing at the Atmospheric Radiation Measurement Program Climate Research Facility: 2. Vertical redistribution of radiant energy by clouds. *J. Geophys. Res.*, **111**, doi:doi:10.1029/2005JD005922.

Mace, G. G., Q. Zhang, M. Vaughan, R. Marchand, G. Stephens, C. Trepte, and D. Winker, 2009: A description of hydrometeor layer occurrence statistics derived from the first year of merged Cloudsat and CALIPSO data. *J. Geophys. Res.*, **114**, 17 pp., doi:doi:10.1029/2007JD009755.

Macke, A., J. Mueller, and E. Raschke, 1996: Single scattering properties of atmospheric ice crystals. *J. Atmos. Sci.*, **53**, 2813 – 2825.

McClatchey, R., R. Fenn, J. Selby, F. Volz, and J. Garing, 1972: *Optical Properties of the Atmosphere*. Air Force Cambridge Research Laboratories, 3rd edition.

Meehl, G. A., W. M. Washington, J. M. Arblaster, and A. Hu, 2004: Factors Affecting Climate Sensitivity in Global Coupled Models. *J. Climate*, **17**, 1584–1596.

Menzel, W. P., R. A. Frey, B. A. Baum, and Z. H., 2006: Cloud top properties and cloud phase algorithm theoretical basis document. Algorithm Theoretical Basis Document MOD04, Cooperative Institute for Meteorological Satellite Studies, University of Wisconsin.

Menzel, W. P., W. L. Smith, and T. R. Stewart, 1982: Improved cloud motion wind vector and altitude assignment using VAS. *J. Appl. Meteor.*, **22**, 377 – 384.

Merheim-Kealy, P., J. P. Huot, and S. Delwart, 1999: The MERIS ground segment. *Int. J. Rem. Sens.*, **20**, 1703–1712.

Mitchell, R. M. and D. M. O'Brien, 1987: Error Estimates for Passive Satellite Measurement of Surface Pressure Using Absorption in the A Band of Oxygen. *J. Atmos. Sci.*, **44**, 1981–1990.

Morel, M., J. Bezy, F. Montagner, A. Morel, and J. Fischer, 1993: Envisat's Medium Resolution Imaging Spectrometer: MERIS. *ESA Bulletin*, 40 – 44.

Muller, J.-P., M.-A. Denis, R. D. Dundas, K. L. Mitchell, C. Naud, and H. Mannstein, 2007a: Stereo cloud-top heights and cloud fraction retrieval from ATSR-2. *Int. J. Rem. Sens.*, **28**, 1921 – 1938.

Muller, J.-P., R. Preusker, J. Fischer, M. Zuhlke, C. Brockmann, and P. Regner, 2007b: ALBEDOMAP: MERIS land surface albedo retrieval using data fusion with MODIS BRDF and its validation using contemporaneous EO and in situ data products. *IGARSS International Geoscience and Remote Sensing Symposium, 2007*, 2404–2407.

Nasiri, S. L. and B. A. Baum, 2004: Daytime Multilayered Cloud Detection Using Multispectral Imager Data. *J. Atmos. Oceanic Technol.*, **21**, 1145 – 1155.

O'Brien, D. and R. Mitchell, 1989: Zones of feasibility for retrieval of surface pressure from observations of absorption in the A band of oxygen. *Division of Atmospheric Research Technical Papers*, **19**, 12.

— 1992: Error Estimates for Retrieval of Cloud-Top Pressure Using Absorption in the A Band of Oxygen. *J. Appl. Meteor.*, **31**, 1179–1192.

O'Brien, D., R. Mitchell, S. English, and G. Da Costa, 1998: Airborne Measurements of Air Mass from O2 A-Band Absorption Spectra. *J. Atmos. Oceanic Technol.*, **15**, 1272 – 1286.

Ou, S., K. Liou, and B. Baum, 1996: Detection of Multilayer Cirrus Cloud Systems Using AVHRR Data: Verification Based on FIRE II IFO Composite Measurements. *J. Appl. Meteor.*, **35**, 178 – 191.

Pavolonis, M. J. and A. K. Heidinger, 2004: Daytime cloud overlap detection from AVHRR and VIIRS. *J. Appl. Meteor.*, **43**, 762–778.

Petty, G. W., 2006: *A First Course in Atmospheric Radiation*. Sundog Publishing, 460 pp.

Preusker, R. and R. Lindstrot, 2009: Remote sensing of cloud-top pressure using moderately resolved measurements within the oxygen A band - a sensitivity study. *J. Appl. Meteor. Climat.*, **48**, 1562 – 1574.

Ramanathan, V., B. R. Barkstrom, and E. F. Harrison, 1989: Climate and the Earth's Radiation Budget. *Physics Today*, **22**, 22–32.

Randall, D., R. Wood, S. Bony, R. Colman, T. Fichefet, J. Fyfe, V. Kattsov, A. Pitman, J. Shukla, J. Srinivasan, R. Stouffer, A. Sumi, and K. Taylor, 2007: *Climate Models and Their Evaluation. In: Climate Change 2007: The Physical Science Basis. Contribution of Working Group I to the Fourth Assessment Report of the Intergovernmental Panel on Climate Change* . Cambridge University Press, Cambridge, United Kingdom and New York, NY, USA.

Rast, M., J. L. Bezy, and S. Bruzzi, 1999: The ESA Medium Resolution Imaging Spectrometer MERIS - A review of the instrument and its mission. *Int. J. Rem. Sens.*, **20**, 1681–1702.

Rodgers, C., 2000: *Inverse Methods for Atmospheric Sounding: Theory and Practice*. World Scientific, London.

Rossow, W. B. and Y. C. Zhang, 1995: Calculation of surface and top-of-atmosphere radiative fluxes from physical quantities based on ISCCP datasets: 2. validation and first results. *J. Geophys. Res.*, **100**, 1167–1197.

Rothman, L. S., D. Jacquemart, A. Barbe, D. Chris Benner, M. Birk, L. R. Brown, M. R. Carleer, C. Chackerian, K. Chance, L. H. Coudert, V. Dana, V. M. Devi, J. M. Flaud, R. R. Gamache, A. Goldman, J.-M. Hartmann, K. W. Jucks, A. G. Maki, J.-Y. Mandin, S. T. Massie, J. Orphal, A. Perrin, C. P. Rinsland, M. A. H. Smith, J. Tennyson, R. N. Tolchenov, R. A. Toth, J. Vander Auwera, P. Varanasi, and G. Wagner, 2005: The HITRAN 2004 molecular spectroscopic database. *J. Quant. Spectrosc. Radiat. Transfer*, **96**, 139–204.

Saunders, R., M. Matricardi, and A. Geer, 2008: RTTOV9.1 users guide. NWP SAF report, Met. Office.

Seiz, G., R. Davies, and A. Gruen, 2006: Stereo cloud-top height retrieval with ASTER and MISR. *Int. J. Rem. Sens.*, **27**, 1839–1853.

Shenk, W. E. and R. J. Curan, 1973: A multi-spectral method for estimating cirrus cloud top heights. *J. Appl. Meteor.*, **12**, 1213–1216.

Smith, W. L. and C. M. R. Platt, 1978: Intercomparison of radiosonde, ground based laser, and satellite deduced cloud heights. *J. Appl. Meteor.*, **17**, 1796–1802.

Stephens, G. L. and A. K. Heidinger, 2000: Molecular line absorption in a scattering atmosphere: I. Theory. *J. Atmos. Sci.*, **57**, 1599–1614.

Stephens, G. L., D. G. Vane, R. Boain, G. Mace, K. Sassen, Z. Wang, A. Illingworth, E. O'Connor, W. Rossow, S. L. Durden, S. Miller, R. Austin, A. Benedetti, and C. Mitrescu, 2002: The CloudSat Mission and the A-Train: A new dimension of space-based observations of clouds and precipitation. *Bull. Amer. Meteor. Soc.*, **83**, 1771–1790.

Stuffler, T., H. Kaufmann, S. Hofer, K.-P. Foerster, G. Schreier, A. Mueller, A. Eckardt, H. Bach, B. Penne, U. Benz, and R. Haydn, 2007: The EnMAP hyperspectral imager- An advanced optical payload for future applications in Earth observation programmes. *Acta Astronautica*, **61**, 115–120.

Tsushima, Y., S. Emori, T. Ogura, M. Kimoto, M. J. Webb, K. D. Williams, M. A. Ringer, B. J. Soden, B. Li, and N. Andronova, 2006: Importance of the mixed-phase cloud distribution in the control climate for assessing the response of clouds to carbon dioxide increase: a multi-model study. *Climate Dynamics*, **27**, 113 – 126, doi:10.1007/s00382-006-0127-7.

U.S.GeologicalSurvey, 1996: Global 30 Arc-Second Elevation Data Set . *http://edc.usgs.gov/products/elevation/gtopo30/README.html*.

Vanbauce, C., J. Buriez, F. Parol, B. Bonnel, G. Seze, and P. Couvert, 1998: Apparent Pressure Derived from ADEOS-POLDER Observations in the Oxygen A-Band Over Ocean. *Geophys. Res. Lett.*, **25**, 3159–3162.

Wang, P., P. Stammes, R. van der A, G. Pinardi, and M. van Roozendael, 2008: FRESCO+: an improved O2 A-band cloud retrieval algorithm for tropospheric trace gas retrievals. *Atmospheric Chemistry and Physics*, **8**, 6565–6576.

Wielicki, B. A. and J. A. Coakley, 1981: Cloud retrieval using infrared sounder data: Error analysis. *J. Appl. Meteor.*, **20**, 157–169.

Winker, D., C. Hostetler, and W. Hunt, 2004: CALIOP: The CALIPSO Lidar. *22nd International Laser Radar Conference, Matera, Italy*.

Winker, D. M., M. A. Vaughan, A. H. Omar, Y. Hu, K. A. Powell, Z. Liu, W. H. Hunt, and S. A. Young, 2009: Overview of the CALIPSO Mission and CALIOP Data Processing Algorithms. *J. Atmos. Oceanic Technol.*, **26**, 2310–2323.

Wiscombe, W. J., 1980: Improved Mie scattering algorithms. *Appl. Opt.*, **19**, 1505 – 1509.

Wu, M.-L. C., 1985: Remote sensing of cloud-top pressure using reflected solar radiation in the oxygen A-band. *J. Appl. Meteor.*, **24**, 539–546.

Yamamoto, G. and D. Wark, 1961: Discussion of the Letter by R. A. Hanel: Determination of Cloud Altitude from a Satellite. *J. Geophys. Res.*, **66**, 3569.

Zwally, H. J., B. Schutz, W. Abdalati, J. Abshire, C. Bentleyand, A. Brenner, J. Bufton, J. Dezio, D. Hancock, D. Hardingand, T. Herring, B. Minster, K. Quinn, S. Palm,

J. Spinhirne, and R. Thomas, 2002: ICESat's laser measurements of polar ice, atmosphere, ocean and land. *Journal of Geodynamics*, **34**, 405 – 445.

Acknowledgments

First of all, I would like to thank Prof. Jürgen Fischer for continued support and encouragement and the opportunity to work on this interesting topic. At the Institut für Weltraumwissenschaften he has created a relaxed but focused and goal-oriented working atmosphere. I am much obliged to Prof. Ralf Bennartz for agreeing to be second supervisor and the invitation to work at his group for one year. Both scientifically and personally, I have made invaluable experiences during my stay at the Department of Atmospheric and Oceanic Sciences, UW Madison, WI, USA.
At both working groups I have met many inspiring, cooperative and tolerating colleagues, who enabled me to finish this work. Special thanks go to Dr. Rene Preusker, who has contributed in countless ways to the scientific success of this thesis.
Last but not least, I would like to thank my little family for everything else.